The copyright of this thesis vests in the author. No quotation from it or information derived from it is to be published without full acknowledgement of the source. The thesis is to be used for private study or non-commercial research purposes only.

Published by the University of Cape Town (UCT) in terms of the non-exclusive license granted to UCT by the author.

University of Cape Town

Physics of low and intermediate spin states of atomic nuclei in the mass $A \sim 160$ region

Maciej Andrzej Stankiewicz

University of Cape Town

Thesis Presented for the Degree of
DOCTOR OF PHILOSOPHY
in the Department of Physics
University of Cape Town

May 2013

Abstract

The nuclear landscape provides possibly the richest set of data that can be collected for quantum systems, displaying many varying features. The lack of a complete nuclear theory has resulted in a fragmentation of the theories used to describe isolated sections of observables in the landscape of nuclear excitations. A recent model proposed that a tetrahedral deformation could explain observed low-lying, negative parity bands characterized by a lack of in-band electromagnetic transitions.

For this work, experimental data has been collected specifically to quantify the intensities of the "missing" in-band transitions for several nuclei in the mass 160 region ($^{156}_{68}$Er, $^{160}_{68}$Er and $^{158}_{66}$Dy). While these in-band transitions appear suppressed, it was possible to not only observe some of these transitions, but to quantify the suppression, which indicate a consistency within the band structure between low and medium spin states. An order of magnitude difference was observed in the $B(\mathrm{E2})/B(\mathrm{E1})$ branching ratios between the odd-spin and the even-spin octupole vibrational bands in ^{158}Dy and ^{160}Er. This difference is consistent with that reported in other nuclei in the region, which is indicative of some shared reason for this behaviour.

The theoretical aspect of this work tries to explain the observed anomalies in terms of the Random Phase Approximation model. Results of calculations suggest that in the intrinsic frame, the negative signature collective modes will have significantly stronger absolute $B(\mathrm{E1})$ rates than the positive signature band partners. By considering a quadrupole deformation of these vibrational states as consistent with the ground state band, the $B(\mathrm{E2})$ rates can be estimated, and the theoretical value for the $B(\mathrm{E2})/B(\mathrm{E1})$ branching ratio is shown to be qualitatively consistent with experimental observations. From this we conclude that the negative parity vibrational bands in the mass 160 region are likely low-K octupole bands, and not tetrahedrally deformed structures.

University of Cape Town

Contents

University of Cape Town

University of Cape Town

University of Cape Town

University of Cape Town

List of Figures

University of Cape Town

University of Cape Town

University of Cape Town

University of Cape Town

University of Cape Town

University of Cape Town

University of Cape Town

University of Cape Town

University of Cape Town

List of Tables

University of Cape Town

Chapter 1

Introduction

University of Cape Town

The field of nuclear physics has its roots at the beginning of the 20^{th} century. Rutherford discovered the existence of an atomic nucleus in 1911, but it was not until the discovery and identification of the neutron 20 years later that the study of the atomic nuclei truly began.

The atomic nucleus has been found to be a bound state of an integral number of protons and neutrons. These *nucleons* are individually well understood as spin $\frac{1}{2}$ fermions which obey the Pauli exclusion principle. The existence of bound states of charged protons, without the countering effect of any negative charges in the nucleus, implies the presence of another force, strong enough to overpower the electromagnetic repulsion between the protons. The *strong nuclear force* has been discovered, but has to this day not been completely understood.

1.1 Single particle models

The Yukawa potential was the first attempt at an explanation of the nuclear force, with a massive boson (π) mediating the interaction between nucleons. While the discovery of the pion in 1947 was a great success for the theory,

it has however been found that a nucleon-nucleon potential alone cannot account for the richness of nuclear physics.

Towards the end of the 1940s, significant progress was being made in the development of the nuclear shell model.[1] By modifying the spin-orbit coupling observed in atomic physics, the model had been able to explain the 'magic numbers' of nuclear physics, which result in nuclei with particular N or Z being particularly stable/abundant. By considering the protons and neutrons separately, and adding the nucleons in the lowest 'orbitals', consistent with the Pauli exclusion principle, the empirically observed magic numbers could be explained as shell gaps. While the model has been successful, the original iteration worked with a spherically symmetric potential, and it is therefore only accurate for nuclei with near-spherical shapes.

By observing excited states of nuclei, it has become apparent that most nuclei do not in fact conform to the spherical shape, but exhibit some form of deformation. The deformed shell model, developed by Nilsson [1], has proven to be a highly successful framework. In the Nilsson model the nucleus is assumed to have a quadrupole deformation, and the energies of the orbital levels depend on the orientation of the total angular momentum of the individual nucleons relative to the nuclear deformation.

University of Cape Town

1.2 Collective models

In a parallel development, rather than trying to derive the nuclear force from first principles, it was realized that collective descriptions of nuclear matter (particularly for high A) may provide a simpler understanding of the behaviour of nuclei. Developed by Weizsäcker in 1935, the semi-empirical mass formula (SEMF) presented an approximation for the nuclear binding energy in nuclear matter. It had been observed that the average binding energy per nucleon is approximately constant for most stable nuclei (usually

[1] Mainly by Wigner, Goeppert-Mayer and Jensen, who shared the Nobel Prize for the discovery.

in the 7-8 MeV range) [2, 3, 4, 5, 6, 7]. From this it was inferred that the nuclear force is short ranged (interactions are limited to nearest neighbours), and therefore the SEMF is a sum of a volume term (proportional to A), a surface term ($A^{2/3}$, for the nuclei not fully surrounded by others), and a Coulomb term for proton repulsion, with the weighting parameters fitted to reproduce the data. In addition, an asymmetry penalty term is included, as justified by the Pauli principle, as well as an empirical pairing term, which comes about from odd-even asymmetry.

The SEMF reproduces the general binding energies of nuclei near stability, but it does not provide any information about the particular configuration of the nucleons, or about the nuclear excitation modes available. Indeed, given that the coefficient of the surface term is a fitted constant, the SEMF implicitly approximates all nuclear shapes as constant (spherical). This approximation has to be abandoned for more accurate nuclear models.

University of Cape Town

1.3 Nuclear deformations

As mentioned in the previous section, the nuclear force appears to be short-ranged and individual nucleons behave as incompressible, hence the 'volume' of the nucleus is directly proportional to the number of nucleons (A) it contains. The nucleus is, of course, a quantum system, and it will not have a sharp spatial cut-off in the mass distribution, so a classical volume cannot be defined, but this is the natural first approximation to make. In addition one can assume the nuclear matter to form a compact set, and therefore that it can be described completely in terms of its surface only.

The most general surface expansion can be written as

$$R(\theta, \phi, t) = R_0\big[(1 + \Delta(\theta, \phi, t)\big], \tag{1.1}$$

where the R_0 represents the spherical approximation, and, for most deformations, $|\Delta| \ll 1$. The time and space dependence of the deformation func-

tion are usually taken to be separable, so that the rotations/vibrations of a deformed system can be created through a modulation of a single spatial deformation. At any given t, the surface can be expanded in terms of the orthogonal spherical harmonics

$$R(\theta,\phi)\Big|_t = R_0\left[1+\sum_{\lambda=0}^{\infty}\sum_{\mu=-\lambda}^{\lambda}\alpha_{\lambda\mu}Y_{\lambda\mu}(\theta,\phi)\right], \tag{1.2}$$

with constants $\alpha_{\lambda\mu}$. As the nuclear radius has to be real, by invoking symmetry under charge conjugation, as well as rotational invariance [3], the parameters $\alpha_{\lambda\mu}$ must transform like spherical tensors, and additionally $\alpha^*_{\lambda\mu} = (-1)^\mu \alpha_{\lambda\,-\mu}$. The implication is that in the set of $2\lambda+1$ parameters $\alpha_{\lambda\mu}$ there are $2\lambda+1$ independent degrees of freedom: $\alpha_{\lambda 0}$ has to be real, and every $\alpha_{\lambda\mu}$ can have real and imaginary parts for $\mu = 1\ldots\lambda$.

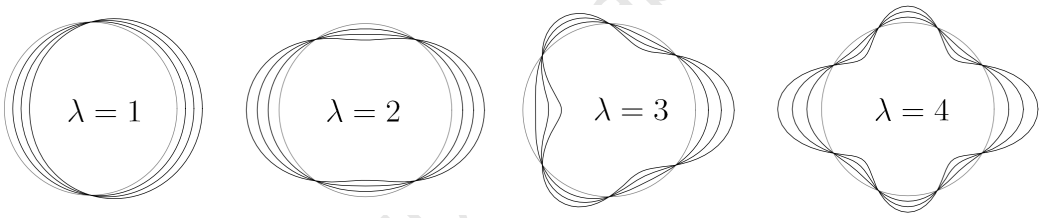

Figure 1.1: Schematic illustration of various multipole deformations. The deformations are done for pure $\alpha_{\lambda 0}$ states, with $\lambda = 1, ..., 4$. The various curves show the nuclear cross-section with $\alpha_{\lambda 0} = 0, 0.2, 0.4$ and 0.6.

The monopole deformation, ($\lambda = 0$), corresponds to a change in the radius of the nucleus, and therefore in the volume. A monopole vibration would correspond to a *breathing mode*, which, due to the high energies necessary for nuclear compression, need not be considered at normal energies. The dipole mode ($\lambda = 1$), at first order, corresponds to a translation of the nucleus, rather than actual deformation, and will generally be ignored when describing nuclear shapes.

The quadrupole ($\lambda = 2$) modes, being the lowest order non-trivial deformations (figure 1.1), turn out to be the most prevalent form of deformation observed in nuclear shapes, and will be discussed more in the following section.

University of Cape Town

Octupole ($\lambda = 3$) modes are also commonly observed in nuclear excitations, where the asymmetric shape manifests as negative parity bands.

The higher deformation modes have, so far, not been inferred to exist as pure states. For high values of λ the scale of surface deformations decreases, and stops being a plausible representation of the nucleus, whose surface is ultimately described in terms of its constituent nucleons. The $\lambda = 4$ modes are often included for mixing with quadrupole deformed nuclei, and the $\lambda = 6$ modes may also be included when describing octupole deformations.

1.3.1 Quadrupole deformations

It has been experimentally verified that the ground states of most even-even nuclei are deformed. The nuclei tend to exhibit a non-zero quadrupole moment, which is associated with a non-zero quadrupole deformation (possibly with other harmonics as well). A pure quadrupole deformation can be written as

$$R(\theta, \phi) = R_0 \left[1 + \sum_{\mu=-2}^{2} \alpha_{2\mu} Y_{2\mu}(\theta, \phi) \right], \tag{1.3}$$

where $\alpha_{2\,+2} = \alpha_{2\,-2}$ and $\alpha_{2\,+1} = \alpha_{2\,-1}$. By converting to Cartesian coordinates, and considering a rotation of the nucleus to its intrinsic frame [3], the 5 independent parameters can be understood in physical terms:

- $a_0 \equiv \alpha_{20}$, stretches the nuclear z axis with relation to the x and y axes,
- $a_2 \equiv \alpha_{2\pm2}$, stretches the nuclear x axis relative to the y axis,
- three Euler angles, defining the rotation of the nuclear intrinsic axes, in relation to the lab frame.

A different method of parameterization was introduced by A. Bohr [8] as:

$$a_0 = \beta \cos\gamma \qquad \text{and} \qquad a_2 = \frac{1}{\sqrt{2}} \beta \sin\gamma, \tag{1.4}$$

University of Cape Town

where the factor of $\frac{1}{\sqrt{2}}$ was chosen such that $\sum |\alpha_{\lambda\mu}|^2 = a_0^2 + 2a_2^2 = \beta^2$ is invariant. This polar analogue for quadrupole deformations has been accepted as the most convenient way of describing nuclear shapes.

The β-γ plot can be considered as an analog of the polar plot, although there is a complication in the non-uniqueness of individual points. A positive β with $\gamma = 0$ corresponds to an elongation of the z axis of a nucleus – termed a *prolate* shape. As γ is increased, the nucleus becomes tri-axial, as the x axis grows at the expense of the z, until (at $\gamma = 60°$) the two axes are equal, with the y axis shorter – this is termed an *oblate* shape. Increasing γ then continues to deform the nucleus, although it does not correspond to unique surface shapes, but rather cycles through the possible orientations in space. There are $3! = 6$ ways of setting up the axes, hence only the region $0 \leq \gamma \leq 60°$ need be considered.

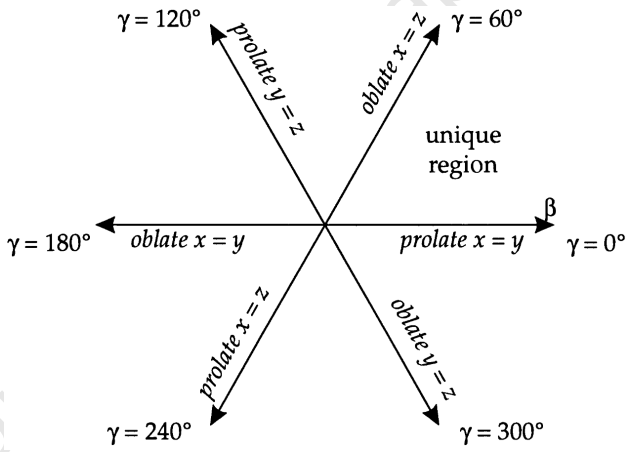

Figure 1.2: The β-γ plane, divided into the six equivalent regions [3]. Prolate nuclei have $\beta > 0$, $\gamma = 0°$, while oblate nuclei have $\beta < 0$ and $\gamma = 0°$.

For axially symmetric nuclei ($\gamma = 0°$) of mass AM and average radius R_0, the macroscopic quantities (moment of inertia and intrinsic quadrupole moment) of the nucleus can be integrated, and the next to leading order [2] values are:

$$I = \frac{2}{5} AMR_0^2(1 + 0.31\beta) \tag{1.5}$$

$$Q_0 = \frac{3}{\sqrt{5\pi}} ZR_0^2\beta(1 + 0.16\beta). \tag{1.6}$$

The values of I and Q_0 can be experimentally inferred through the structure of rotational bands and transition rates, which in turn allow one to infer the quadrupole deformation parameters of the nuclei.

1.3.2 Octupole deformations

Due to the pairing of nucleon spins, the ground state spin-parity of even-even nuclei is always found to be $J^\pi = 0^+$, and given that the parity of a Y_{lm} spherical harmonic is $(-1)^l$, this excludes the octupole shape from the ground state configurations. To create an octupole vibrational band, the configuration of the contained nucleonic matter needs to be rearranged, so octupole bands can only exist as nuclear excitations.

A rotational or vibrational structure can then be superimposed upon the octupole excited state. As local excitations of nuclear structures preserve the state's parity, and for electric transitions the photon that carries angular momentum l has parity $(-1)^l$, one can expect low lying octupole bands to have spin structures $1^-, 3^-, 5^-, \ldots$, or $2^-, 4^-, 6^-, \ldots$, and indeed this is often observed. These structures are generally assumed to be Y_{30} deformed.

However, upon close inspection it was found that while some nuclei display this aforementioned structure, they also exhibit a suppression of the in-band transitions. Based on theoretical calculations, Dudek [9, 10, 11] proposed that the negative parity bands might be representative of a Y_{32} deformation, rather than Y_{30}, which would result in the nucleus having a *tetrahedral* deformation.

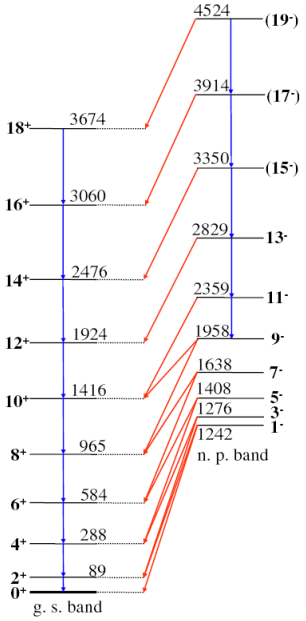

Figure 1.3: The spectrum of ^{156}Gd, showing lack of in-band transitions in the odd negative parity band [11].

University of Cape Town

Tetrahedral deformations

While the quadrupole deformations can be interpreted in direct, spatial terms, the same is not true for octupole deformations. Sufficient understanding can be derived from the shapes of the spherical harmonics themselves:

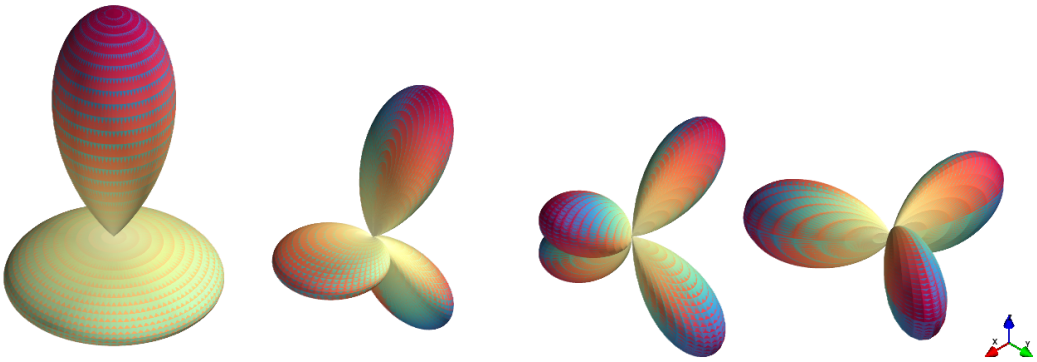

Figure 1.4: Parametric plots of the Y_{30}, Y_{31}, Y_{32} and Y_{33} spherical harmonics.

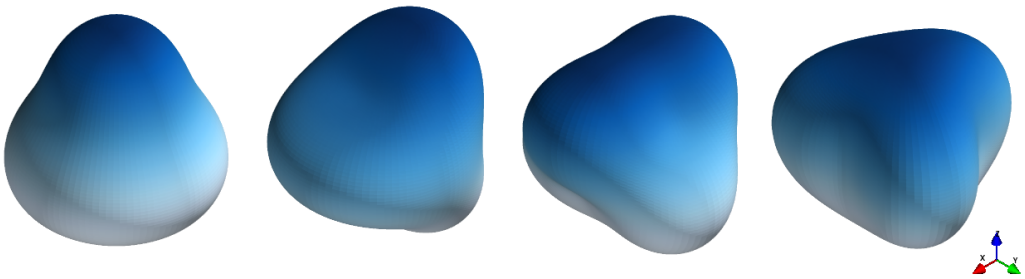

Figure 1.5: Shapes associated with pure octupole deformations, with $R(\theta, \phi) = 1 + 0.25 Y_{3i}(\theta, \phi)$, for $i = 0, 1, 2, 3$.

The Y_{30} associated deformation creates a *pear*-shape, while the Y_{31} and Y_{33} modes involve squashing the nucleus onto a plane and deforming it as in figure 1.1. The Y_{32} term involves a modulation with four preferred directions, as associated with the vertices of a tetrahedron. The predicted tetrahedral deformation [9, 11], is an appealing notion, as it is correlated with the T_d symmetry group. However, in order to realize a tetrahedral shape, the deformation will need to be a pure Y_{32} state, with no quadrupole deformations. This in turn would imply a suppression of E2 transitions, which had already been observed in ^{156}Gd.

Further calculations [9, 10] have suggested that, at certain tetrahedral deformations, the single particle energies exhibit 'shell gaps', much like the spherical shell model. The existence of these shell gaps suggests searching for tetrahedrally deformed nuclei with both Z and N near the 'magic numbers'. One such region is the rare-earths, with $(Z, N) \sim (70, 90)$.

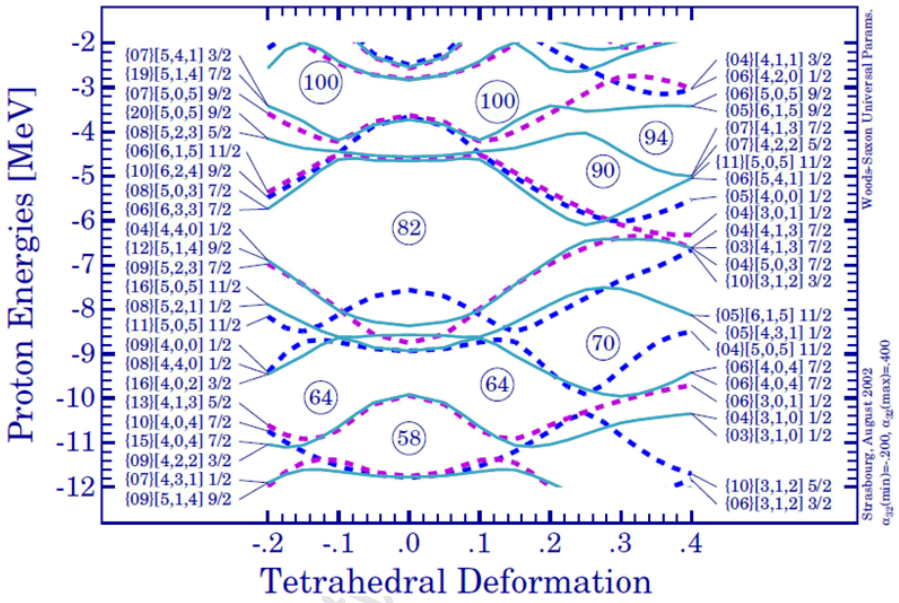

Figure 1.6: Single particle proton energies in a Woods-Saxon potential [12].

However, an experiment to study low-lying states in $^{160}_{70}\mathrm{Yb}_{90}$ was performed at iThemba LABS recently, and the inferred nuclear quadrupole moment (and deformation) was found to disagree with the tetrahedral prediction [13]. Furthermore, calculations of the branching ratios between the in-band and out-of-band transitions showed a distinct staggering between the odd and even spin octupole bands (figure 1.7). The staggering is consistent with that observed for several Gd isotopes.

1.4 Objectives and structure of thesis

The purpose of this study is to further explore the low-spin structure of nuclei in the rare-earth $(Z, N) \sim (70, 90)$ region, to determine the configuration and

University

all cases shows evi-
e: a subtle crossing
y arrows). In Fig. 3,
ther similarities. The
all typically less than
-spin states are up to a
is a difference in mo-
the Gd isotopes, we

bands are involved in the latter crossing, we adopt a multiple-band mixing model similar to that described in Ref. [25]. The energies of unperturbed bands, with wave functions $\phi_i(I)$, are parametrized using a variable moment of inertia (VMI) [26] expression given by

$$e(I) = e_0 + \tfrac{1}{2}C(\Im_I - \Im_0)^2 + (I - i_x)(I - i_x + 1)/2\Im_I,$$

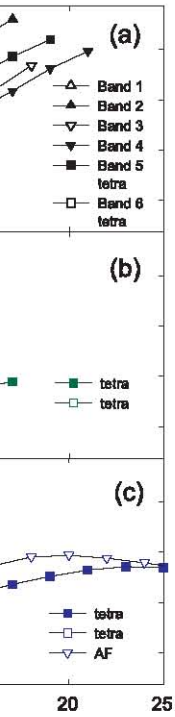

nd members in ^{154}Gd,
reference, vs spin.

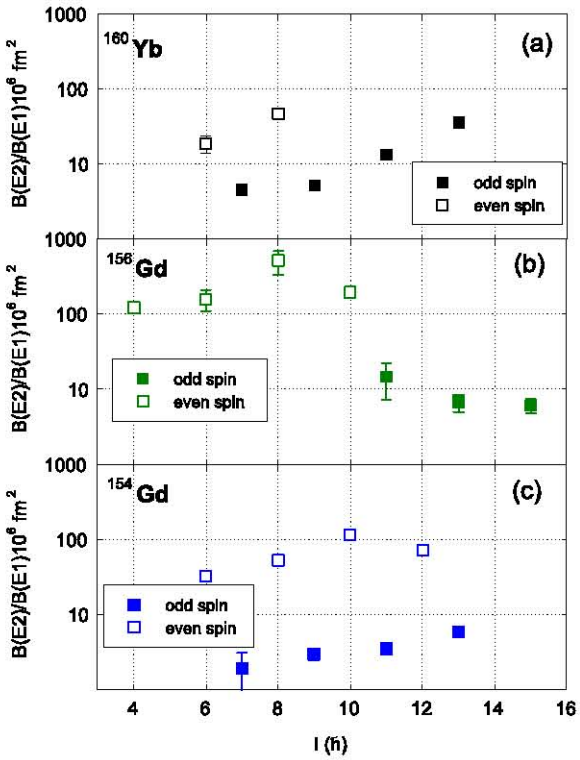

FIG. 3 (color online). $B(E2; I \rightarrow I-2)/B(E1; I \rightarrow I-1)$ (filled symbols) and $B(E2; I \rightarrow I-2)/B(E1; I \rightarrow I)$ (open symbols) values for proposed tetrahedral bands. Data for ^{156}Gd from Ref. [19].

Figure 1.7: $B(E2)/B(E1)$ ratios inferred for ^{160}Yb, ^{156}Gd and ^{154}Gd, showing anomalous behaviour between the odd and even spin octupole bands [13].

structure of the low-lying negative parity bands. Of particular interest is the apparent anomaly observed between the excitation strengths of the odd- and even-spin negative parity bands.

Chapter 2 will outline the relevant nuclear theoretical models which are successful in the description of phenomena observed at low and medium excitation energies. Chapter 3 describes the experimental setup, together with the tools used to collect and analyze the experimental data. The next chapter will contain results of the experiments, as well as a brief interpretation of the observed bands in terms of their underlying configurations. The structure of the negative-parity octupole bands will be discussed in detail in chapter 5, where the band energies and strengths will be compared to the results obtained from the calculations performed within the framework of the quasi-RPA model.

Chapter 2

Nuclear Models

University of Cape Town

The field of physics can be considered one of the purest forms of science, in that it attempts to explain the workings of the world around us. This inherently ambitious task is made even more daunting by the notion that any model of an aspect of the physical world cannot be *proved* to be correct. At best, a theoretical model can be used to make predictions, which may be verified experimentally. There is no guarantee that results of a future experiment will not deviate from the theory; a deviation which may either be explained through a refinement of the theory, or will necessitate the development of new models.

The current physics theories are considered correct for the electromagnetic and weak interactions, and general relativity is accepted, although it cannot be reconciled with quantum mechanics. The Lagrangian of the strong interaction is considered known, although the complexity of the theory does not allow the construction of solutions in nuclear physics. In order to explain the behaviour of strongly interacting matter, experiments are performed to probe nuclear matter across all energy scales (from thermal neutron induced reactions to 7 TeV collisions at the LHC), and many models have been developed to try and explain the observations.

In low-energy nuclear physics, dealing with bound systems of a fixed number of nucleons, a number of anomalous phenomena have been observed, and they

can be explained as an interplay between collective (rotations and vibrations) and single-particle interactions. The models relevant to this work, with some background will be discussed below.

2.1 Shell model

As the nuclear landscape was further explored, it was found that some atomic nuclei exhibited resistance to excitations at low energy. Already in 1934 the exceptional stability of ^{4}He, ^{16}O and ^{40}Ca was established. In 1948, with the development of accelerator systems, Mayer was able to deduce that nuclei with 50 and 82 protons, or 50, 82 and 126 neutrons also exhibited stability [14], which, combined with the naturally high abundance of tin and lead, implied a special property, which has been termed *magic*. The inertness of elements based on the number of electrons was well established from atomic theory, and it was conjectured that the inertness of the nuclei was from the closing of nuclear shells. The difficulty lay in the structure of the nuclear interaction – the electrons lay in a $-\frac{1}{r}$ potential which could be explicitly solved, but the nuclear potential was unknown.

By considering the motion of the nucleons inside the nucleus, Mayer and Jensen inferred that the potential must be flat near $r = 0$, and that the potential must go to zero rather abruptly near the surface [15]:

$$\left(\frac{dV}{dr}\right)_{r=0} = 0 \qquad \text{and} \qquad \left(\frac{dV}{dr}\right) > \left|\frac{V}{r}\right| \text{ for } r \to R. \tag{2.1}$$

This is naturally satisfied by the square well, but that model implies no force inside the nucleus, and infinitely strong forces at the surface. Another way to satisfy the conditions (2.1), is to let (dV/dr) increase linearly with r, or

$$V(r) = \begin{cases} -V_0[1-(r/R)^2] & \text{for } r < R, \\ 0 & \text{for } r > R. \end{cases} \tag{2.2}$$

In order to simplify the solving of the Schrödinger equation, they considered

University of Cape Town

an infinite square well, and an untruncated harmonic potential – for bound states these changes modify the attenuation of the tails of the wavefunctions, but should not overly affect the eigenvalues. The energy levels for the isotropic oscillation are then [15]:

$$E = \hbar\omega_0[2(n-1)+l] = N\hbar\omega_0, \tag{2.3}$$

where $\omega_0 = \sqrt{\frac{2V_0}{mR^2}}$, $N = 2(n-1)+l$, and the zero-point energy has been neglected. The evenly spaced states in a harmonic oscillator, combined with the state degeneracy, create a set of shells. The associated shell gaps occur at 2, 8, 20, which agree with the lower magic numbers, but continue to 40, 70, 112 and 168, which do not exhibit magic properties.

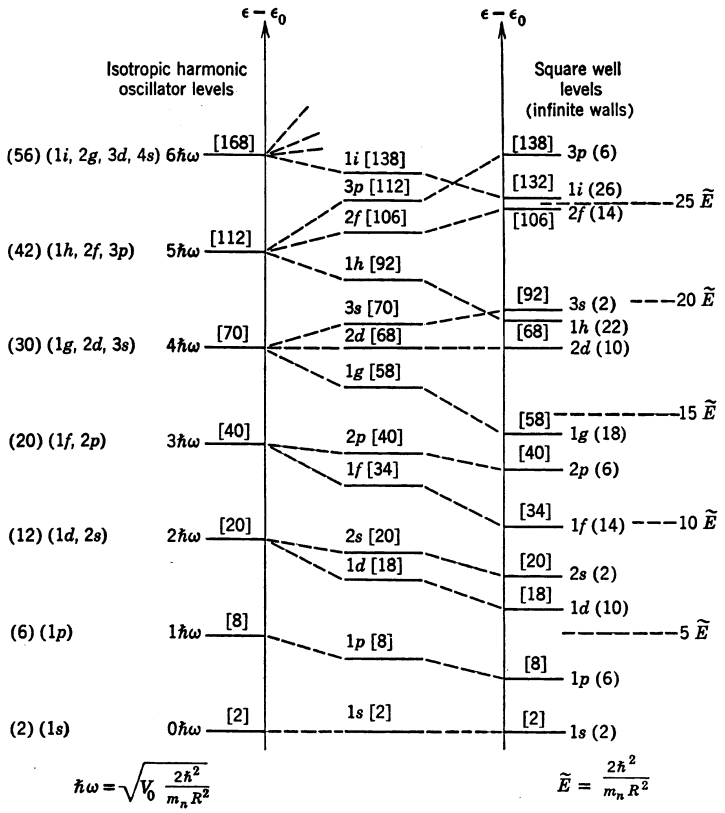

Figure 2.1: Mayer and Jensen's level system of the harmonic oscillator, infinite square well, and intermediate stage, indicating the expected shell gaps [15].

The next, inspired, step was the realization that the splitting in atomic levels depends not only on the quantum numbers n and l, but also on the spin-orbit coupling term $\vec{l} \cdot \vec{s}$, although the shifting of the orbital energies only reproduces the magic numbers if the spin-orbit coupling favours the orbitals with higher j, and the intermediate case behaviour can be reproduced by flattening the potential through the inclusion of a term proportional to l^2. The addition of an l^2 term would result in a narrowing of the shell-gaps, which can be offset through a $\langle l^2 \rangle_N = \frac{N(N+3)}{2}$ term [1]. The modified oscillator Hamiltonian can be written as

$$H = T + V = \frac{p^2}{2m} + \frac{1}{2} m\omega_0^2 r^2 + C\vec{l} \cdot \vec{s} + D\left(l^2 - \langle l^2 \rangle_N\right). \tag{2.4}$$

A more accurate representation can be established through the use of a Woods-Saxon potential $V(r) = -V_0 \left[1 + e^{\frac{r-R}{a}}\right]^{-1}$, although it has the disadvantage of not having closed analytic solutions, unlike the modified oscillator.

2.2 Nilsson model

The existence of rotational bands in nuclei implies non-spherical nuclear shapes. While it is possible to create deformed nuclei in a spherical potential, the deformed nature will affect the single-particle energies based on the quantum numbers of the orbitals, and this has to be incorporated into an effective model.

The modified oscillator model lends itself to generalization fairly naturally – if one was to allow the potential stiffness along the nuclear z-axis to be different to the stiffness along the x- and y-axes, the single-particle Hamiltonian will be

$$H = \frac{p^2}{2m} + \frac{m}{2}\left(\omega_\perp^2 (x^2 + y^2) + \omega_z^2 z^2\right) + C\vec{l} \cdot \vec{s} + D\left(l^2 - \langle l^2 \rangle_N\right), \tag{2.5}$$

University of Cape Town

where the anisotropy is introduced through the elongation parameter ε introduced by Nilsson [16], which relates the frequencies as

$$\begin{aligned} \omega_z &= \omega_0(\varepsilon)\left(1-\frac{2}{3}\varepsilon\right), \\ \omega_\perp &= \omega_0(\varepsilon)\left(1+\frac{1}{3}\varepsilon\right). \end{aligned} \tag{2.6}$$

The vibrator frequency $\omega_0(\varepsilon)$ is weakly dependent on ε, in order to preserve the nuclear volume, and the elongation parameter satisfies $\varepsilon = (\omega_\perp - \omega_z)/\omega_0$.

2.2.1 The Nilsson parameterization

The parameter ε has a direct physical meaning. The equipotential surfaces for a constant V are a set of points for which $\omega_\perp^2(x^2+y^2)+\omega_z^2 z^2$ is a constant, or $x^2+y^2+\left(\frac{\omega_z}{\omega_\perp}\right)^2 z^2 = K$, is the form of an ellipsoid, with x, y, z semi-axes of 1, 1 and $\frac{\omega_\perp}{\omega_z}$ respectively. The eccentricity of the x-z ellipse, for $\varepsilon > 0$ is:

$$e = \frac{\text{focal length}}{\text{semi-major axis}} = \frac{\sqrt{(\omega_\perp/\omega_z)^2-1}}{\omega_\perp/\omega_z} = \frac{\sqrt{\omega_\perp^2-\omega_z^2}}{\omega_\perp}. \tag{2.7}$$

For small ε, using (2.6) one can expand

$$e = \frac{\sqrt{(1+\frac{1}{3}\varepsilon)^2-(1-\frac{2}{3}\varepsilon)^2}}{1+\frac{1}{3}\varepsilon} \approx \sqrt{1+\frac{2}{3}\varepsilon-1+\frac{4}{3}\varepsilon} \approx \sqrt{2\varepsilon}, \tag{2.8}$$

so the deformation parameter ε is simply related to the eccentricity of the ellipsoid. A positive ε corresponds to a prolate deformation, whereas a negative ε corresponds to an oblate deformation.

Likewise, one can consider the deformed Hamiltonian under perturbation treatment. For small ε, one can write $H = H_0 + \varepsilon h' + \mathcal{O}(\varepsilon^2)$, where H_0 is

University of Cape Town

the spherical Hamiltonian. The perturbation

$$\begin{aligned}
\varepsilon h' &= \frac{m}{2}((\omega_\perp^2 - \omega_0^2)(x^2+y^2) + (\omega_z^2 - \omega_0^2)z^2) \\
&\approx \frac{m\omega_0^2}{2}\left(\frac{2}{3}\varepsilon(x^2+y^2) - \frac{4}{3}\varepsilon z^2\right) \\
&= \varepsilon\frac{m\omega_0^2}{3}\left(x^2+y^2-2z^2\right), \qquad (2.9)
\end{aligned}$$

where the bracket term can be recognized as having the form of the spherical harmonic $P_2(\cos\theta) \sim Y_{20}$. The effective oscillator potential can thus be written as

$$V_{osc} = \frac{1}{2}m\omega_0^2 r^2\left(1 - \frac{2}{3}\varepsilon P_2(\cos\theta)\right), \qquad (2.10)$$

and this can be generalized to non-ellipsoidal nuclear shapes through the inclusion of higher order Legendre polynomials P_λ and their associated 'deformations' ε_λ [1, 17], with the original $\varepsilon \equiv \varepsilon_2$. The association can be made with the expansion given in (1.2) and (1.3). To first order [1]:

$$\begin{aligned}
\varepsilon &\approx \tfrac{3}{2}\left(\tfrac{5}{4\pi}\right)^{1/2}\beta_2 &&\approx 0.946\beta_2 \\
\varepsilon_3 &\approx \left(\tfrac{7}{4\pi}\right)^{1/2}\beta_3 &&\approx 0.746\beta_3 \qquad (2.11) \\
\varepsilon_4 &\approx -\left(\tfrac{9}{4\pi}\right)^{1/2}\beta_4 &&\approx -0.846\beta_4.
\end{aligned}$$

There is an ambiguity in the sign of the octupole deformation ε_3, but it is not often used. The nuclear shape is usually described simply by $(\varepsilon, \varepsilon_4)$ parameterization.

To describe tri-axial shapes, it is customary to define an additional angle γ (equivalent to the γ in equation (1.4) and figure 1.2) and define individual harmonic frequencies as

$$\begin{aligned}
\omega_x &= \omega_0(\varepsilon,\gamma)\left[1 - \frac{2}{3}\varepsilon\left(\gamma + \frac{2\pi}{3}\right)\right] \\
\omega_y &= \omega_0(\varepsilon,\gamma)\left[1 - \frac{2}{3}\varepsilon\left(\gamma - \frac{2\pi}{3}\right)\right] \qquad (2.12) \\
\omega_z &= \omega_0(\varepsilon,\gamma)\left[1 - \frac{2}{3}\varepsilon\gamma\right].
\end{aligned}$$

University of Cape Town

2.2.2 Analytical solutions

In the simple ellipsoidal deformation, the Nilsson Hamiltonian retains cylindrical symmetry, and the solutions can be obtained using cylindrical coordinates. The loss of spherical symmetry and the establishment of a preferred axis removes the energy degeneracy of orbitals with different magnetic substates. States of equal j will have different projections onto the symmetry axis, denoted Ω, the total angular momentum projection is denoted $K = \sum \Omega$ and the parity π. From quantum mechanics, an ellipsoidal nucleus can only rotate if the angular momentum is orthogonal to the preferred axis, so for a single-particle model $K = \Omega$.

In the modified harmonic oscillator Hamiltonian, with the oscillator potential (2.10), the good quantum numbers of the single-particle orbitals turn out to be the primary quantum number of the oscillator N, the number of nodes in the z direction of the wavefunction n_z, and the component of angular momentum along the symmetry axis Λ, where $|K - \Lambda| = \frac{1}{2}$

An exact solution can be derived in this system [1]. The energies

$$\begin{aligned} E(N, n_z) &= \hbar\omega_z \left(n_z + \frac{1}{2} \right) + \hbar\omega_\perp (n_\perp + 1) \\ &= \hbar\omega_0 \left(N + \frac{3}{2} + \frac{\varepsilon}{3}(N - 3n_z) \right). \end{aligned} \tag{2.13}$$

indicate that each N shell will split into $N+1$ discrete states, with n_z taking all possible values from 0 to N.

2.2.3 Small ε expansion

The original shell model was shown to work for spherical shapes, so the terms $\vec{l} \cdot \vec{s}$ and l^2 need also be included in the Nilsson Hamiltonian. The angular momentum j is a good quantum number in the spherical case, and, as one slowly adds a deformation, the residual interaction must remain fairly small. As such, the quantum numbers N, n_z and Λ remain essentially preserved, and are termed *asymptotic quantum numbers* even for intermediate values of ε.

University of Cape Town

This implies that the unperturbed $2j+1$ states of any orbital are going to split into $j+\frac{1}{2}$ evenly spaced orbitals based on their asymptotic quantum number n_z. As the parameter ε gets larger, the interaction between orbitals causes them to deviate from linearity, and a diagonalization becomes necessary to find the energy solutions.

2.2.4 Nilsson diagrams

The most convenient way to visualize the physics underpinning the Nilsson model is through single-particle diagrams. Starting with a region of interest, the individual energies of every $K[N, n_z, \Lambda]$ orbital can be calculated as a function of deformation ε and plotted. As every orbital can contain two particles, by filling up the proton/neutron numbers, the Nilsson diagrams (see figures 2.2 and 2.3) can provide fairly accurate information of the ground state deformation of the nucleus, as well as information regarding low-energy nuclear excitations based on altering the nucleon configuration in the nucleus.

In order to present a simple diagram while allowing for non-ellipsoidal shapes, calculations are often performed with a non-zero hexadecapole deformation ε_4. Mean field calculations [18] in the region $Z \sim 70$, $N \sim 90$ indicate that $\varepsilon_4 < 0$, hence the plots shown are for $\varepsilon_4 = -\varepsilon_2^2/6$. The energy scale is in Nilsson's 'natural' units of $\hbar\omega_0 \equiv 41A^{-1/3}$ MeV

The effects of state mixing are clearly evident in the Nilsson diagrams. Two states of equal spin and parity cannot coexist at a given energy, so when two such trajectories approach each other, they appear to repel and exchange characters, so that after the interaction they carry the character of the state with which the interaction occurred.

The Nilsson model makes a fairly broad assumption regarding nuclear structure: that the primary (core) and the valence (single-particle) aspects of the nucleus can be considered separately. This is applicable if the nucleus is rotating relatively slowly. However, as the nucleus is further excited and the rotational frequency is increased, this interaction become important. The Cranked Shell Model (CSM), developed by Inglis [19], is used when describing nuclear structure at medium to high spin.

University of Cape Town

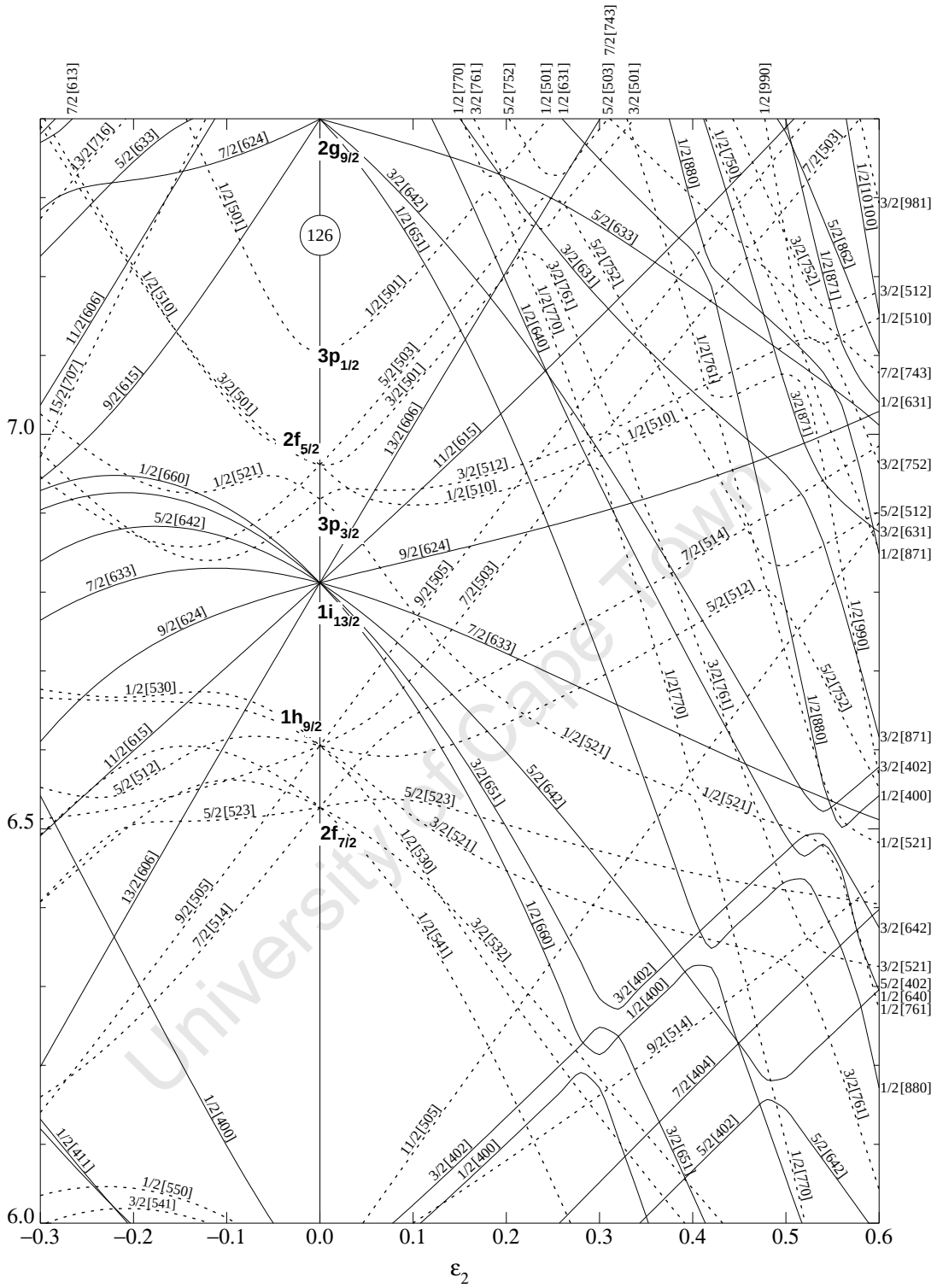

Figure 2.2: Nilsson diagram for neutrons, $82 \leq N \leq 126$ with hexadecapole deformation $\varepsilon_4 = -\varepsilon_2^2/6$ [20]. Dashed lines indicate negative parity and solid lines indicate positive parity states. Single particle energies are in units $\hbar\omega_0$.

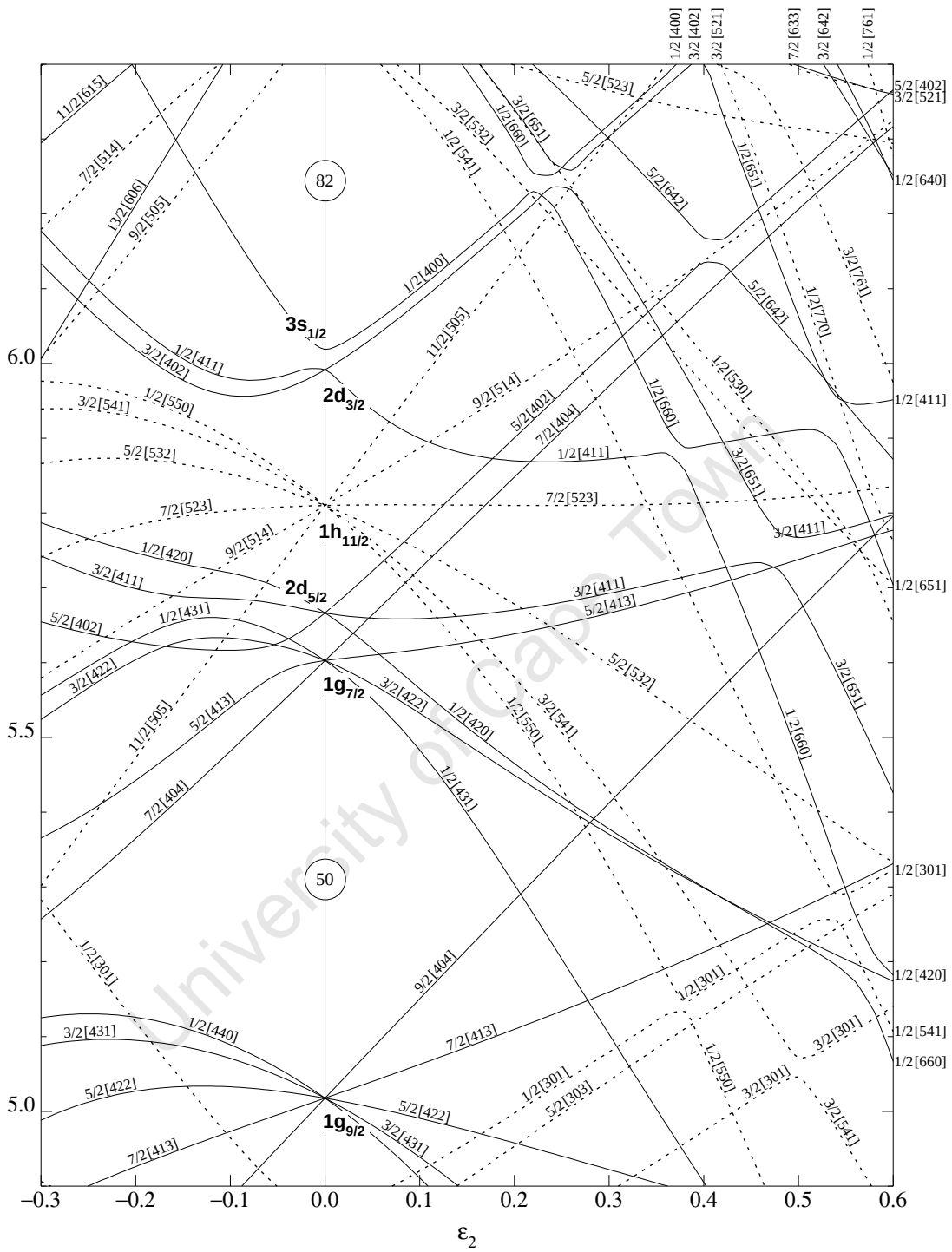

Figure 2.3: Nilsson diagram for protons, $50 \leq Z \leq 82$ with hexadecapole deformation $\varepsilon_4 = -\varepsilon_2^2/6$ [20]. Dashed lines indicate negative parity and solid lines indicate positive parity states. Single particle energies are in units $\hbar\omega_0$.

University of Cape Town

2.3 Nuclear rotation

The simplest mode of excitation in nuclei is through rotation. In quantum systems the energy and angular momentum of a rotation are both discrete, which gives an excellent opportunity to study the underlying structure.

Starting with the simplest case – an even-even nucleus in its ground state, where the spins of all nucleon pairs are anti-aligned – a deformed nucleus will have a preferred axis z. The angular momentum (and therefore axis of rotation) of a collective rotation $\vec{R}$ will be perpendicular to the preferred axis, and as there are no other components, the total angular momentum of the system $\vec{I} = \vec{R}$. The allowed energy states

$$E(I) = \frac{1}{2\mathcal{J}}\vec{R}^2 = \frac{1}{2\mathcal{J}}\vec{I}^2 = \frac{\hbar^2}{2\mathcal{J}}I(I+1), \tag{2.14}$$

where $\mathcal{J}$ is the classical moment of inertia of the nucleus.

The quantization of angular momentum requires that the spin differences between successive levels of a rotational band are integer, and in practice the observed spectra fall into two discrete types. One generally observes bands with $\Delta I = 2$, which correspond to E2 (electric quadrupole) transitions, although band structures with $\Delta I = 1$ (M1 transitions) also occur: in such cases an M1/E2 admixture is usually observed.

It was discovered early on that a fair number of nuclei in the periodic table displayed relatively neat rotational bands. For an ideal nuclear rotor, with energy levels $E(I) \sim I(I+1)$, the in-band E2 gamma energies are $E(I) - E(I-2) \sim (4I-2)$, resulting in a set of evenly spaced gamma ray energies. Such a *picket-fence* spectrum is representative of a pure nuclear rotation.

2.3.1 Cranking Hamiltonian

A certain difficulty arises when trying to describe a nucleus that is rotating fairly fast. In the Nilsson model, the single-particle and the rotational degrees

University of Cape Town

of freedom are considered disjoint, and can be treated separately. However, as one increases the angular frequency of the nucleus, the interactions between the nuclear core and the valence nucleons become substantial.

One of the most direct ways of studying a rotating nucleus is to assume it rotates at a frequency ω, and to set up the coordinate system rotating at the same frequency. The axes retain their orientation with respect to the nuclear shape, and one can write down the transformations between the lab and the intrinsic reference frames.

Upon performing a full derivation [23], the Coriolis and centrifugal interactions come into play. For a rotation around the x axis, the Hamiltonian in the rotating frame satisfies

$$H' = H - \omega I_x, \tag{2.15}$$

where H is the original Hamiltonian and I_x is the spin alignment along the chosen axis. The term H' is sometimes referred to as the Routhian. The presence of the $-\omega I_x$ term removes the time-reversal symmetry from the original Hamiltonian, removing the energy degeneracy from particle orbitals of constant j based on their spin projection m_j.

Within the cranking model, only two useful symmetries remain: In the case of a symmetrical nuclear shape (the expansion of equation (1.2) contains only even λ terms), parity π remains a good quantum number. The other symmetry is termed *signature* α, and it relates to the properties of the nucleonic state under a half-rotation around the cranking axis. The rotation operator is $R_x \equiv e^{-i\pi I_x}$, and applied to single-particle states it allows two solutions $\alpha = \pm\frac{1}{2}$. The signature quantum number (α) is additive between single-particle states.

In the limiting case $\omega = 0$, the unperturbed states (with degenerate energies for $\pm m_j$) do not have signature as a good quantum number. However, linear combinations of states can be set up to have signature $\alpha = +\frac{1}{2}$ and $\alpha = -\frac{1}{2}$, and these basis states can then be used to solve the cranking equation [23]. The equation (2.15) actually decouples into four independent sets of

University of Cape Town

equations based on the different parities and signatures.

2.3.2 Intrinsic variables

To describe nuclear rotations, it is necessary to be able to transform the lab observables into the intrinsic frame of the nucleus. It is convenient to assume a rotating ground (vacuum) state, and treat all excited states of the nucleus as excitations of the vacuum. The solutions to (2.15) are going to be ω dependent, and one can see that the alignment of a rotational band will satisfy $I_x \sim \frac{dE}{d\omega}$. Starting with the classical definition, and considering E2 transitions

$$\hbar\omega(I) \equiv \hbar\frac{dE}{dI} \approx \hbar\frac{\Delta E}{\Delta I} \approx \hbar\frac{E(I+1) - E(I-1)}{2\hbar} = \frac{E_\gamma}{2}. \tag{2.16}$$

However, this is only a first approximation. For a quantum system $\langle I\rangle = \sqrt{I(I+1)} \approx I + \frac{1}{2}$, but a more important aspect is the alignment of the nuclear state I. The ground state of an even-even nucleus always has spin-parity of 0^+, but an excitation of a single-particle nature (taking a nucleon to a higher orbital) can remove the pairing correlations and set up a nuclear state with intrinsic spin K. In such cases $I_x \equiv \langle I\rangle = \sqrt{I(I+1) - K^2}$. The observed spin states of such a band cannot go below K: the lowest such state is termed the *bandhead*.

For a $K = 0$, perfectly rotational ground band the in-band transitions would form a set linearly spaced gamma-ray energies, resulting in a linear relationship between the nuclear spins and the angular frequency ω. However, at higher angular speeds the nucleus will preferentially deform to increase the moment of inertia, and therefore decrease the excitation energies, resulting in a non-linear spin-ω dependence.

Symmetry considerations prevent the spin from having a dependence on even powers of ω [25], and a next order correction is often introduced as a characterization of the vacuum state

University of Cape Town

$$I_{x,0}(\omega) = \mathcal{J}_0\omega + \mathcal{J}_1\omega^3, \tag{2.17}$$

where the $\mathcal{J}_0$ and $\mathcal{J}_1$ are termed the Harris parameters, and are adjustable (for different nuclei). The energy of the vacuum state can therefore be evaluated as

$$E'_0(\omega) = -\int I_{x,0}(\omega)d\omega = -\frac{1}{2}\mathcal{J}_0\omega^2 - \frac{1}{4}\mathcal{J}_1\omega^4 + \frac{1}{8}\frac{\hbar^2}{\mathcal{J}_0}, \tag{2.18}$$

where the constant term is chosen for self consistency. The Harris parameters can be found through a fit of the ground band energies in the nucleus of interest.

In order to compare the experimental data to the theoretical calculation, it is common to evaluate the excitation energies (Routhians) and aligned angular momenta relative to the defined vacuum state

$$e'(\omega) = E'(\omega) - E'_0(\omega) \tag{2.19}$$

$$i(\omega) = I_x(\omega) - I_{x,0}(\omega) \tag{2.20}$$

2.3.3 Quasiparticles

In the previous section the nucleus and its excitations were considered as excitations of the nuclear ground state. In order to regain consistency between this model and the (deformed) single-particle models, the excitation of a nucleon to a higher orbital requires the addition of a nucleon in a higher state, and the removal from its original orbital.

It is convenient to combine these into a particle-hole system, termed a *quasiparticle* [21, 22, 23, 24]. The vacuum state requires filled orbitals up to the Fermi surface, so an even-even nucleus. Odd A nuclei can be described as one- or three- quasiparticle excitations of a nearby even-even vacuum state.

The states below the Fermi surface, e_i, can be treated as hole states. To create a hole costs energy, as the particle has to move up in energy, so the

University of Cape Town

spectrum of the hole states can be constructed as $e_i^h = \lambda - e_i$, as shown in figure 2.4. The particle- and hole-spectra are complementary, so keeping track of both is a double dimensional representation of a system, and results in the double-counting of the energies. The double-counting does however allow for a description of the nucleus based only on the particle and hole excitations above the Fermi surface.

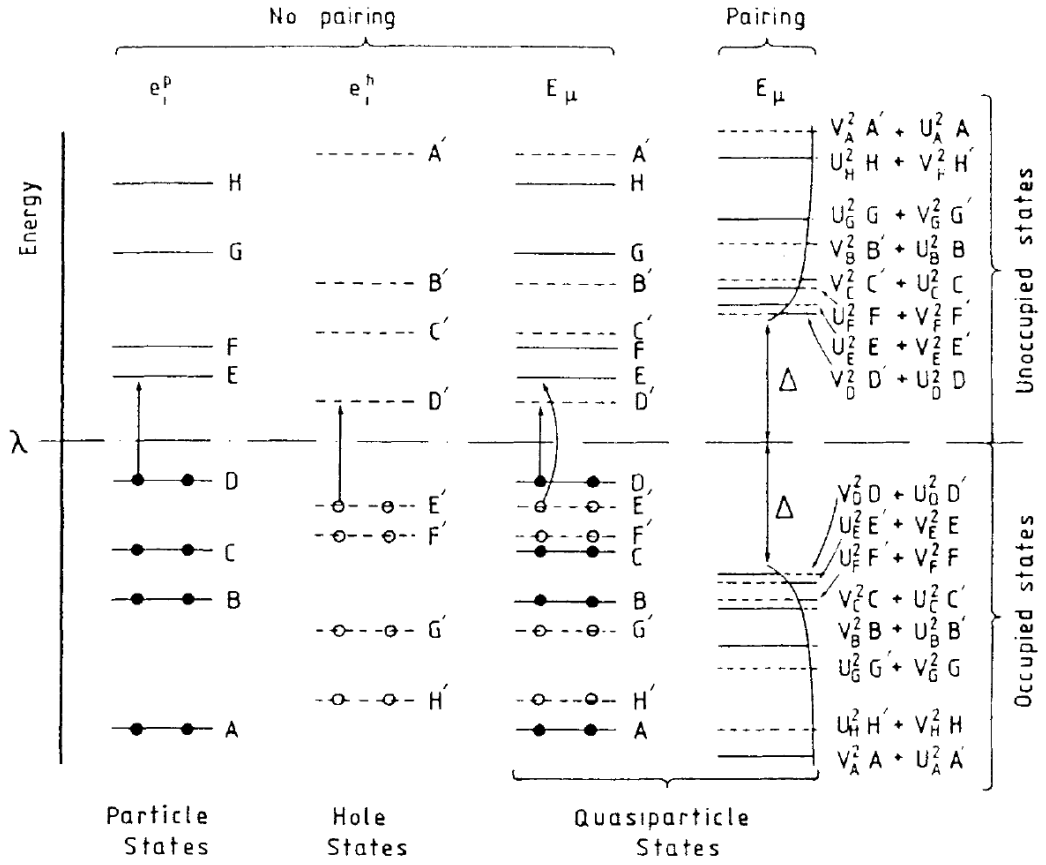

Figure 2.4: A schematic drawing [23] of the quasiparticle excitation. The particle state orbitals are as normal, except relative to the Fermi level λ. The hole states are reflected around the Fermi level. The third column indicates the quasiparticle levels. The cost of exciting a particle D to E, is equivalent to moving the hole E' to D', and is half the cost of taking D to D' and E to E'. The last column includes the Δ gap caused through the breaking of a nucleon pair.

2.3.4 Pairing

From the beginning of the study of nuclear structure, it has been observed that there exists a strong pairing correlation in nuclei. Nuclei with even-even numbers of protons and neutrons are significantly more stable than the even-odd nuclei, and virtually all odd-odd nuclei are β unstable.

This concept of pairing was first formalized by Bardeen, Cooper and Schrieffer in their work on superconductivity [26], where they explained the observed effect through the preference of the fermions to bond into a Cooper pair, effectively reducing the system to a set of interacting bosons. This idea was quickly adopted into nuclear physics [27].

The pairing is implemented as an extra term in the cranking Hamiltonian, as an extremely short range force, that acts only on a pair of fermions that sum to a $J^\pi = 0^+$ boson. Practically this can be understood as the force between two nucleons with identical quantum numbers, but due to Pauli exclusion, this can only exist for nucleons with time-reversed orbits: there is a unique state which can interact with a given state. The strength of this interaction is taken to be a constant Δ.

The introduction of the pairing term introduces a non-diagonal term in the interaction Hamiltonian, which in turn implies that the particle and hole orbitals (solutions of the cranked Hamiltonian) become a mixture of particle and hole states themselves.[1] The pairing interaction only pairs like states, so the diagonal Hamiltonian will divide in to sets of 2×2 non-diagonal parts, dealing with the particle and hole wavefunctions.

Since an orbital of energy e_i has an effective energy of $e_i - \lambda$, the corresponding hole has energy $\lambda - e_i$. If U and V refer to the pure particle and hole wavefunctions, the addition of the pairing term results in the Hamiltonian:

$$\begin{pmatrix} e_i - \lambda & \Delta \\ \Delta & \lambda - e_i \end{pmatrix} \begin{pmatrix} U \\ V \end{pmatrix} = E_i' \begin{pmatrix} U \\ V \end{pmatrix}, \tag{2.21}$$

[1] Although signature remains a good quantum number

University of Cape Town

which produces solutions of

$$E_i' = E_\pm = \pm\sqrt{(e_i - \lambda)^2 + \Delta^2}, \tag{2.22}$$

and the mixtures of the solutions are

$$U_\pm^2 = V_\mp^2 = \frac{1}{2}\left(1 \pm \frac{e_i - \lambda}{\sqrt{(e_i - \lambda)^2 + \Delta^2}}\right). \tag{2.23}$$

It is worth noting that $|E_\pm| > \Delta$, so in order to excite a single nucleon out of the vacuum will require at least 2Δ energy, which in the rare earth region is ~ 2 MeV.

2.4 Random Phase Approximation

The single-particle and rotational models produce excellent agreement with experimental data. The pairing gap does however preclude an explanation of low-lying excitations (below 2 MeV at $\omega = 0$) in even-even nuclei. Most even-even nuclei in the rare-earth region do however have low-lying structures of both positive and negative parities. These are generally termed as quadrupole and octupole vibrations respectively. One manner of explaining the existence of these low lying states, maintaining consistency with quasiparticle model, is the Random Phase Approximation (RPA) [7, 28, 29, 30].

The RPA calculations attempt to account for vibrational excitations by incorporating a separable residual interaction into the system, in addition to the rotating deformed potential. The starting point is the quasiparticle cranking Hamiltonian h_{2qp}, which has an implicit signature symmetry. The residual interaction is introduced by the multipole interaction terms [31]

$$H = h_{2qp} - \frac{1}{2}\sum_{\lambda\mu} \kappa^{\lambda\mu} Q_{\lambda\mu} Q_{\lambda\mu}^\dagger. \tag{2.24}$$

The solutions are found through the re-diagonalization of this Hamiltonian

University of Cape Town

(details in appendix B). When searching for solutions with a well defined signature, it is convenient to only use the interaction terms that preserve that particular signature.

2.5 Electromagnetic transitions

Nuclear de-excitations usually result in the emission of photons. These photons come about due to the time-dependent parts of the Hamiltonian that involve changing electric and magnetic fields. There are two modes: electric (E) and magnetic (M) radiation, named from time variation of charge and current distributions respectively. Angular momentum and parity are preserved by the electromagnetic interaction, and, in notation, the quantity of angular momentum carried is appended onto the radiation mode as EL or ML. The parity change is $(-1)^L$ for E, and $(-1)^{L+1}$ for M transitions.

From semi-classical radiation theory [6, 32], the transition probability per unit time is given by

$$T_{fi}^{\mathrm{E,M}}(L) = \frac{1}{4\pi\epsilon_0}\frac{8\pi(L+1)}{L[(2L+1)!!]^2}\frac{1}{\hbar}\left(\frac{E_\gamma}{\hbar c}\right)^{2L+1} B_{fi}^{\mathrm{E,M}}(L), \tag{2.25}$$

where the function $B_{fi}^{\mathrm{E,M}}(L)$ is the *reduced transition probability*, and contains the specific nuclear information. It is primarily the square of the matrix element of the appropriate multiple operator responsible for producing the relevant photon.

An approximation for the B function is due to Weisskopf, based on the single-particle shell model:

$$B^E(L) = \frac{e^2}{4\pi}\left(\frac{3R^L}{L+3}\right)^2 \tag{2.26}$$

$$B^M(L) = 10\left(\frac{\hbar}{m_p cR}\right)^2 B^E(L). \tag{2.27}$$

However, nuclear de-excitations based on collective effects deviate substantially from these (single-particle) Weisskopf estimates.

University of Cape Town

2.5.1 Branching ratios

In order to perform direct measurement of the reduced transition probability of a particular gamma ray, it is necessary to measure the lifetime of a particular nuclear state. While it is possible to perform such measurements with sufficiently sophisticated equipment [33], some information about the reduced transition probabilities can be inferred from the nuclear branching ratios. Of primary interest to this work is de-excitation through E1 and E2 transitions.

Suppose that a given state can de-excite through the emission of either an E1 or an E2 gamma ray, of energies E_{γ_1} and E_{γ_2}, and probability p_1 and p_2 respectively.[2] The ratio of probabilities $p_1 : p_2$ can be directly inferred through the number of collected events, scaled by the detector efficiency at each energy, and it is also the ratio of total transition probabilities $T(\mathrm{E1})/T(E2)$. Taking the explicit form of 2.25, the ratio of probabilities

$$\frac{p_1}{p_2} = \frac{T(\mathrm{E1})}{T(\mathrm{E2})} = \frac{100}{3}(\hbar c)^2 \frac{E_{\gamma_1}^3}{E_{\gamma_2}^5} \frac{B(\mathrm{E1})}{B(\mathrm{E2})}. \tag{2.28}$$

For analysis of the 'tetrahedral' bands it is customary to consider the ratio $B(\mathrm{E2})/B(\mathrm{E1})$ [34]. Substituting in the relevant numbers, and using MeV as the units of the gamma ray energies[3], one can obtain

$$\frac{B(\mathrm{E2})}{B(\mathrm{E1})} = \frac{100}{3}(\hbar c)^2 \frac{E_{\gamma_1}^3}{E_{\gamma_2}^5} \frac{p_2}{p_1} \approx 1.30 \times 10^6 \frac{E_{\gamma_1}^3}{E_{\gamma_2}^5} \frac{p_2}{p_1} \text{ fm}^2. \tag{2.29}$$

[2] If there are only two decay modes, $p_2 = 1 - p_1$, but other modes may also be available.

[3] This is against the spirit of most of this work where energies are taken in keV, but this does reduce the magnitude of the $E_{\gamma_1}^3/E_{\gamma_2}^5$ term to a manageable range.

University of Cape Town

Chapter 3

Experimental Details

University of Cape Town

The study of nuclear shapes poses a variety of technical obstacles. Nuclear sizes are typically well approximated as $R_0 A^{1/3}$, which for $A \sim 160$ corresponds to a nuclear radius of only 6.5 fm. Direct observation is completely impossible, as photons with sufficiently small wavelengths will have energies of order 100 MeV, which is enough not only to excite the nucleus, but also to knock out several of the constituent nucleons.

One of the common approaches currently used is to create an excited state (several MeV) of the nucleus, and to collect information about the de-excitation processes. The excited nucleus will de-excite through an emission of γ-rays, giving away excess energy and angular momentum. The experimental work here involved gamma-ray (γ-ray) spectroscopy, which involves surrounding the nucleus of interest with high-resolution germanium detectors.

The missing first step is the creation of an excited state of the nucleus of interest. Due to the extreme size and energies involved, it is not practical to try and excite any particular nucleus, but rather to aim at an isotopically pure target and deliver the energy through a collimated beam of light ions. A judicious choice of beam particles and energy can be used to create excited states of a wide variety of nuclei, and, additionally, this also allows the study of nuclei which are not naturally stable.

3.1 Fusion-evaporation reactions

In order to study nuclear properties through gamma-ray spectrometry, it is necessary to prepare the desired nucleus in an energetically excited state, and this is generally performed via some nuclear reaction. One of the most malleable techniques is the fusion-evaporation reaction.

A set of light ions is taken and accelerated through several stages until it reaches a particular energy per projectile. At iThemba LABS, this is performed by the Separated Sector Cyclotron (SSC). The beam of ions is then made to impinge upon a target foil usually made of another, heavier element.

Upon collision the beam and target nuclei have a certain probability (cross section) of interacting sufficiently strongly to fuse all the constituent nucleons into a single bound state. As the reaction is unlikely to be directly head-on, the resulting compound system will normally have a fairly high angular momentum, in addition to an energy excitation of order $\frac{m_T}{M}E_{beam}$ (where m_T is the mass of the target, and M is the mass of the created compound nucleus).

The rapidly spinning, highly excited nucleus then undergoes various forms of de-excitation until it reduces to a stable isotope in its ground state. In the initial stages, the decay is governed by the strong interaction wherein the irregularly shaped compound nucleus settles into a more symmetric shape and it can emit several loosely bound nucleons (or other very light nuclei such as d or α). On average, an emitted neutron carries away $\sim$2 MeV of kinetic energy [35], and (due to its charge and resulting Coulomb interaction) an emitted proton takes away $\sim$8 MeV, while the heavier α particle carries $\sim$15 MeV of kinetic energy. In low-energy reactions, neutron evaporation is the dominant decay channel.

After a time (10^{-19} s), the nucleus becomes strong-interaction stable, and it then continues the de-excitation process through the electromagnetic interaction, via emission of γ rays. It is this nuclear isotope that one can study

University of Cape Town

in detail, as it is created in an excited state with relatively high angular momentum. This nucleus emits photons which carry away energy, and generally one or two units of angular momentum, per γ.

In the very high excitation energy range, the nuclear states form a pseudo-continuum, and the initial γ rays emitted are termed 'statistical gamma-rays', as these γs will have an almost continuous energy distribution, making inferences about the states impossible. Once the excitation energy falls below ~ 10 MeV, the density of nuclear states becomes sufficiently sparse as to allow description in terms of discrete, resolvable energy levels, and therefore, a discrete set of associated transition energies, which can be measured through the observation of the emitted γ rays.

The electromagnetic de-excitation of the nucleus is comparatively slow, usually taking time of the order of 1 ns, although this time can be extended through the population of long-lived isomeric states – nuclear levels where the transition to lower levels is retarded, usually due to a requirement such as high change in spin or nuclear configuration.

Once the nucleus reaches the ground state energy, it will become inert. It could get re-excited by interacting (via fusion or Coulomb excitation) with another beam particle, or, if it is energetically favourable, it could undergo β decay (weak interaction), changing the charge of the nucleus without affecting the number of constituent nucleons. The daughter nucleus in the β decay is normally formed in an excited state, which will (within 1 ns) create a cascade of γs down to the ground state of the new nucleus.

University of Cape Town

3.2 AFRODITE array

The premier accelerator center in South Africa is the iThemba Laboratory for Accelerator Based Sciences (LABS), which houses a $K = 200$ separated sector cyclotron (SSC) with a smaller solid-pole cyclotron (SPC) injector for use in the production of radio nuclides, therapy beams and nuclear physics. Of the various setups used for studying nuclear physics, one is the

AFRODITE (AFRican Omnipurpose Detector for Innovative Techniques and Experiments) gamma-ray spectrometer [36].

The AFRODITE frame is a rhombicuboctahedron (a polyhedron with 18 square faces and 8 equilateral triangular faces). The experimental beam pipe goes through two opposite square faces, leaving space for the placement of up to 16 detectors around the central point. This setup allows for 8 detectors to be placed at 90° to the beam direction, and 4 detectors each at angles of 45° and 135° to the beam line.

3.2.1 Detector system

As the primary function of the array is to perform high-resolution γ-ray spectroscopy, the detectors need to be chosen as to deliver the best possible energy resolution and peak-to-total ratios on individual photons [37, 38]. At this time, most precision γ-ray spectroscopy experiments in the world use High Purity Germanium (HPGe) crystals for the detectors. While germanium detectors do offer excellent energy resolution, it is necessary for them to operate under very low temperatures in order to reduce the thermal excitations of electrons across the fairly small band gap (0.665 eV at room temperature). An effective way of accomplishing this is to use liquid nitrogen (77 K) to cool detectors, by connecting the germanium crystals to a dewar of liquid N_2 by means of a copper rod.

University of Cape Town

CLOVER detectors

The AFRODITE array consists of two types of HPGe detectors. There are 9 primary detectors of the 'clover' type, as used in the EUROGAM and EUROBALL experiments [39, 40, 41]. The clover detector consists of four n-type coaxial HPGe crystals, placed in a 2×2 arrangement (displayed, with dimensions, in figure 3.1), and housed in common cryostat (see figure 3.2).

There are several advantages to this sort of configuration. Firstly, the detector's physical size is increased with relation to the size of the crystals,

allowing for increased space coverage. If a photon strikes a crystal but is not fully absorbed, it may Compton scatter into one of the other clover elements, allowing for the total energy of the photon to be calculated through add-back. Secondly, the physical segmentation allows for finer detail on the interaction point of a γ with the detector, which allows for better Doppler correction. Finally, the scattering of a photon between detector elements can be used to infer information about the polarization of the incoming γ.

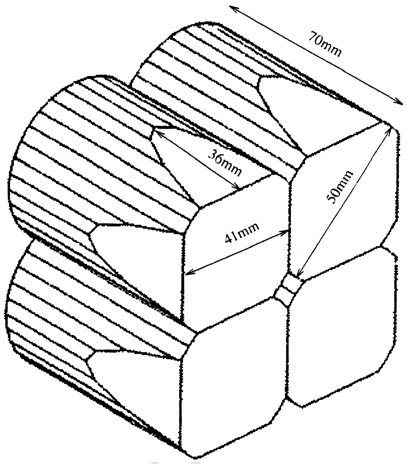

Figure 3.1: Drawing of the HPGe clover detector, displaying the shape and positioning of the individual elements (crystals) [40].

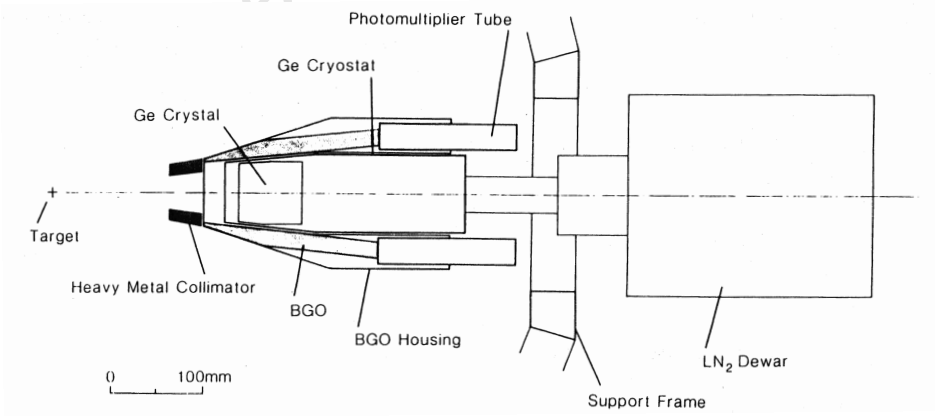

Figure 3.2: Schematic drawing of the clover detector in its protective housing [39, 41]. The BGO detectors surrounding the Ge crystals act as an event veto for escaped photons. The effective solid angle of the detector is 1.34 % of 4π.

Compton suppression

It has been observed that, when using Ge detectors, high energy photons (which undergo multiple Compton scatters before depositing all their energy into the crystal) have a fairly low peak-to-total count rate, due to partial absorption of the energy, when the final scattered photon escapes the detectors. A way of reducing the background incurred in such multiple-scatter events, termed 'Compton suppression', has been developed [42]. In order to detect whether a γ has escaped the HPGe crystal, the detector is surrounded by a another γ-ray detecting material – one with a lower production cost (to make it viable), but with a very high γ-ray detection efficiency.

In the AFRODITE array, the clover crystals are surrounded by bismuth germanate ($B_4Ge_3O_{12}$, usually termed BGO) detectors, which, due to the high density and Z of Bi, has an excellent photopeak efficiency. The BGO crystals are scintillators, emitting visible light when a γ is detected, which is in turn detected by surrounding photomultiplier detectors. If a time-coincidence is detected between the signals in the clover and the BGO shielding, the events are automatically vetoed. Figure 3.3 indicates the difference in cleanness of spectra that can be obtained from Compton-suppression.

In order to prevent false vetoing of events, the BGO detectors are shielded from the target point by a heavy metal collimator (see figure 3.2). The collimators, made primarily of tungsten ($Z = 74$), are shaped to allow γ-rays to enter the Ge crystals, but are sufficiently thick to stop all reaction γs from reaching the BGO detectors.

LEPS detectors

In addition to the clover detectors, the AFRODITE experiment has several Low Energy Photon Spectrometer (LEPS) detectors [43], which can be used in conjunction with the Clover detectors. These detectors are p-type, single cylindrical HPGe crystals, with 60 mm diameter and 10 mm thickness, corresponding to a maximal solid angle of 1.57 % of 4π. The crystals are

University of Cape Town

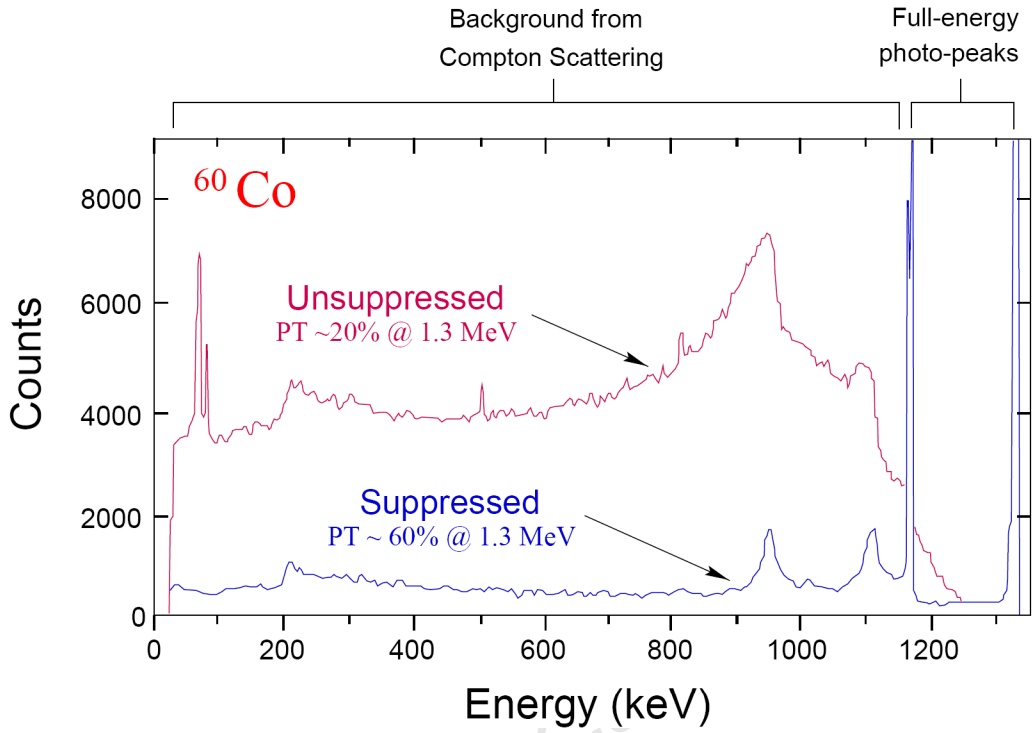

Figure 3.3: Example of spectra obtained with a ^{60}Co source on HPGe detector [44]. The source produces high energy (1173 keV and 1332 keV) γ-rays. The majority of the photons Compton scatter out of the detector, depositing only a fraction of the total energy, and leaving a high, continuous background spectrum. The BGO veto eliminates most of the Compton background.

electrically segmented into four quarters, with individual read-outs. The significantly smaller crystal thickness implies that the LEPS detectors are primarily used only for detecting low-energy γ-rays – up to 200 keV – for which the linear attenuation of Ge is less much than 1 cm [20]. For such low energy photons, the dominant interaction with the crystal is via the photo-electric effect, so an incoming photon has only a small chance of depositing a fraction of its total energy in the crystal. The LEPS detectors are not therefore surrounded by a BGO shield, as the Compton background is already fairly minimal.

When the array was initially set up, careful measurements were made on calibration and absolute efficiencies of the detectors, as shown in figure 3.4.

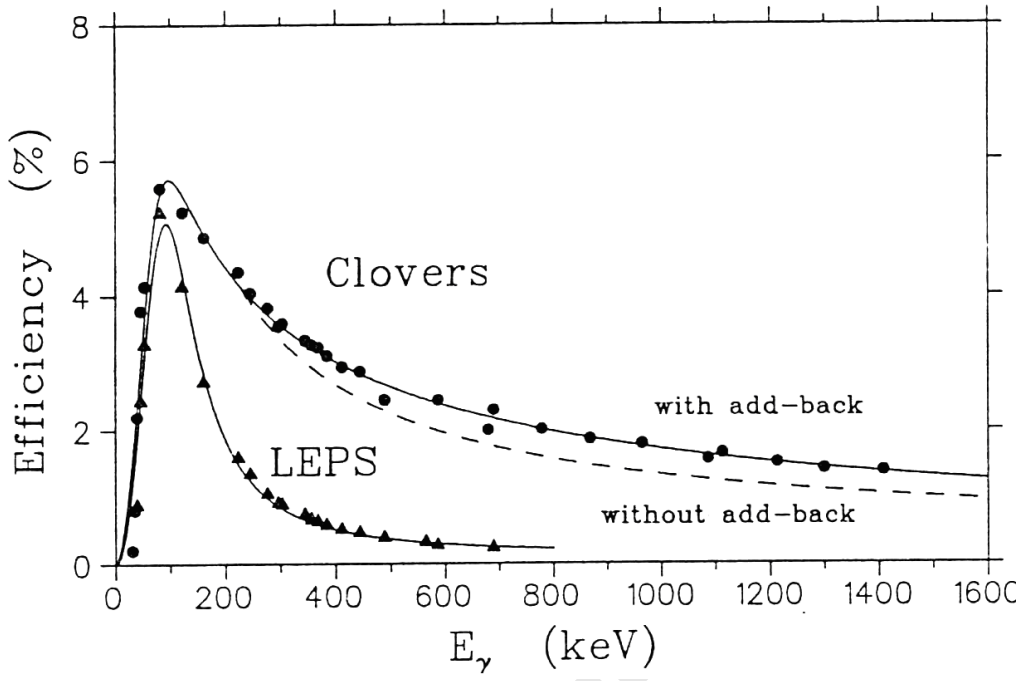

Figure 3.4: The absolute efficiency of AFRODITE, based on 8 clover and 7 LEPS detectors [36]. Data obtained using known strength ^{152}Eu and ^{133}Ba sources.

For every individual experiment, a similar efficiency calibration was also carried out, in order to compensate for any changes in detector geometry, as well as the effect of any absorbers used.

3.2.2 Electronics and data acquisition

While performing the experiment, the individual signals of all the detector outputs need to be read out and processed in order to be stored for analysis. The direct outputs of the clover Ge detectors and their BGO shields are passed through pre-amplifiers and into individual RIS modules. These integrated modules check for Ge 'hit' signals, and if the BGO veto is not present, output a 'clean Ge' signal to the fast trigger unit.

In these experiments, the trigger module collected signals from every RIS module, and (during running of the experiment) it was set to require 2 'clean

Ge' signals in order to register an event (for calibration purposes, the trigger level is set to 1, so non-coincidence data are collected). If two RIS modules reported a good clover hit within a set time coincidence (usually 180 ns), in coincidence with the radio-frequency controlling the cyclotron,[1] a coincidence event is captured. The signal from the fast trigger is then sent out to all the detectors (which have since delayed the input signal) to send the incoming data via a FERA bus to a VME crate. If the trigger does not register an event, the buffers are cleared and signals are discarded.

The LEPS detectors do not have special RIS modules, but are rather sent through a set of amplifiers, a Constant Fraction Discriminator (CFD), an Analog to Digital Converter (ADC) and a Time to Digital Converter (TDC) to convert the signals to digital value and time, and fed into a set of SILENA 4418/V modules for readout. The primary trigger for running AFRODITE involves only the clover detectors, so the SILENA outputs are operated in slave mode.

The VME crate is connected to a linux workstation running the program MIDAS (Multiple Instance Data Acquisition System). For every legal event, the data and time values for all detectors are stored directly onto tape. The incoming raw data are also automatically histogrammed, so that individual crystal performance can be monitored.

A secondary workstation is also set up to perform online analysis of the data. As the data are read in from the VME crates, it can be sent across, where a second instance of MIDAS performs the calibration and add-back on individual detectors. The performances (calibrations, peak widths) of various detectors can be monitored directly.

Once an experiment is finished, the offline analysis is done in a similar manner. The data are sorted using the MTSort language in MIDAS, and EUROGAM-style co-incident spectra and matrices can be produced.

[1]The cyclotron frequency varies depending on the ion being accelerated, but normally it is of the order of 70 ns, or 350 ns if the cyclotron is producing a pulsed beam. The RF requirement does not veto the data collection, but is rather used to set the baseline from which the detector times are measured.

University of Cape Town

3.2.3 Detector calibration

The energy calibration of the detectors is performed using known sources. To calibrate the clovers, a ^{152}Eu source is used, due to its emission of multiple gamma-rays over a wide energy range [45]. The decay spectrum contains at least 10 well separated peaks, ranging in energy from 121.5 keV, all the way to 1408 keV. A medium-strength source ~ 10 kBq is directly placed in front of the detectors (no absorbers), and the raw histograms are accumulated in singles mode. The raw signals are then individually fitted for Gaussian peaks, and a routine is called to match the observed peaks/intensities with the known values for the ^{152}Eu source. A least squares fit is performed to convert the channel number n to the corresponding energy E, using the quadratic relation:

$$E(n) = a_0 + a_1 n + a_2 n^2 \tag{3.1}$$

The absolute energy coefficients are then converted to 0.5 keV per channel (the histograms used have 4096 channels – this allows a study of energies up to 2 MeV), and finally an energy correction is applied for the Doppler shift, based on the v/c of the resultant nucleus (see tables in Appendix A).

The energy calibration of the LEPS detectors is performed using a ^{133}Ba source, as the decay spectrum contains 9 transitions of discrete energies, ranging from 53 keV to 384 keV. The fitting is done in a similar way to that for the clover modules, except the coefficient fitting is performed only up to a linear term, to avoid skewing the data due to the low-efficiency of the LEPS detector above 300 keV. The absolute energy coefficients are then converted to 0.2 keV per channel.

3.3 Reaction selection

In order to study a particular nucleus, it is imperative to select the reaction components and energy in order to maximize the quality of the data that can be collected. In order to limit the number of reaction products, it is necessary

University of Cape Town

to try and use a target that is as isotopically pure as possible. This implies, however, that the target must be a stable nucleus, and not a long-lived radio-active one. This is also in accordance with safety considerations, as 1 mg of radio-active material would be too dangerous to work with. Likewise, the beam particles must also be stable, as most of the projectile nuclei are lost during acceleration, and a radio-active beam would make the accelerator equipment 'hot'.

Given the interest in studying low-lying bands in $N = 92$ nuclei, the identification of suitable reactions became necessary. After surveying the literature, it was decided to study some of ${}^{158}_{66}$Dy, ${}^{160}_{68}$Er and ${}^{162}_{70}$Yb. The feasibility of experiments to study these nuclei was then investigated.

The iThemba LABS cyclotron is best used for producing beams of light ions, so a search was performed on beam/target combinations which may be used to produce the required nuclei (see appendix A for outputs).

The ideal reaction to use is one with a high cross-section, and as pure a fusion-evaporation product as possible, but, as the interest is in the low-lying states and transitions, the nuclear excitation energy ought to be kept reasonably low, so as to allow higher statistics for transitions at the bottom of octupole bands. A countering effect comes about in that lower-energy excitations result in fewer γ-ray cascades, decreasing the coincidence statistics.

The highest cross-sections for fusion correspond to α beams, and, as is shown in figure 3.5, it is possible to obtain a virtually pure ^{158}Dy reaction state through ^{156}Gd$(\alpha, 2n)$ at 27 MeV.

Similarly, to study ^{160}Er, α reaction cross-sections are high, but the low natural abundances of ^{158}Dy and ^{160}Dy (0.1% and 2.4% respectively) were prohibitive in the construction of an isotopically pure target. It was decided to use the ^{152}Sm(^{12}C,4n) reaction at 62 MeV instead (see figure 3.6).

In early 2009 I submitted a proposal to study ^{158}Dy and ^{160}Er. While waiting for the experiments to be performed, I also received data from an earlier experiment which studied the $N = 88$ nucleus ^{156}Er via the ^{147}Sm(^{12}C, 3n) reaction at 63 MeV (see figure 3.7).

University of Cape Town

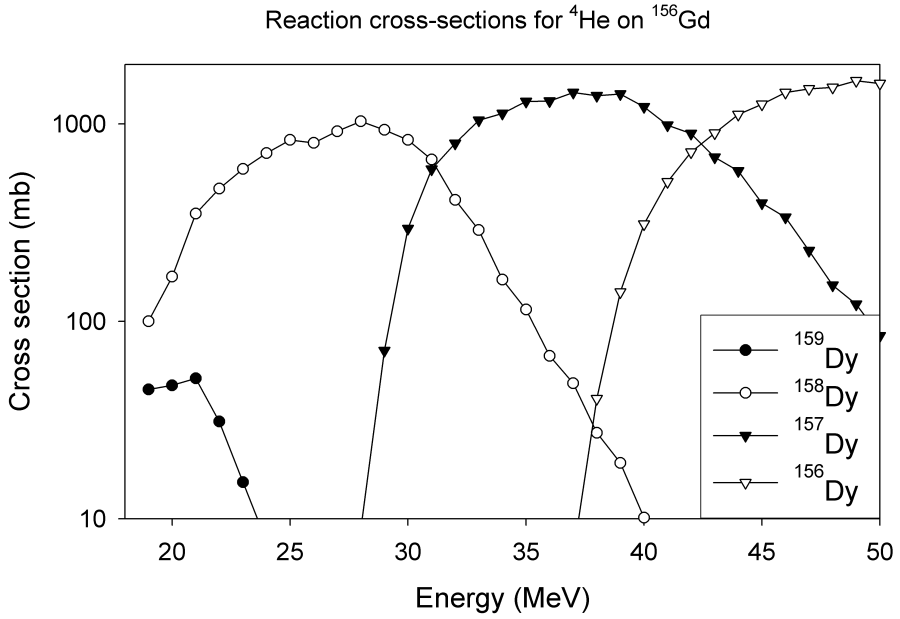

Figure 3.5: The relative particle yields for an α beam on a ^{156}Gd target.

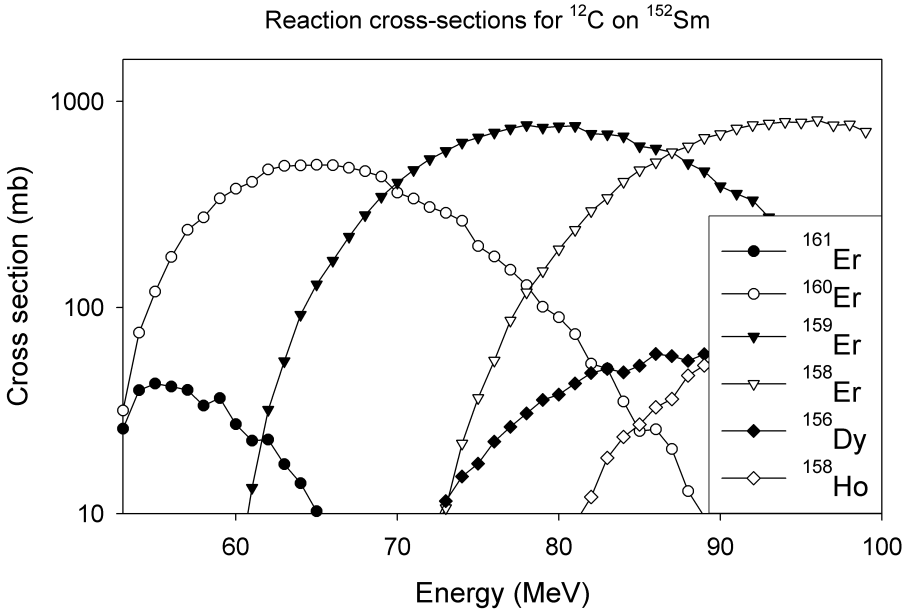

Figure 3.6: The relative particle yields for a ^{12}C beam on a ^{152}Sm target.

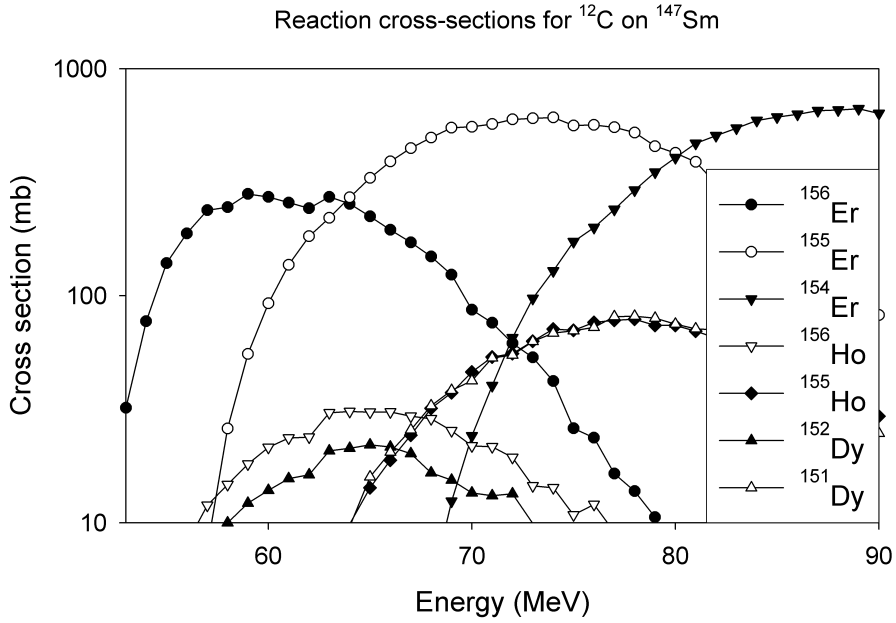

Figure 3.7: The relative particle yields for a ^{12}C beam on a ^{147}Sm target.

3.4 Data analysis

The calibrated data are sorted into time-coincident $\gamma\gamma$ matrices. The data are converted and analyzed using the `Radware` software package [46]. The program `escl8r` is used to construct level schemes of the various data sets, based on the coincidence matrices, energy and efficiency calibration as well as a manual background subtraction. The program calculates the relative gamma-ray intensities and allows for direct viewing of fit-subtracted spectra. The plots of spectra are also generated through the `Radware` package.

3.4.1 γ-ray classification

As has been mentioned in section 2.5, the gamma-rays emitted during the nuclear de-excitation can be produced via electric or magnetic interactions, and can carry discrete quantities of angular momentum. The spin-parity (J^{π}) of a gamma-ray carries valuable information when it comes to the construction

of level schemes. While the in-band transitions for most structures in nuclear physics exclusively involve E2 or M1 transitions, the character and multipolarity of out-of-band transitions need to be determined before the spin-parity assignments of a band can be performed.

It turns out that the intrinsic properties of a gamma-ray cannot be inferred on an individual basis by the HPGe detectors. However, for multi-detector arrays a method known as Directional Correlation from Oriented nuclei (DCO) has been developed [47, 48], which may be applied for the AFRODITE array.

Upon creation, in a fusion-evaporation reaction, the excited nuclei will be in some unknown spatial configuration. For any specified configuration, the distribution of the emission of gamma-rays will not be isotropic, but will depend on the orientation of the initial states and the multipole matrix elements between the initial and final states. The angular distribution of the γ-rays related to a particular transition can be used to infer the J^π of that transition. As the orientation of the emitting nuclei cannot be determined directly, the total angular distribution of a single transition cannot be used to identify it.

A way past this is to consider a cascade of γ-rays, where the character of some of the transitions is known. Given a strong, known transition (usually taken as an E2), the angular distribution of the collected gamma-rays will be related to the intrinsic quadrupole orientation of the initial nuclear state. For two transitions γ_1 and γ_2, and detector systems set up at angles θ_1 and θ_2 from the beam direction, a DCO ratio can be defined as

$$R_{DCO} = \frac{\epsilon_{\gamma_2}(\theta_1)\epsilon_{\gamma_1}(\theta_2)}{\epsilon_{\gamma_2}(\theta_2)\epsilon_{\gamma_1}(\theta_1)} \cdot \frac{I_{\gamma_2}(\theta_1) \text{ gated by } I_{\gamma_1}(\theta_2)}{I_{\gamma_2}(\theta_2) \text{ gated by } I_{\gamma_1}(\theta_1)}, \tag{3.2}$$

where $\epsilon_{\gamma_i}(\theta_j)$ is the detector efficiency for the detection of γ_1 by a detector placed at θ_j from the axis. When dealing with identical detectors (which the clovers are approximated as), the absolute efficiency for a particular energy is constant for all detectors, and all the ϵ terms are assumed to cancel to 1.

A quadrupole transition decaying to the state from which the known E2

University of Cape Town

transition emanates will have an angular distribution approximately equal to the angular distribution of the known transition, and the DCO ratio will equal 1. For a dipole transition, compared to the E2, the ratio will represent a different value, which depends on the angles θ_1, θ_2, which are forced by the geometry of the array.

In the AFRODITE array four clover detectors are placed at 45° (backward) from the beam direction, and the rest are placed at 90° to the beam axis. For a stretched dipole transition, when compared to a stretched quadrupole, the DCO ratio should be approximately 0.7, with an in between value characteristic of an E/M (quadrupole/dipole) admixture.

From a practical point of view, when the collected data are being sorted into coincidence matrices for analysis, a second (asymmetric(coincidence matrix can also be created by histogramming energies of gamma-rays collected at 45° verse those at 90°. The programs in the `Radware` package can then used to set gates and evaluate the areas contained with the transposed peaks, in order to obtain directional correlation data.

The DCO method is not, however, always applicable. The gated peaks on the asymmetric matrix will always be a factor of 4 smaller, making character identification of weak transitions prone to very high uncertainties. Secondly, for level schemes that contain very dense peaks, wherein a strong transition has an energy similar to one in the cascade which is to be investigated, the values obtained for the DCO ratio cannot be relied upon.

University of Cape Town

Chapter 4

Experimental Results

University of Cape Town

The nuclei in the rare-earth region have been studied in previous experiments, and the structure of the high-spin states has been established fairly well. Likewise, measurements of the low-spin states have been performed using scattering experiments. The main goal of the experiments performed at AFRODITE was not so much to extend the known bands in energy, as to search for low-energy states (up to the bandheads) and investigate the γ transitions linking them, in order to infer both band structures, and the strength of the in- and out- of band transitions linking these states. Three nuclei have been studied for this work: the $N = 88$ nucleus ^{156}Er, and two $N = 92$ nuclei ^{160}Er and ^{158}Dy.

The naming/numbering of the bands has been done so as to try maintain consistency with the latest established data sets [20, 49], the relevant experimental papers, and to keep some continuity between the similar structures in the related nuclei.

4.1 Pre-Analysis

In order to perform the analysis, the data collected in the form of a gamma-gamma coincidence matrix need to be modified, to take into account the

underlying physics and efficiencies of the HPGe detectors. This is done within the `Radware` software package [46].

4.1.1 Timing and random subtraction

During the experiments the data are taken (energies and times of all detectors are read out and stored) if at least two Clover detectors fire within a fixed time (usually 150-180 ns) of each other. The gamma-rays thus collected can be thought of as prompt gamma-rays (from the reaction), as well as a mixture of random gamma-rays from other sources, forming a flat background (in time). By comparing the arrival times of the gamma-rays with the RF timing system of the accelerator, it is possible to remove some of the spurious data. This process, termed *random subtraction*, is treated as follows:

Let p_i be the probability of a prompt gamma-ray in channel i, and r_i the (time independent) probability of a random event. For N prompt and M late gamma-rays:

- The symmetric time-gated matrix A will contain both prompt and random gamma-rays in each channel, giving $(p_i + r_i)(p_j + r_j)N^2$ counts in channel (i, j).
- An asymmetric time-gated matrix B of non-coincidence data (matrix constructed of one prompt and one late gamma 'coincidence') should then contain $(p_i + r_i)(r_j)NM$ counts in channel (i, j).
- The symmetric, random subtracted matrix defined as $A - \frac{N}{M}(B + B^T)$ will then contain $(p_i p_j - r_i r_j)N^2$ counts in channel (i, j).

The primary flaw with this method is the prerequisite of a number of statistical nuclei: one requires $r_i \ll p_i$, and that $\frac{N}{M}$ be sufficiently small as to not introduce artifacts in the data during the random subtraction.

The beams provided by the iThemba accelerator ran with an RF separation of 67.6 ns (for a ^{12}C beam). Often it is possible to get a pulsed beam: the

University of Cape Town

accelerated particles only come in 1 of every 5 pulses, giving a separation of 338 ns. This gives a better timing resolution, but at the cost of a reduced event count – if multiple nuclear interactions occur within the same beam-pulse, the gamma-rays collected during that event will not be representative of a single de-excitation cascade by a single nucleus.

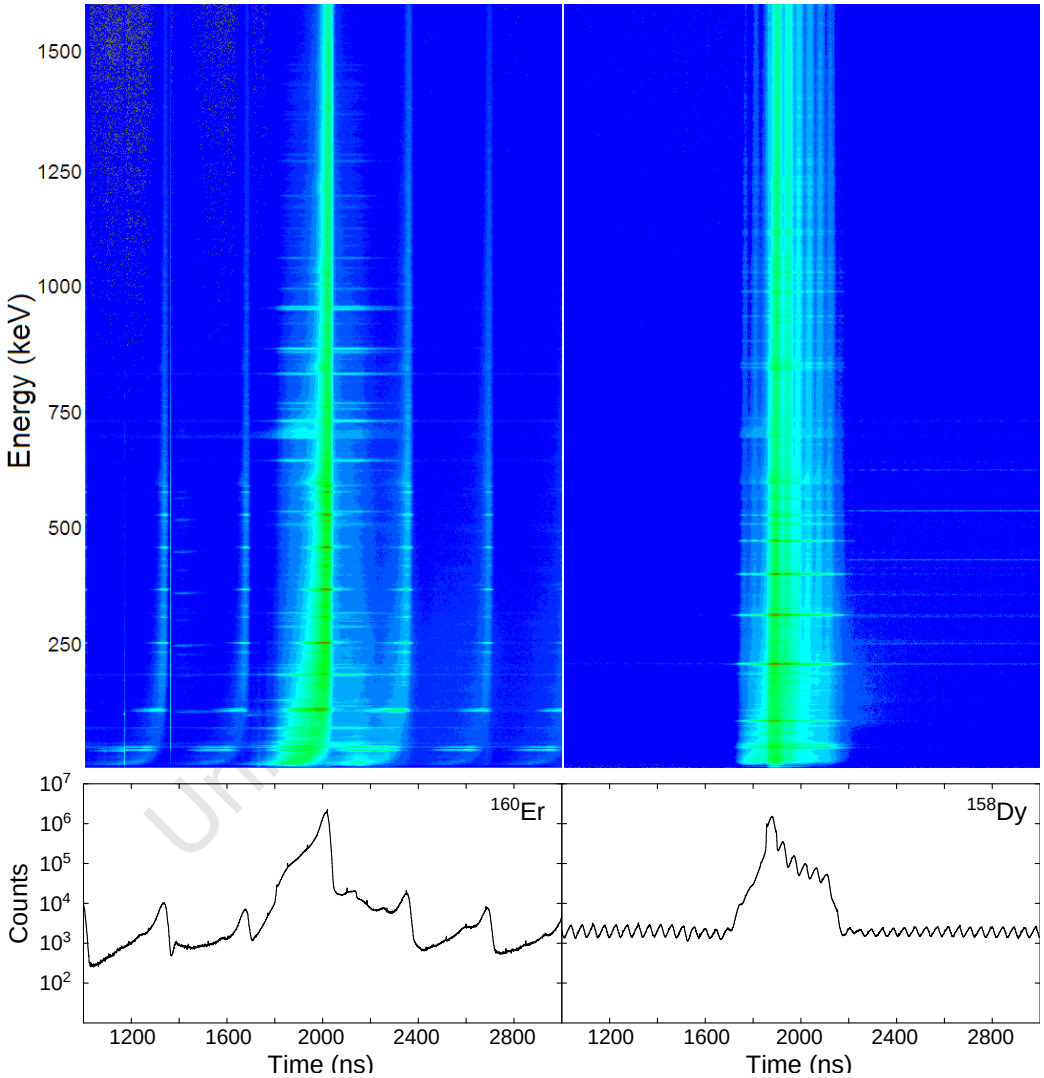

Figure 4.1: Representative energy-time and time-projection plots for data taken with a pulsed beam (^{160}Er) compared to an un-pulsed beam (^{158}Dy), showing the effect of merging of consecutive beam pulses on the time-spectra.

For experiments performed without pulse-selection, the beam pulse separation was less than the maximal drift time for charge within the HPGe detectors [37]. Thus it became impossible to separate the gamma-rays collected from neighbouring beam pulses, and the tight window for defining prompt gamma-rays had to be abandoned. This increases the effective r_i fraction. Additionally, random coincidence probability r_i now differed inside and outside the 'prompt' region, and due to low number of detectors (two detectors were required in coincidence to register an event – the in/out of the coincidence matrix required event multiplicity of at least 3) the count rate outside the prompt region resulted in a high value of the $\frac{N}{M}$, which can make full random subtraction impossible. In such cases, a partial subtraction can be performed, and the analysis proceeded to the next stage.

The total projection of a random-subtracted gamma-gamma matrix from the ^{156}Er experiment is shown in figure 4.2, panels a) and b). It is evident that the main peaks of the spectrum are easily distinguishable, but there is also a fairly high level of continuous background generated through incomplete Compton suppression (see figure 3.3). As such, there is some level of coincidence between every pair of gamma-rays, making analysis based on the coincidence measurements unjustified.

By taking the background as essentially statistical, the majority of the continuum can be removed, and the working total projection spectrum can be reduced to that of figure 4.2 c).

It can be observed that in addition to the strong peaks from the ground band of ^{156}Er, there are also clear peaks at 137 keV, 266 keV and 366 keV, which come from the ground state band of ^{156}Dy. This is not due to direct production, but rather from β decay of ^{156}Er to ^{156}Ho ($\tau_{1/2} \approx 19.5$ minutes) and then to ^{156}Dy ($\tau_{1/2} \approx 56$ minutes) [49]. The gamma-rays from the holmium are not as visible, due to that decay not usually producing a cascade of gamma-rays, and to the detector absorbers taking care of most of the photons of less than 100 keV. By considering the summed gates over the main ^{156}Er transitions (sum of 344 keV, 453 keV, 543 keV and 619 keV gates), shown in figure 4.2 d), the ^{156}Dy lines disappear.

University of Cape Town

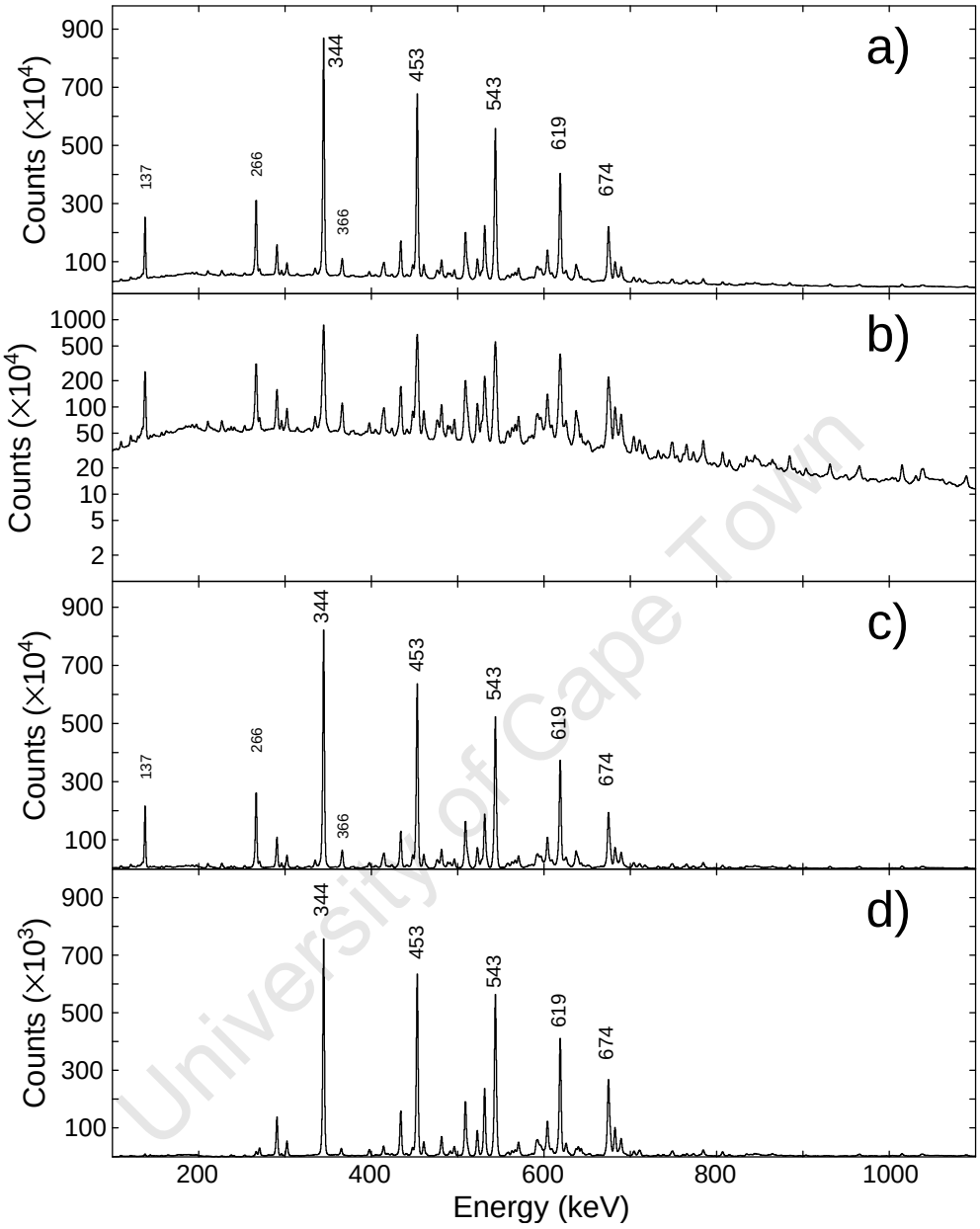

University of Cape Town

Figure 4.2: The calibrated, ungated data obtained for the experiment in a) linear and b) logarithmic form, showing the continuous gamma-ray background. Spectrum c) shows the background-subtracted data, and d) is the gated spectrum on the first four ground state transitions in ^{156}Er.

4.1.2 Existing level schemes

Information about the nuclear excitations has been put in the form of level schemes since the beginning of gamma-ray spectroscopy. The known data are regularly extended and updated, as modern detector arrays are developed, or (as in this case) when a very particular measurement is performed. When studying nuclei, it is prudent to start with the information that is already known about them.

At a similar time that the ^{156}Er experiment took place at iThemba LABS, another experiment was performed at Argonne National Laboratory using the Gammasphere spectrometer using the ^{114}Cd(^{48}Ca,6n) reaction, and had the benefit of 100 HPGe detectors, resulting in the publication of recent experimental results for this nucleus [50, 51]. Partial level schemes from those publications are shown in figures 4.3, 4.4.

The higher-N erbium isotopes have a good history of providing new physics, and have been well studied at high spin. ^{158}Er was the first nucleus to display back-bending [52], and breaks of collectivity at high spin [53]. For ^{160}Er, several structures have also been studied to high spin ($\sim 50\hbar$) in the late 1980s [54]. Recent medium-spin work has also been done on the positive parity vibrational states [55] using the ^{159}Tb(^{6}Li,5n) reaction at 52 MeV. Incidentally, another study of ^{160}Er has been performed at the Gammasphere array to study even higher spins using the ^{116}Cd(^{48}Ca,4n) reaction at 215 MeV, with the results published in 2011 [56]. Partial published level schemes are shown in figures 4.5, 4.6.

The band structure of ^{158}Dy has, however, not been studied extensively. In the 1960s and 1970s low spin data were obtained through light beam reactions and beta decay of ^{158}Ho [20, 49]. Additionally, there have been several high-spin studies [57, 58], shown in figures 4.7, 4.8. Since no intermediate excitation studies have been performed recently, several new band structures have been populated in this experiment.

University of Cape Town

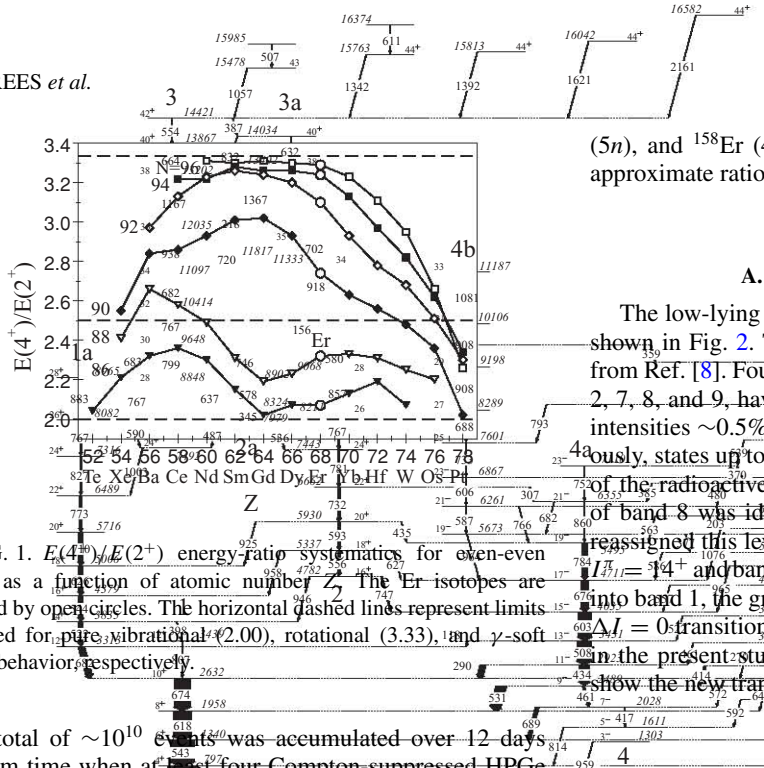

FIG. 1. $E(4^+)/E(2^+)$ energy-ratio systematics for even-even nuclei as a function of atomic number Z. The Er isotopes are denoted by open circles. The horizontal dashed lines represent limits expected for pure vibrational (2.00), rotational (3.33), and γ-soft (2.50) behavior, respectively.

A total of $\sim 10^{10}$ events was accumulated over 12 days of beam time when at least four Compton-suppressed HPGe detectors fired in prompt time coincidence. In the offline analysis, $\sim 10^{11}$ quadruple-coincident events (γ^4) were unfolded from the raw data and replayed into a Radware format four-dimensional hypercube [11,12] for subsequent analysis. The three most strongly populated nuclei in the ^{150}Nd(^{11}B,xn) reaction at Gammasphere [?]. Figure 1: $E(4^+)/E(2^+)$ energy-ratio systematics for even-even nuclei as a function of atomic number Z. The Er isotopes are denoted by open circles. The horizontal dashed lines represent limits expected for pure vibrational (2.00), rotational (3.33), and γ-soft (2.50) behavior, respectively. reaction at Gammasphere [50]. ^{156}Er ($5n$), ^{157}Er ($4n$), and ^{158}Er ($4n$), were observed in the hypercube at an approximate ratio of 0.5:1.0:1.0.

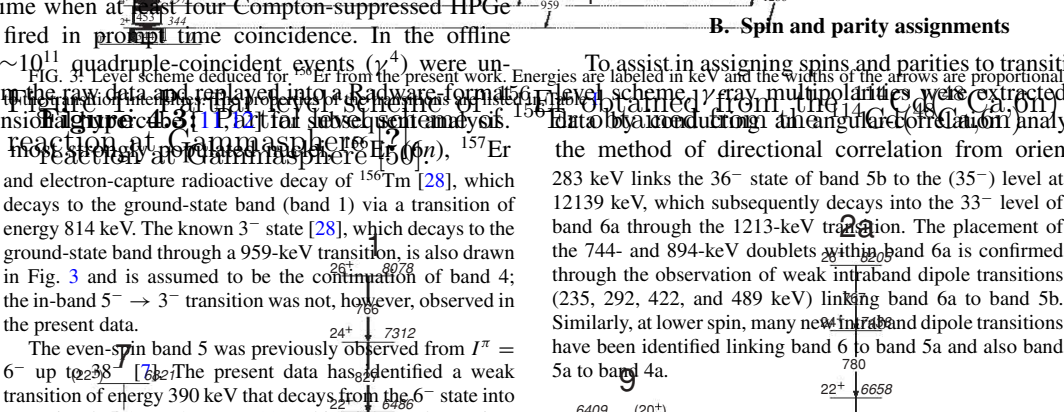

FIG. 3. Level scheme deduced for ^{156}Er from the present work. Energies are labeled in keV and the widths of the arrows are proportional to transition intensity. Dashed lines indicate tentative placements. Spin and parity assignments are discussed in the text. Figure 3: Partial level scheme of ^{156}Er obtained from the ^{144}Gd(^{16}O,4n) reaction at Gammasphere [?].

A. New non-yrast levels in ^{156}Er

The low-lying levels in ^{156}Er, deduced from this work, are shown in Fig. 2. The band-numbering convention is adopted from Ref. [8]. Four weakly populated band structures, labeled 2, 7, 8, and 9, have been established in ^{156}Er with maximum intensities $\sim$0.5% of the 344-keV $2^+ \rightarrow 0^+$ transition. Previously, states up to 4^+ were seen in bands 2 and 7 from studies of the radioactive decay of ^{156}Tm; in addition, the 3^+ level of band 8 was identified [13,14], although subsequent work reassigned this level to 4^+ [15]. Band 2 has been extended to $I^\pi = 14^+$ and band 7 to $I^\pi = (22^+)$. Both of these bands decay into band 1, the ground-state band, via a series of $\Delta I = 2$ and $\Delta I = 0$ transitions. The levels of band 9 are newly identified in the present study. The coincident γ-ray spectra of Fig. 3 show the new transitions in bands 8 and 9, respectively.

B. Spin and parity assignments

To assist in assigning spins and parities to transitions in the level scheme of ^{156}Er obtained from the ^{144}Gd(^{16}O,4n) reaction at Gammasphere [?]. Figure 2: Partial level scheme of ^{156}Er obtained from the ^{144}Gd(^{16}O,4n) reaction at Gammasphere [?]. data obtained from an angular-correlation analysis using the method of directional correlation from oriented states

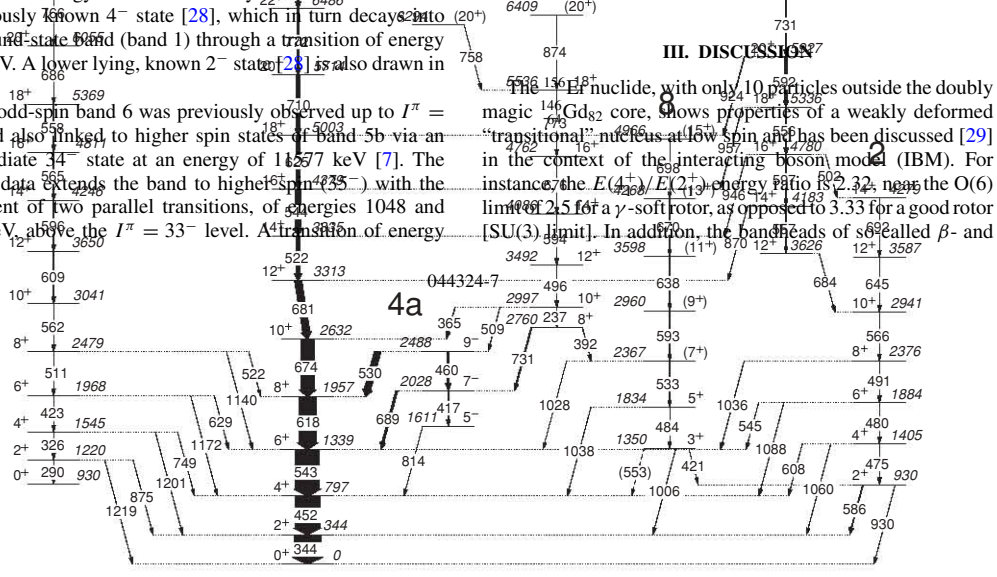

FIG. 2. Partial level scheme, up to $I = 26$, deduced for ^{156}Er from the present work and showing new bands 2, 7, 8, and 9 in relation to known bands. Energies are labeled in keV and the widths of the arrows are proportional to the transition intensities. Figure 4: Partial level scheme of ^{156}Er obtained from the ^{144}Gd(^{16}O,4n) reaction at Gammasphere [?].

III. DISCUSSION

The Er nuclide, with only 10 particles outside the doubly magic $^{146}_{64}$Gd$_{82}$ core, shows properties of a weakly deformed "transitional" nucleus at low spin and has been discussed [29] in the context of the interacting boson model (IBM). For instance, the $E(4^+)/E(2^+)$ energy ratio is 2.32, near the O(6) limit of 2.5 for a γ-soft rotor, as opposed to 3.33 for a good rotor [SU(3) limit]. In addition, the bandheads of so-called β- and

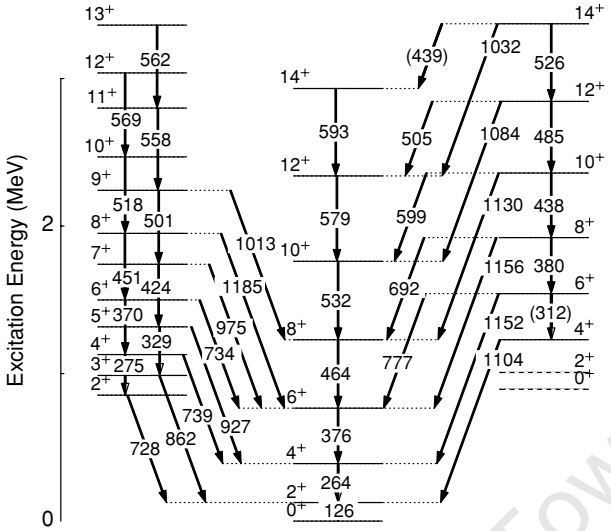

Figure 4.5: Partial level scheme of ^{160}Er obtained from the ^{159}Tb(^{6}Li,5n) reaction at Stony Brook [55].

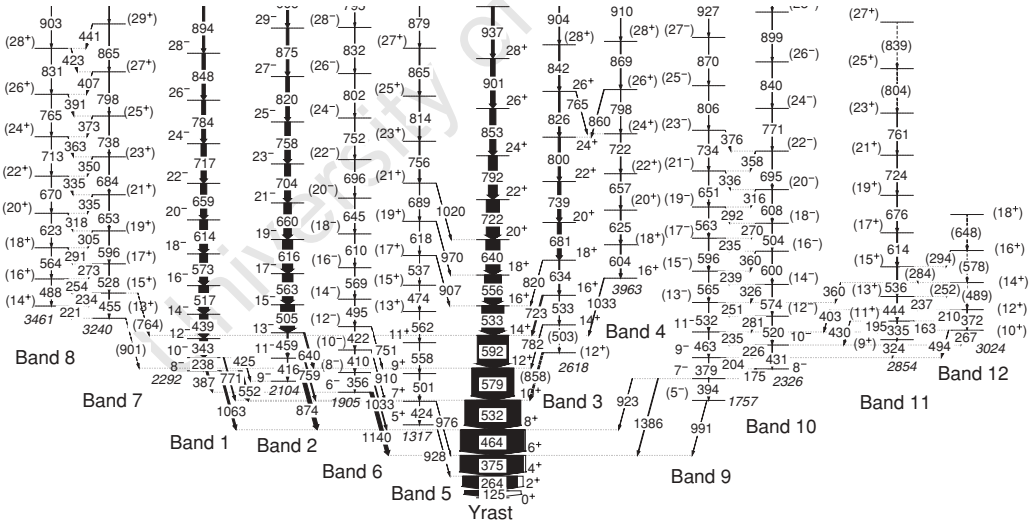

Figure 4.6: Partial level scheme of ^{160}Er obtained from the ^{116}Cd(^{48}Ca,4n) reaction at Gammasphere [56].

University of Cape Town

133- and 158-keV γ ray for the band, 5 and 6. The $E2$ transitions and interband $M1$ transitions are shown.

the DCO ratios. Since the DCO ratio between 90° and 32° in our experiment setup was most sensitive, we used the DCO ratio defined by the following equation:

$$R_{DCO} = \frac{I(\gamma_1{:}32° \text{ or } 148° \text{ gated by } \gamma_2{:}90°)}{I(\gamma_1{:}90° \text{ gated by } \gamma_2{:}32° \text{ or } 148°)}.$$

The angle of 32° was equivalent to that of 148° for the DCO analysis [26]. The stretched $E2$ transitions close to the γ

feed band 4. The lowest state of band 4 feeds the 5^+ state via a 448-keV transition (see, Fig. 2). Since the 448-keV transition is assigned as a ΔI=1 transition (see, Fig. 3), the possible spin and parity of the lowest state are J^π=(6^+) or (6^-). If the parity was positive, one could observe $E2$ transitions linking between the lowest state and the 4^+ state of band 1 in the experiment. The most probable spin and parity are hence J^π=(6^-). A 2476-keV excitation energy state of band 2 was assigned as J=(10, 11) in previous studies [18]. However this state is assigned as J^π=(10^-) in the present experiment because this state feeds to the (8^-) level of band 4 through a 380-keV-γ ray which is assigned as an $E2$ transition. Band 2

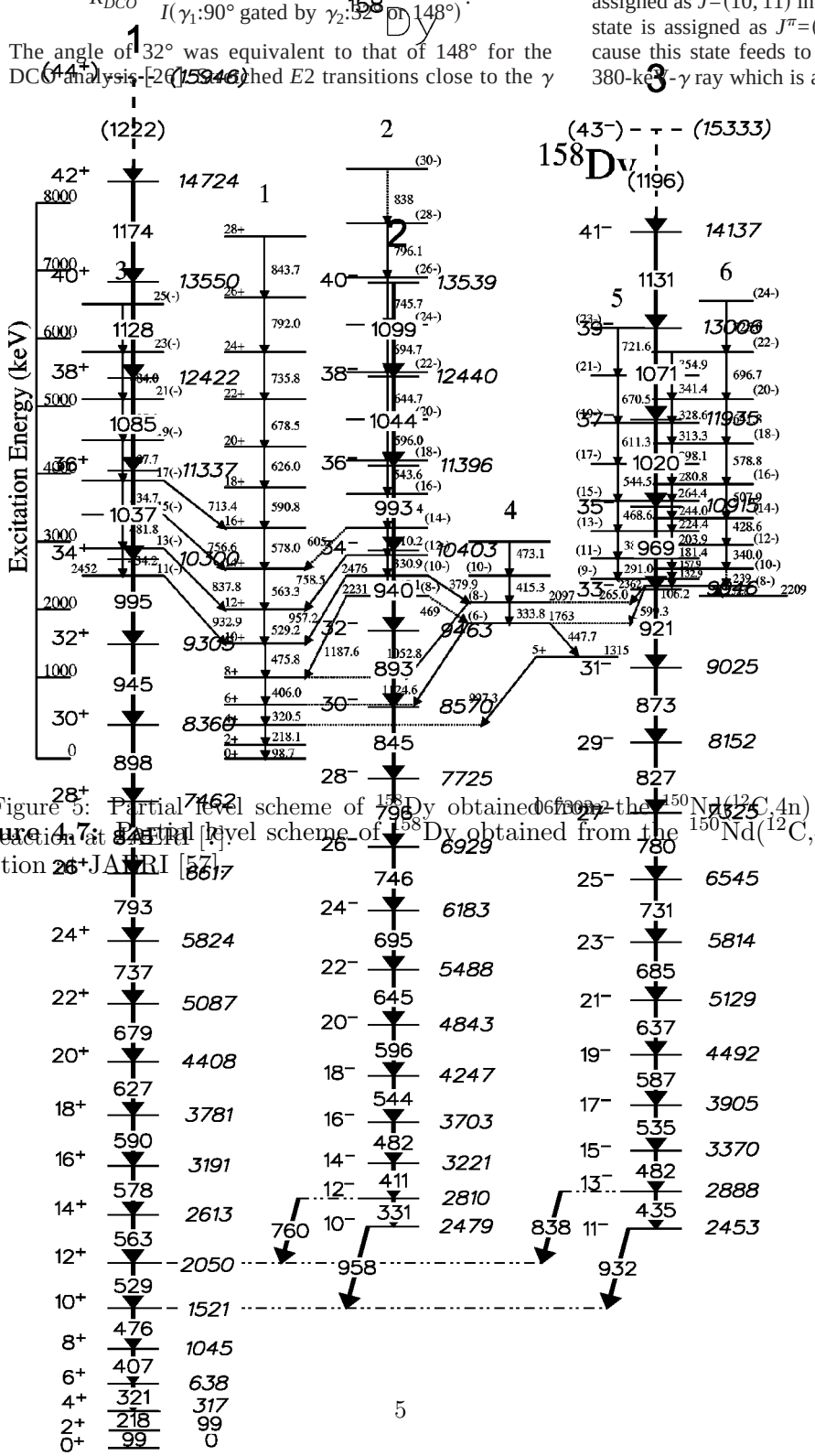

FIG. 5. The level schemes deduced for ^{158}Dy and ^{159}Dy. Energy values are in kiloelectronvolts, tentative transitions are indic lines and tentative spin, and parity and level energies are given within parentheses.

Figure 5: Partial level scheme of ^{158}Dy obtained from the ^{150}Nd(^{12}C,4n) reaction at Laboratori Nazionali di Legnaro, Italy [58].

Figure 4.7: Partial level scheme of ^{158}Dy obtained from the ^{150}Nd(^{12}C,4n) reaction at JAERI [57].

Figure 4.8: Partial level scheme of ^{158}Dy obtained from the ^{150}Nd(^{12}C,4n) reaction at Laboratori Nazionali di Legnaro, Italy [58].

nuclei, even though the low-spin yrast structure changes from weakly prolate deformed in the light Dy isotopes to strongly prolate deformed for the heavier ones [41]. This interpretation is in agreement with theoretical predictions regarding the oscillatory nature of the band crossing interaction strength with particle number [42–44]. However, more recent theoretical work aimed specifically at the systematics of the yrast bands in even-N Dy isotopes, such as those using the

angular-momentum-projected Tamm-Dancoff m still predict a more noticeable change in mome (weaker band-crossing interaction strength) for th crossing (A_pB_p) than is experimentally observed

In Fig. 10, the alignment of the yrast s ^{157,158,159}Dy and some neighboring isotones obse spins are compared. There are many common these plots, including a gradual and consistent

4.2 $^{156}_{68}$Er

The nucleus $^{156}_{68}$Er is different from the other nuclei in this section, as it contains only 88 neutrons, rather than 92. The presence of 6 extra neutrons above the magic number 82 corresponds to filling the 3 steep Nilsson orbitals ($[541]\frac{1}{2}$, $[530]\frac{1}{2}$ and $[532]\frac{3}{2}$ – see figure 2.2) up to a deformation of $\varepsilon \approx 0.2$, while the 4 extra $1h_{11/2}$ protons above the closed sub-shell of $Z = 64$ result in the nucleus having a rather transitional character (neither a good rotational nor vibrational ground band) [50]. The excitations of $N = 88$ nuclei show a structure distinct to those of $N = 90$ and $N = 92$ nuclei, as can be seen in figures 5.3, 5.4 and 5.5 in the next chapter.

The experiment to study ^{156}Er took place at iThemba LABS in 2007/2008 using the ^{147}Sm(^{12}C, 3n) reaction on a thick 6 mg/cm^2 target at 65 MeV (cross sections shown in figure 3.7). The AFRODITE experiment at the time consisted only of 8 Clover detectors, and the experiments ran for a total of 5 days using a $\gamma\gamma$ trigger. In order to suppress the effect of low-energy gamma-rays, the Clover detectors were fitted with absorbers of 0.15 mm tin and 0.07 mm brass. Approximately 1.4×10^9 double-coincident events were recorded. The observed level scheme from the AFRODITE experiment is shown in figure 4.9.

As can be expected with the lower intensity beam (relative to that of [50, 51]), the nuclear excitations are limited to a lower energy and spin, resulting in virtually all populated states (that can be inferred from the $\gamma\gamma$ correlations) within 8 MeV and $25\hbar$ of the ground state. The trigger does allow the study of lower-multiplicity cascades, but due to the 3α-cluster nature of the ^{12}C beam (in addition to (^{12}C,xn) reaction channels, (^{12}C,αxn) and (^{12}C,$2\alpha x$n) are also observed), the data set does contain a fair number of contaminant nuclei. In addition to ^{156}Er, gamma-rays from ^{147}Sm, ^{150}Gd, ^{153}Dy, ^{154}Dy, ^{156}Dy, ^{155}Er, ^{157}Er and ^{158}Er were also detected.

University of Cape Town

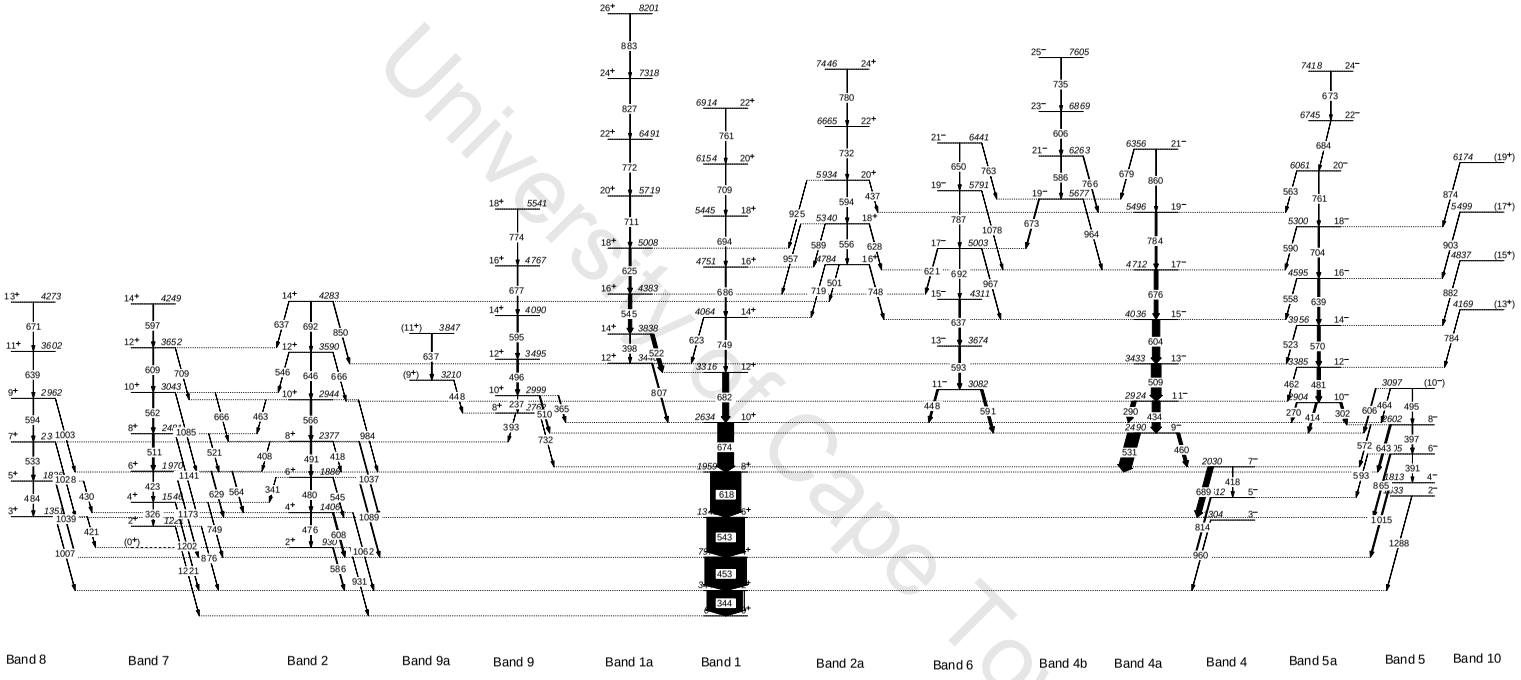

University of Cape Town

Figure 4.9: The level scheme obtained for ^{156}Er from the iThemba LABS experiment. Band construction is based on likeness of character. Note the artificial splitting of bands 4 and 4a, where two bands of differing character crossed, and the unfavoured band continuation is missing. The offset at the top of 5a corresponds to another crossing, labeled 5b in [50].

In order to interpret the bands of figure 4.9, the plots of energy against spin (less a rigid rotor reference frame, to expand the differences) and intrinsic alignment should be considered. When dealing with alignments, it is useful to know the K value of the bands, which is difficult to ascertain. The values K used for the figure 4.11 may be unjustified.

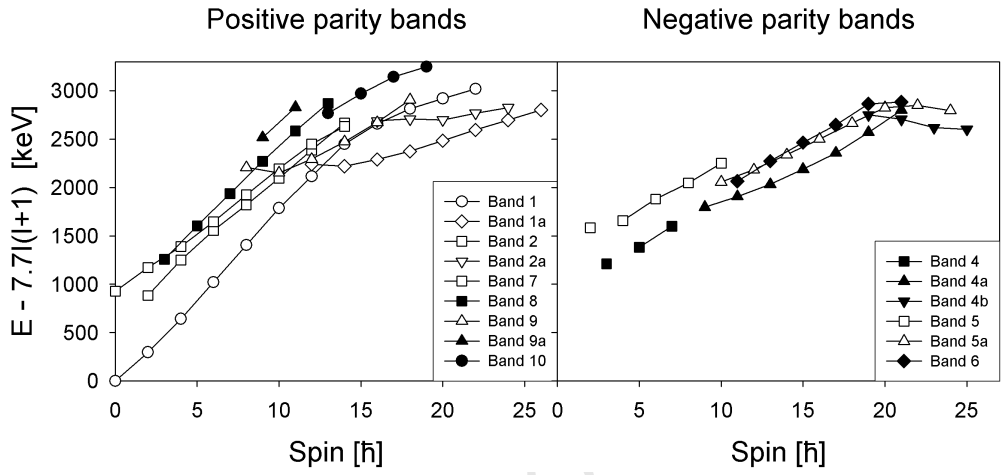

Figure 4.10: Energies, less a rotating rigid rotor reference, of the observed bands in ^{156}Er. Open symbols used for even, filled for odd spin states. The vibrational states are denoted by squares.

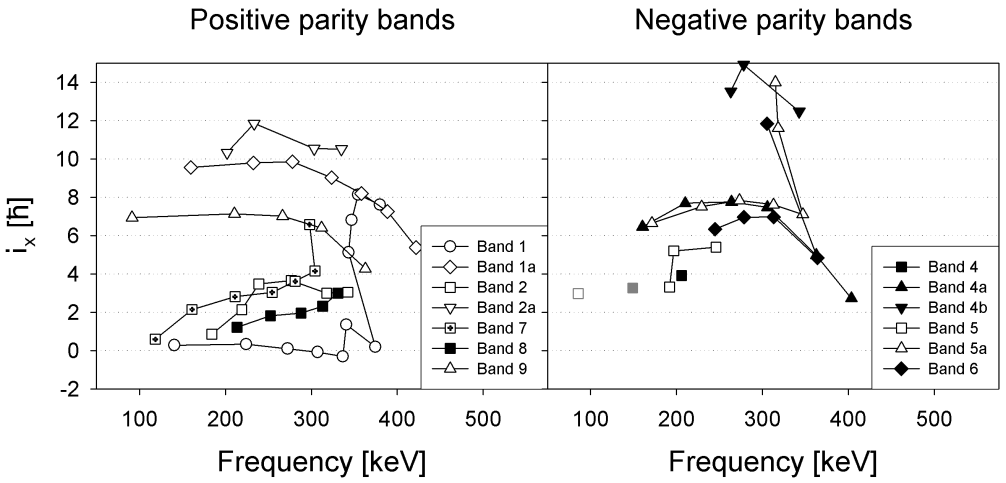

Figure 4.11: Aligned angular momenta of the observed bands in ^{156}Er. Open symbols used for even, filled for odd spin states. The vibrational states are denoted by squares. Grey squares coincide with the unobserved transitions between known levels [59].

4.2.1 Positive parity bands

The position of the observed bands in the level scheme will be described in this section, together with a short interpretation of the underlying structure being represented in the bands, where possible.

Bands 1 and 1a

In the published work (figure 4.3), the ground state band changes character after the 10^+ state, with only a single extra level 12^+, (807 keV transition) continuing the initial ground state configuration. Setting single gates on the $12^+ \rightarrow 10^+$ and $14^+ \rightarrow 12^+$ transitions of [50] (shown in figure 4.12) it was deduced that there are two bands feeding the 3313 keV 12^+ state of [50] (decaying via 682 keV gamma-ray). In the current work, the band containing the 522 keV, 625 keV and 711 keV gamma-rays has been labelled band 1a, whereas the band containing 749 keV, 686 keV and 694 keV gamma-rays is understood as a continuation of the ground state configuration, or band 1.

University of Cape Town

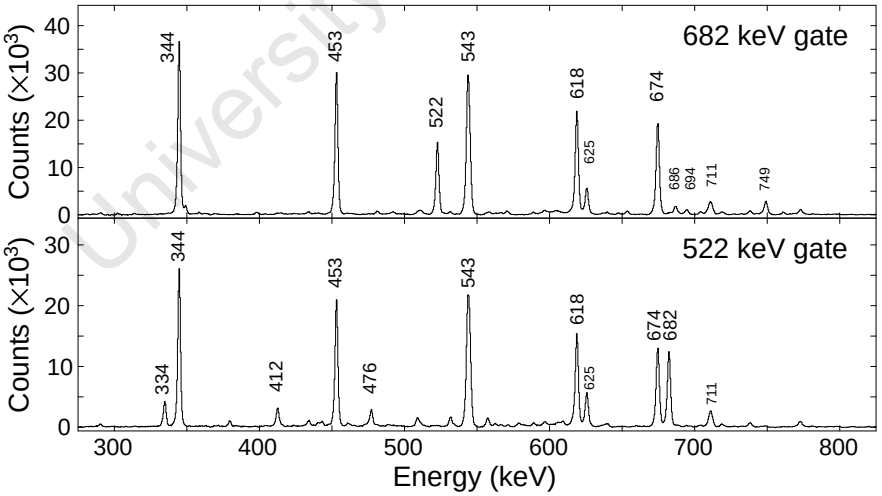

Figure 4.12: Spectra from ^{156}Er gated on the 682 keV and 522 keV transitions. The 334 keV, 412 keV and 476 keV peaks in the 522 keV gate correspond to the ground state band of ^{154}Dy.

As is evidenced by the aligned angular momentum plots (figure 4.11), the positive-parity yrast band 1a has $i_x \approx 10\hbar$, which is consistent with Coriolis induced breaking of a pair of $i_{13/2}$ neutrons, and may be associated with the AB structure in the quasiparticle model.

The spectra from the continuation of band 1 are shown below.

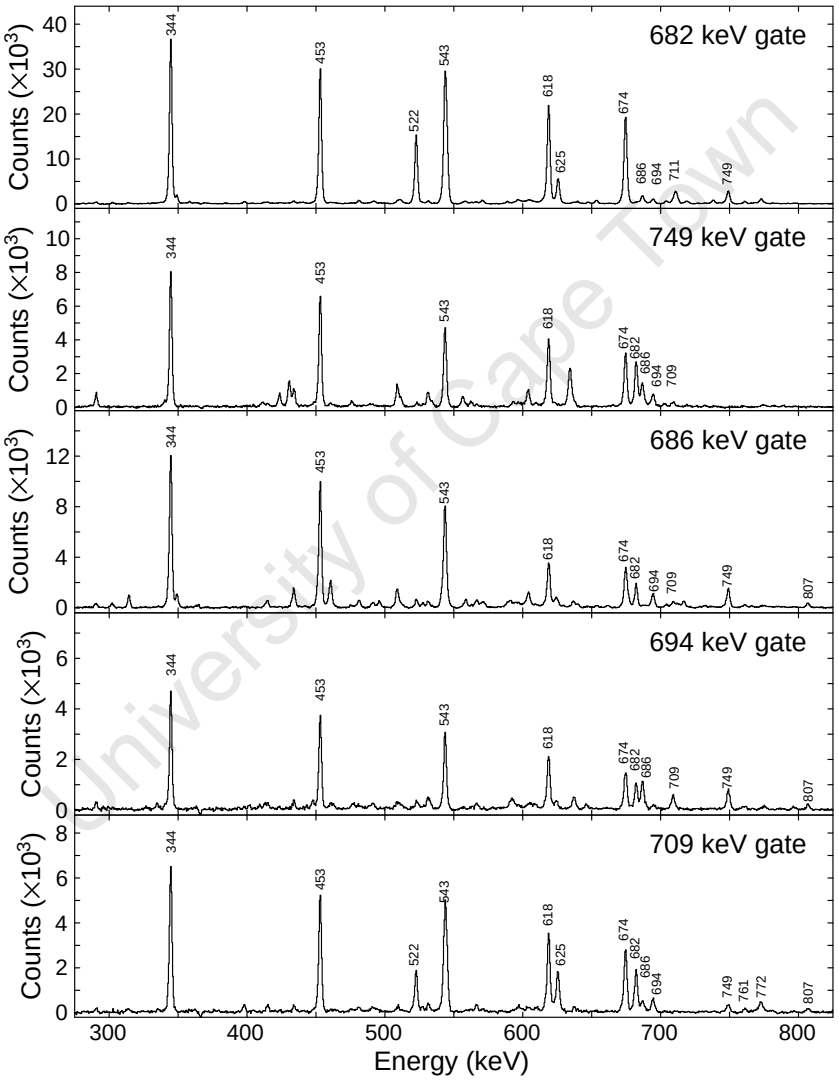

Figure 4.13: Representative spectra showing the continuation of band 1 past spin 12 in ^{156}Er. Note that the 709 keV gate shows some peaks from band 1a which contains a stronger 711 keV transition.

University of Cape Town

Bands 2, 7 and 8

The low-lying positive parity bands (far left in figure 4.9) are three bands whose bandheads are significantly below 2 MeV. These bands correspond to the quadrupole vibrational excitations [3, 4], commonly referred to as β ($K = 0$) and γ ($K = 2$) vibrations. The vibrational character of the structure built upon the first excited 0^+ state has been questioned [60, 61], but is not further addressed in this work.

The data obtained contains no levels that have not already been reported, and the transitions between these bands and the ground band can be confirmed. There are several weak linking transitions joining the two even spin bands, and no evidence was found for the 0^+ state in band 7 of [51].

The lack of observational evidence for the 0^+ (which is claimed to have the same energy as the 2^+ state of band 2) leads to a difficulty is the differentiation between the even-spin states of γ band with the β band. However, in this data set several decays ($5^+ \rightarrow 4^+$ and $3^+ \rightarrow 2^+$) were observed from the odd-spin γ band to band 2, supporting [51] in claiming that bands 2 and 8 are the γ band partners, with band 7 being the β band.

Bands 2a, 9 and 9a

Bands 2a and 9 are both positive parity structures corresponding to two-quasiparticle excitations. Band 2a previously has been observed down to the 12^+ state [51], although in this work it was only seen down to the 16^+ state before decaying to the ground band (1), S-band (1a) or the even-spin γ band (2). The extremely high level of aligned angular momentum ($12\hbar$ – see figure 4.11) of this band is not reproducible from a pure quasiparticle picture. Rather, it has been proposed that it may be a coupling of the AB quasineutron structure with the $2\hbar$ γ-vibration [51].

Band 9 has been observed down to the 8^+ state, and its primary decays are to the negative-parity odd-spin states (bands 4, 4a), as well as a decay to the 7^+ state of the odd-spin γ band. The bandhead appears to be the 8^+

University of Cape Town

state: the only observed transitions out of that state are to two non-yrast bands. Indeed, there are no peaks in the 237 keV gate (figure 4.13) that are not explained by the current level scheme.

Band 9 carries approximately $7\hbar$ alignment (figure 4.11), and it appears to be independent of the band 1-1a crossing, suggesting that its configuration is $i_{13/2}$ independent. It has been proposed [50] that this band corresponds to a rotationally aligned $(h_{9/2}, f_{7/2})^2$ neutron configuration.

Next, it is interesting to consider the 448 keV gate (figure 4.14). There is a strong 448 keV transition linking the ground band to band 6, and the 592 keV and 637 keV peaks correspond to transitions within that band. Additionally, 448 keV is a member of a strong band in ^{153}Dy, which is responsible for the 488 keV, 532 keV, 582 keV and 627 keV peaks. Finally, there are also small peaks at 393 keV and 732 keV, suggesting that there is a decay into the 8^+ state of band 9. Furthermore, the intensity of the 448-637 coincidence is stronger than expected based only on the transitions in band 6. This led to the formation of band 9a in the level scheme.

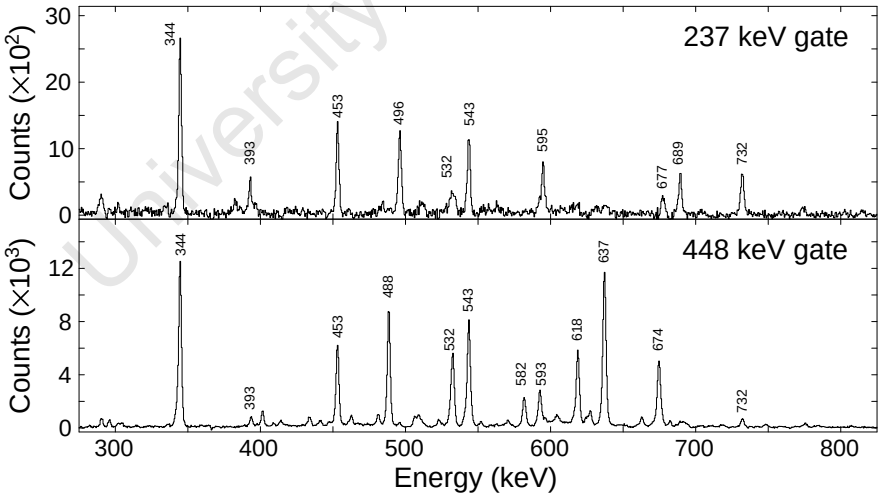

Figure 4.14: Spectra from ^{156}Er gated on the 237 keV and 448 keV transitions, showing that the 448 keV state is feeding the 8^+ state of band 9.

University of Cape Town

Band 10

Finally, there are several weak, high energy transitions which feed into the two-quasiparticle, negative parity band (5a). Figure 4.15 shows the successive disappearance of 784 keV, 882 keV, 903 keV and 874 keV coincidences as one considers successive gates on in-band transitions of band 5a.

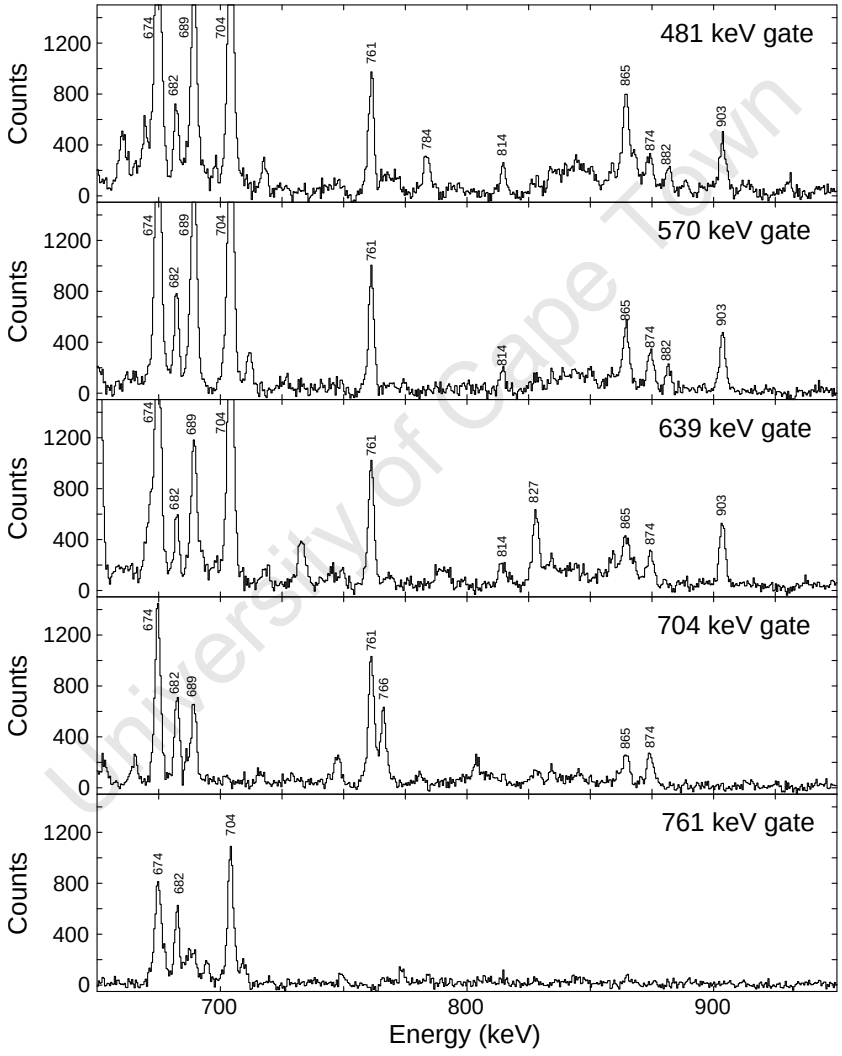

Figure 4.15: Spectra showing the high-energy transitions feeding into band 5a of ^{156}Er. The 689 keV and 814 keV peaks correspond to the decay out of the odd-spin octupole (band 4). The additional peaks (766 keV and 803 keV) in the 704 keV gate correspond to the yrast band in ^{157}Er.

University of Cape Town

The seemingly regular structure to these feeding transitions suggests that the configuration of the source levels is similar. There is, however, no intensity going to expected in-band transitions, suggesting either that these states do not share a configuration, or the out-of-band transitions dominate the would-be in-band E2 rates. With no conclusive result from the DCO analysis (statistics too low), these out-of-band transitions are tentatively labeled E1, which would make band 10 a positive parity structure.

4.2.2 Negative parity bands

The analysis of the level scheme has yielded very little new information on the negative parity states, although the data collected form a neater set of structures than the positive parity bands.

The negative parity states come in two primary bands of odd and even spin, and have been labelled as bands 4 and 5 respectively, with derivatives once the band character changes. At low spin, both have vibrational nature, but from spin 9^- the quasiparticle bands dominate.

Bands 4a, 5a and 6

As demonstrated in figure 4.11, these three bands all have approximately $7\hbar$ angular momentum, and that remains reasonably constant. The alignment plots for bands 5a and 6 do show a drastic upturn, but that is from the inclusion of two (one) states from the 5b (6a) band [51], and are not true band contours. This constant alignment has been interpreted as consistent with a two-quasineutron configuration obtained through coupling a single $i_{13/2}$ neutron with another in an $h_{9/2}$ or $f_{7/2}$ state. The extensions of these bands (4b, 5b, 6a) have been reported to contain irregular behaviour, which may be interpreted as arising from weak oblate-triaxial deformation [51], although that has not been observed in this data set.

University of Cape Town

Bands 4 and 5

The lowest observed negative parity states fall withing the pairing gap, and are therefore expected to be vibrational in nature. Weak transitions have been observed between these states down to spins 5^- and 4^-, although β-decay studies have revealed the existence of lower-lying 3^- and 2^- states [59], which are believed to be part of these bands. Additionally, the comparative strength of the quasiparticle bands 4a and 5a has resulted in no known extensions to the vibrational states past the 8^- state.

In this work, a weak transition at 495 keV was observed in coincidence with the transitions out of the 8^- state, as is shown below. The peak is also visible on the $6^- \rightarrow 4^-$ gate, but at higher intensity than expected. This slight inconsistency leads to the placement of the 10^- level in band 5 as only a tentative assignment. The energy/alignment plots (figures 4.10, 4.11) support this state as consistent with the vibrational nature of band 5.

University of Cape Town

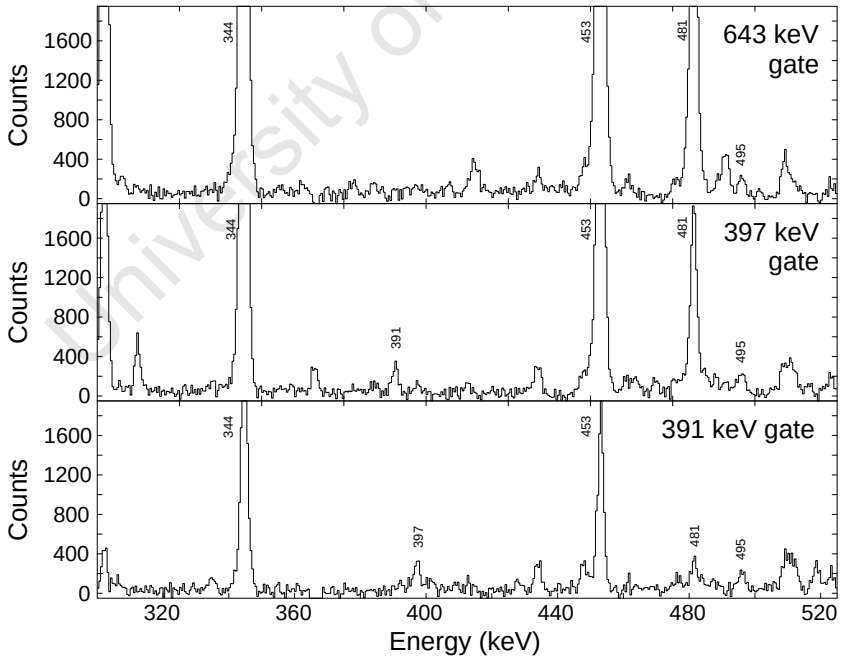

Figure 4.16: Spectra obtained from setting gates on transitions out of the 8^- and 6^- states in band 5 of ^{156}Er.

Unfortunately, no significant evidence could be found in the data set for either the 9^- continuation of the odd-spin octupole vibration (band 4), or the 7^- state in two-quasiparticle band 4a.

4.3 $^{160}_{68}$Er

The experiments to study the $N = 92$ isotopes of erbium and dysprosium was submitted in early 2009, and the data were collected in the May of 2010. Due to the unavailability of a ^{158}Dy target (it is a rare stable isotope, and the production of such a target was deemed financially unfeasible), states of ^{160}Er were populated using a ^{152}Sm(^{12}C,4n) reaction at a beam energy of 64 MeV, which does allow higher angular momentum transfer, but, again, allows beam fragmentation to contaminate some of the data. The target used had a thickness of 5 mg/cm^2, which is sufficiently thick to stop the recoils within the target, so no Doppler correction was necessary.

For this experiment, 9 Clover detectors were available, and 4 LEPS detectors were also included, to increase the detector efficiency at low energy. The LEPS detectors had, however, been pulled back to reduce neutron damage, decreasing their solid angle coverage drastically, and they played little contribution in the experiment. The experiment ran for two weekends (5 days total) with a pulsed beam (340 ns), and 2.7×10^9 time-correlated $\gamma\gamma$ coincidence events were collected. The level scheme constructed out of the collected data is shown in figure 4.17.

There is a known level [49] in ^{160}Er at 1395 keV which might correspond to a 3^- vibrational state. While unobserved, it has been included in the level scheme, as a possible continuation of band 5. Its possible existence has additionally been included (in grey) in the E vs I and the aligned angular momenta plots (figures 4.18, 4.19).

University of Cape Town

Figure 4.17: The level scheme obtained for ^{160}Er from the iThemba LABS experiment.

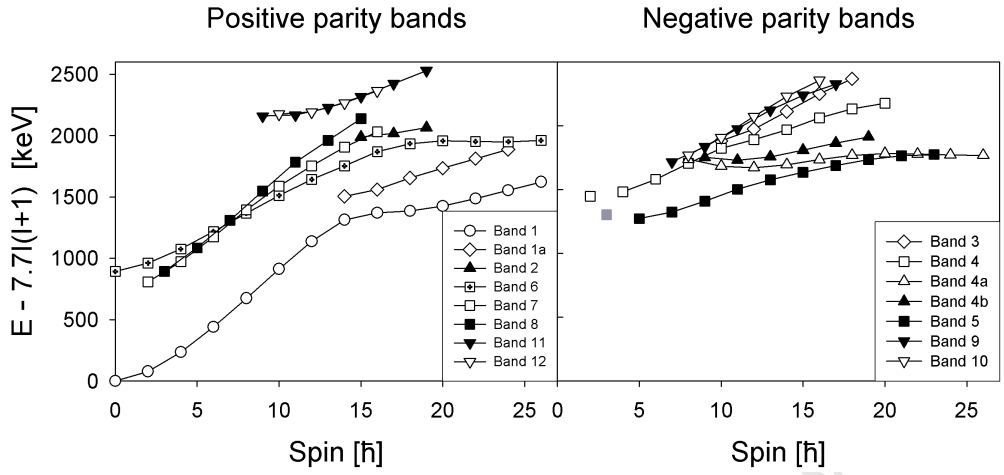

Figure 4.18: Energies, less a rotating rigid rotor reference, of the observed bands in ^{160}Er. Open symbols used for even, filled for odd spin states. The vibrational states are denoted by squares.

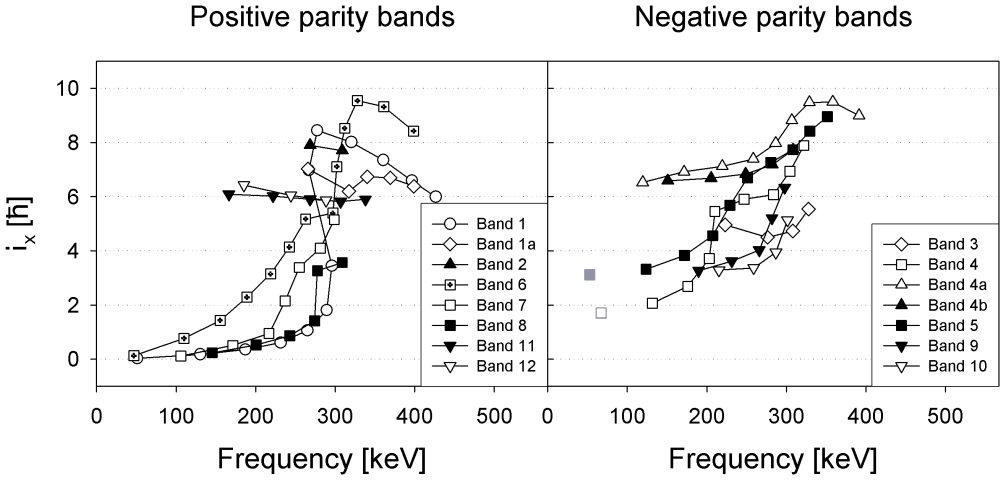

Figure 4.19: Aligned angular momenta of the observed bands in ^{160}Er. Open symbols used for even, filled for odd spin states. The vibrational states are denoted by squares. Grey squares coincide with the unobserved transitions between expected band levels.

Since this experiment used a ^{12}C beam at 64 MeV, the nuclear excitations are again limited to within 8 MeV of the ground state. However, most of the low-lying bands reported in [56] have been observed. The triaxial superdeformed bands are naturally not populated, and in addition no evidence of bands 7 and 8 of [56] has been observed. Three new low-lying band structures have been added to the level scheme, labelled as bands 2, 3 and 4b.

4.3.1 Positive parity bands

Bands 1 and 1a

The yrast band in ^{160}Er, termed band 1, is well understood: it demonstrates a backbend at $\hbar\omega \sim 280$ keV which corresponds to the $(i_{13/2})^2$ alignment (AB crossing) [54]. The non-yrast band 1a (band 3 in [56]) can be treated as a continuation of the ground state configuration past the crossing with the S-band. The increase in angular momentum has been previously discussed as a four-quasineutron configuration [54].

Band 2

A rather weak set of transitions has been observed, resulting in this band being proposed to exist. Gates on 906 keV and 474 keV transitions share a set of small peaks at 537 keV and 618 keV (figure 4.20). The gates are proposed to be the out-of-band transitions into the 14^+ yrast band and 13^+ state in the odd-spin γ band respectively. Since transitions to the 12^+ yrast state were not observed, the proposed bandhead (at 3837 keV) could be 14^- or 15^+. A DCO analysis was performed and, while inconclusive, it did suggest that the out-of-band transitions might include a quadrupole contribution: a tentative assignment of 15^+ would give the out-of-band transitions a plausible E2/M1 character.

University of Cape Town

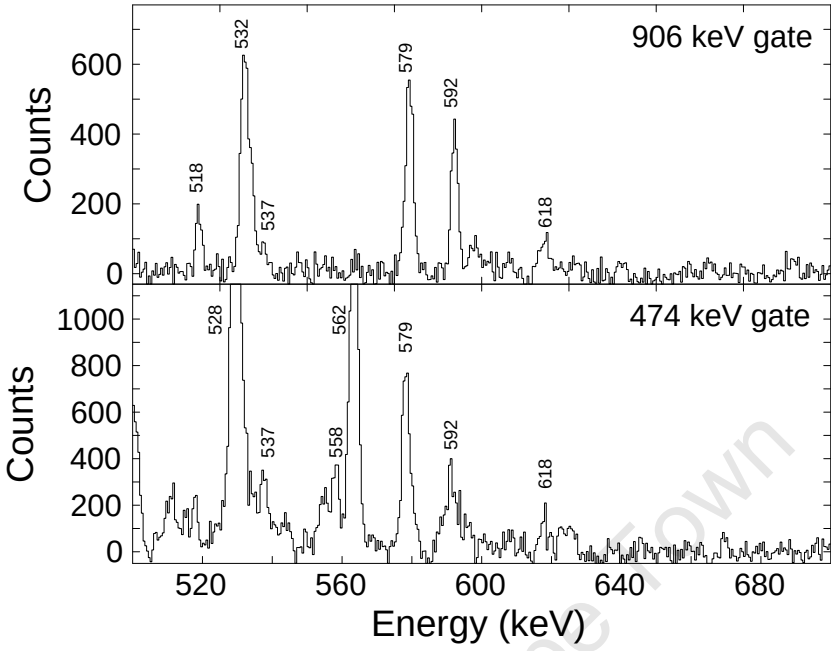

Figure 4.20: Gates on the out-of-band transitions for band 2 of ^{160}Er.

University of Cape Town

Bands 6, 7 and 8

The three bands whose bandheads are around 1 MeV are indicative of the familiar structure of β- and γ-vibrational bands. The low-spin states are in agreement with [55], although the alignment of these bands (see figure 4.19) does not have the approximately constant behaviour expected of these single-phonon vibrational states.

The 0^+ state, established as part of band 6, is indicative of the β-vibration [3], but the alignment of this band increases sharply, exceeding the alignment of the yrast band, even past the AB crossing. The band is extended past spin 14^+, and indeed it matches up reasonably smoothly at spin 16^+ with band 4 of [56]. The spectra indicative of this connection are shown in figure 4.21.

Bands 7 and 8 agree with the results of [55] at low spin, although the data collected deviate from the proposed band structures. The even-spin in-band transition sequences of 274 keV, 371 keV, 451 keV and 518 keV, 569 keV

are observed, but also in coincidence with a 486 keV transition (figure 4.22), which modifies the band from spin 10^+ upwards. This placement is reinforced by the observation of the 1208 keV transition to the 8^+ state in the ground band, whereas there is no peak corresponding to a 1240 keV transition when gating on the $8^+ \rightarrow 6^+$ ground state (464 keV) transition. The odd spin band is extended by a 624 keV transition, disagreeing with the band continuation observed in band 5 in [56].

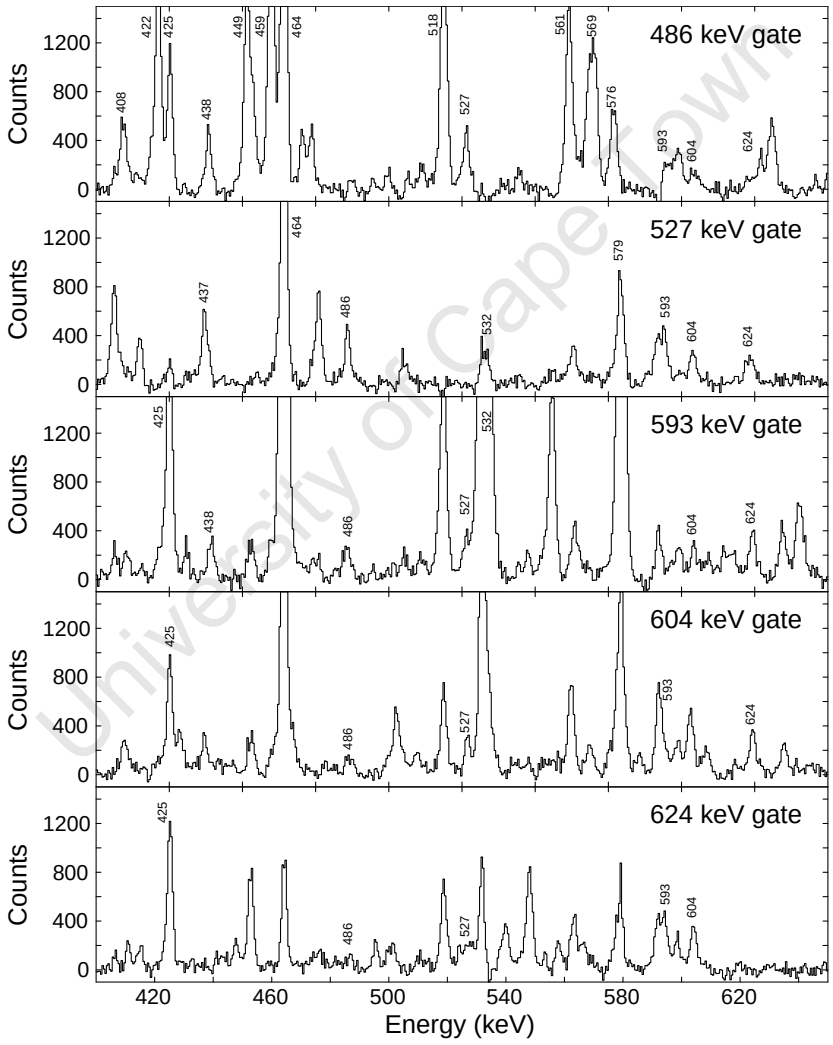

Figure 4.21: Gates on consecutive in-band transitions in band 6 of ^{160}Er, joining the known β band to the band structure observed in [56].

University of Cape Town

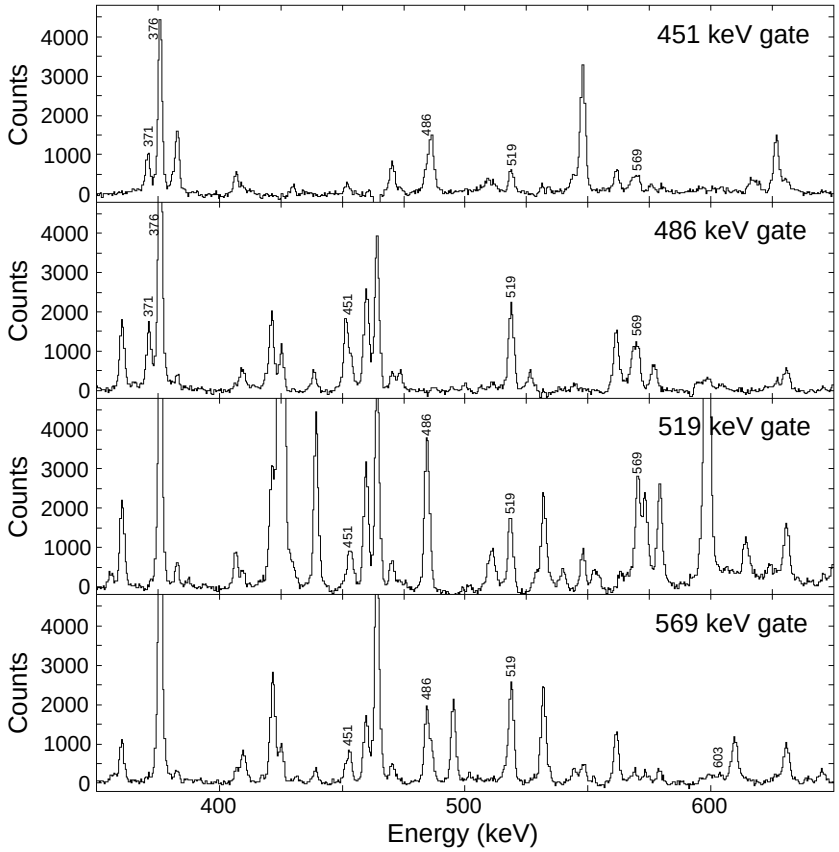

Figure 4.22: Gates on consecutive in-band transitions in band 7 of ^{160}Er.

Bands 11 and 12

A strongly coupled band had been reported (bands 11 and 12 in [56]) to be weakly connected to the strongly coupled bands 9 and 10, although their character could not be properly determined. In this work these bands are observed, and the 488 keV and 577 keV transitions can be confirmed to exist. However, the population of these states was very low, and additional information regarding the spin or structure of this band cannot be determined – rather it is left tentatively as a positive parity structure.

4.3.2 Negative parity bands

Among the observed negative parity structures, a total of seven bands have been inferred from the collected data set. Five of these have been previously observed [56], and two of these have been extended down in spin.

Bands 4 and 5

The odd- and even-spin vibrational (octupole) bands had previously been seen down to spins 6^- and 9^- respectively. In this work two further transitions were seen below this, and there is some evidence for a third, taking the observed in-band transitions down to spins 4^- and 5^- respectively. Due to the low branching ratios, the only way of finding these weak transitions is through the setting of gates on the high-energy E1 transitions to the ground band, shown in figure 4.23.

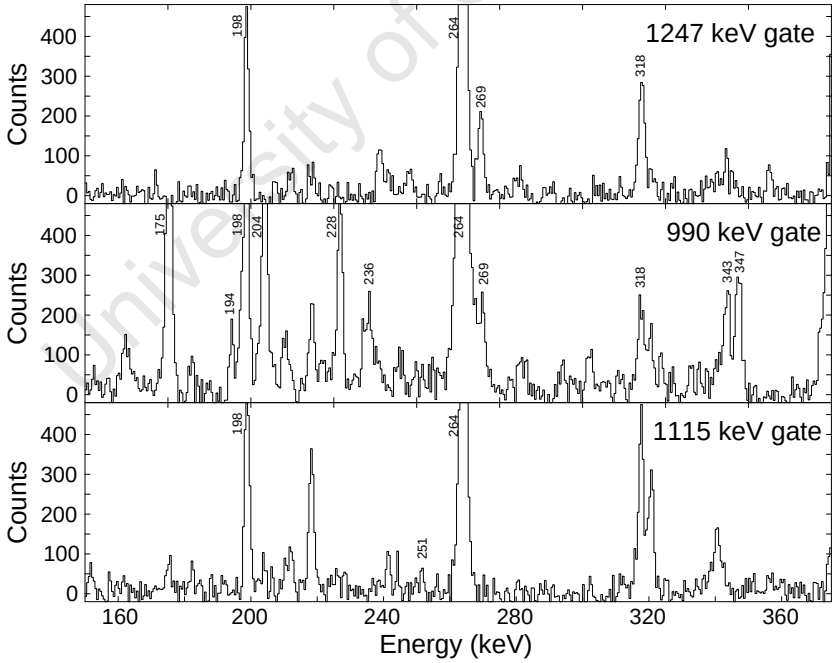

Figure 4.23: Gates on E1 transitions from the 6^-, 9^- and 7^- octupole states in ^{160}Er respectively, showing the weak in-band E2 transitions. The sharp peaks at 198 keV and 318 keV are from the contaminant ^{161}Er.

University of Cape Town

At high spin, band 5 takes on a distinctly quasiparticle-like character, and is understood as and odd-spin two quasineutron band [54].

Band 3

As is seen in figure 4.19, the even spin octupole band (band 4) gets an increase in alignment at $\hbar\omega \sim 210$ keV, which is generally indicative of a band-crossing or interaction. If the low-spin octupole band mixes with a two-quasiparticle band, the conjugate band ought to also be present in the vicinity.

Considering high-energy transitions that feed into the the ground band, a new structure was found (figure 4.24), with a very similar 10^- energy to that of band 4. Based on the energies and alignments, this could be the continuation of the vibrational band past the crossing, although no transitions could be found linking these states to the low-spin states in band 4.

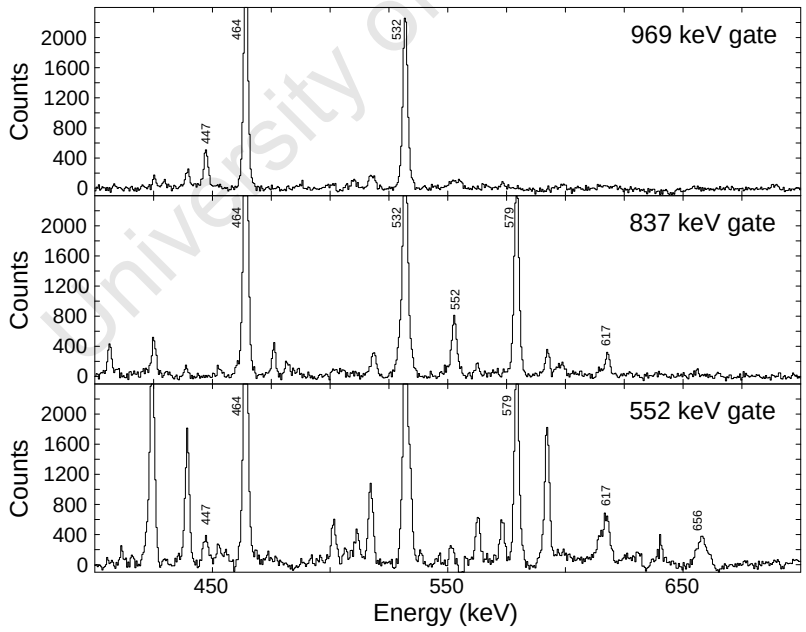

Figure 4.24: Representative spectra substantiating the placement of band 3 in the level scheme of ^{160}Er. The extra peaks in the 552 keV gate correspond to coincidences with the transitions from band 4a.

University of Cape Town

Bands 4a and 4b

In a parallel to ^{156}Er, there appears to be an even-spin two-quasiparticle band of lower energies than the octupole band past spin 8^-. This band, labeled 4a (band 1 in [56]) asymptotically approaches band 5, and is well understood as an even-spin partner to the two-quasineutron band 5.

In addition, a band which behaves as an odd-spin partner to 4a has been found (shown in figure 4.25). There are no transitions linking it to either the octupole bands, or the even-spin states in 4a; yet, considering its alignment (figure 4.19), it is almost certainly also a two-quasineutron band.

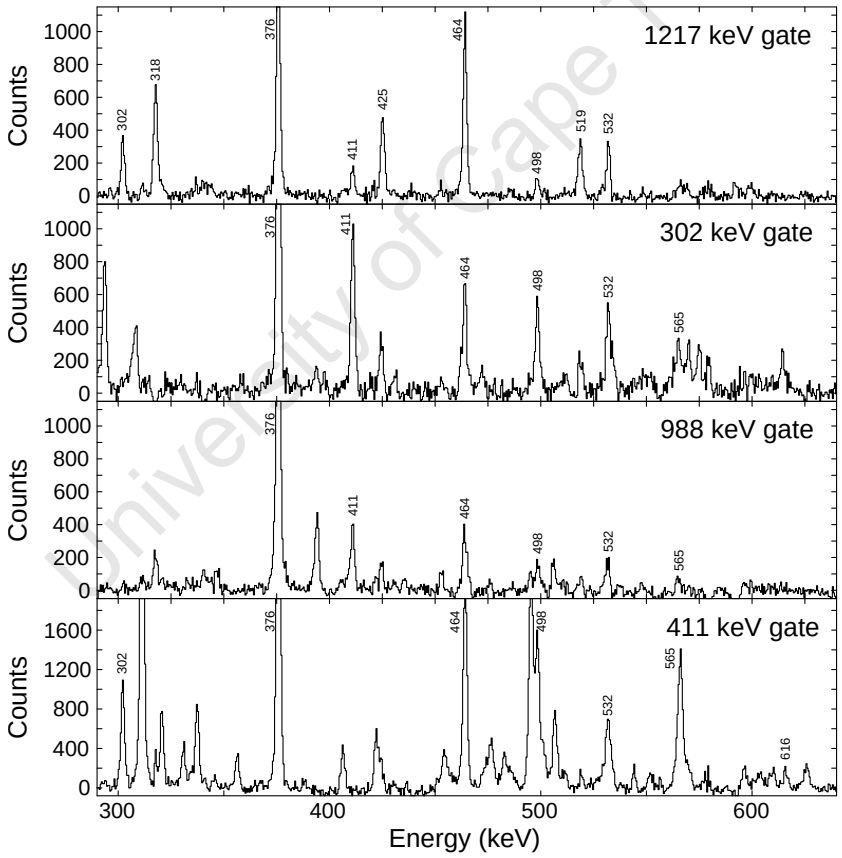

Figure 4.25: Representative spectra substantiating the placement of band 4b in the level scheme of ^{160}Er.

University of Cape Town

Bands 9 and 10

This strongly coupled set of bands has been reported in [56], and has been interpreted as a two-quasiproton configuration. In this work the states were populated, and no evidence was found of the bands continuing to lower spin, suggesting that the $7^-/8^-$ states are bandhead states.

4.4 $^{158}_{66}$Dy

The last experiment was delayed due to problems with target manufacturing, and upon rescheduling by the iThemba project advisory committee, the running time was reduced to single weekend (56 hours) in December 2010. The experiment used the ^{156}Gd(α,2n) reaction at 27 MeV, with a thicker than expected (11 mg/cm^2) target and nine Clover detectors. The limited experimental time dictated that the detector dead-time needed to minimized, therefore the experiment was run without a pulsed beam, from which 1.05×10^9 $\gamma\gamma$ coincident events were unpacked from the collected data.

The use of an α beam resulted in a very clean reaction (the main contaminants came about through isotopic impurities in the target), at the cost of reduced excitation energy: all populated states in ^{158}Dy were within 4.3 MeV of the ground state, and no states above spin 18 were inferred. The deduced band structure is presented in figure 4.26, the energy-spin plots for the positive/negative parity bands in figure 4.27, and the alignments in figure 4.28

Due to the very clean reaction mechanism, most of the observed gamma-rays can be attributed to the nucleus of interest. Aided by the relatively low excitation energy of the rotational ground state band (2^+ state at 99 keV), most of the decays out of vibrational/quasiparticle bands had high energy ($\sim$ 1) MeV out-of-band transitions. By considering consecutive gates in the ground band, the feeding point of most high-energy transitions could be inferred directly, as shown in figure 4.29.

University of Cape Town

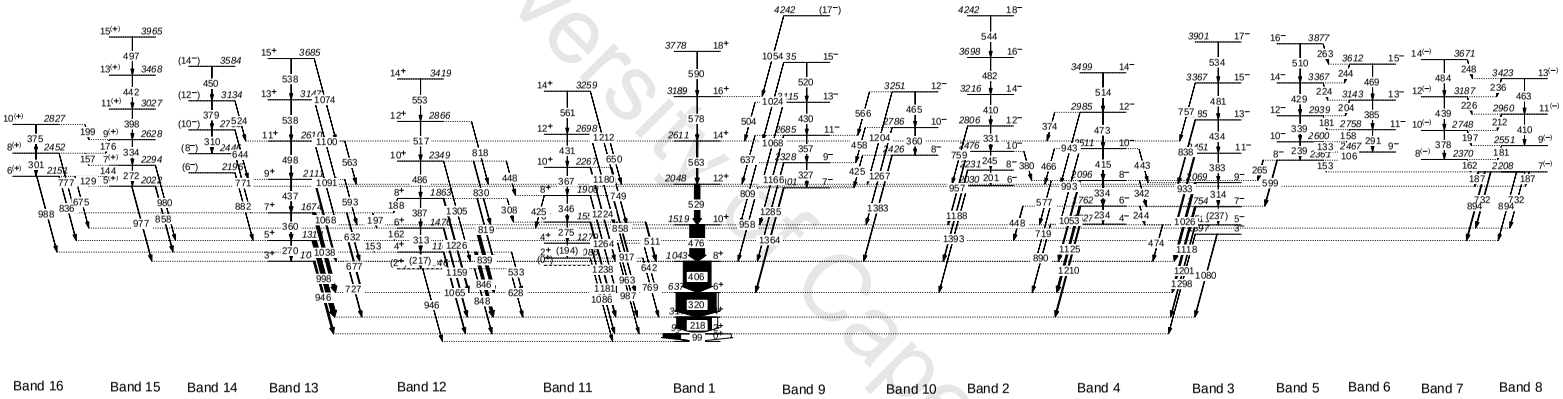

University of Cape Town

Figure 4.26: The level scheme obtained for ^{158}Dy from the iThemba LABS experiment. Bands 7, 8, 9, 10, 14, 15 and 16 have not been previously observed.

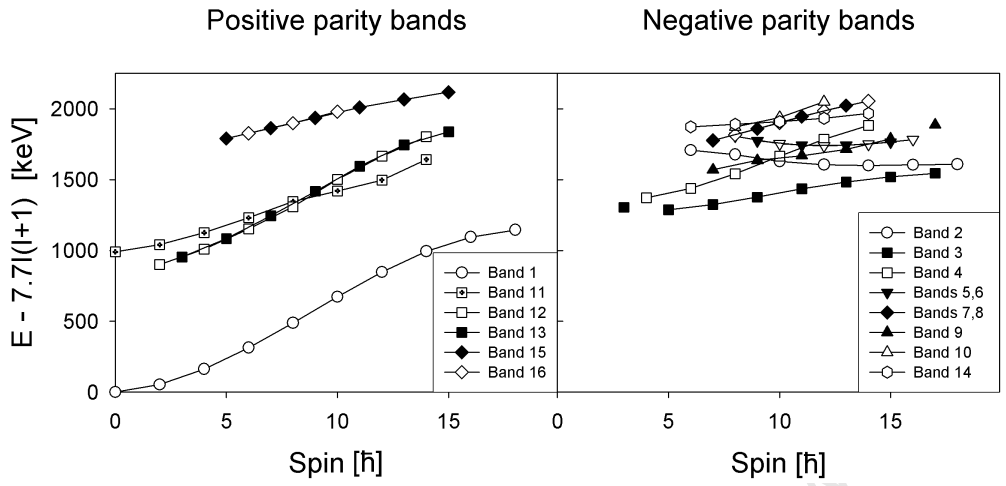

Figure 4.27: Energies, less a rotating rigid rotor reference, of the observed bands in ^{158}Dy. Open symbols used for even, filled for odd spin states. The vibrational states are denoted by squares.

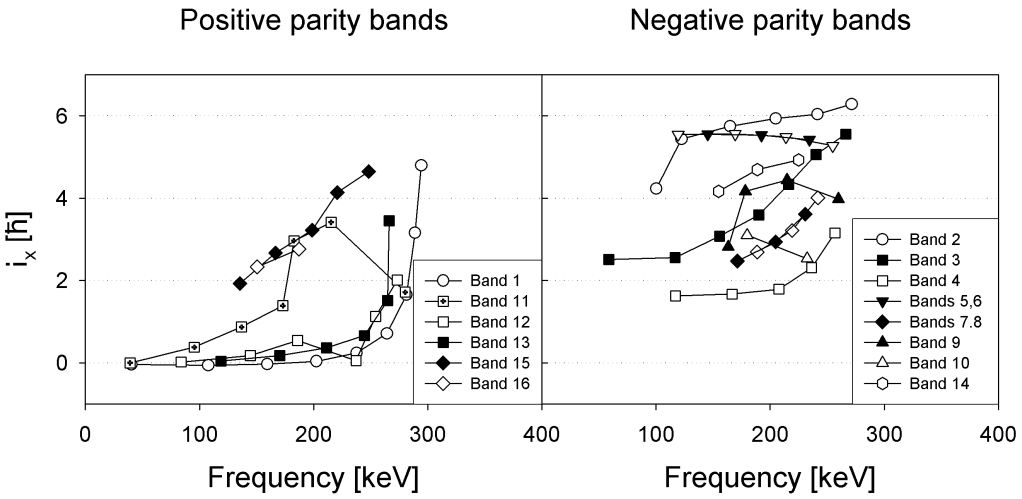

Figure 4.28: Aligned angular momenta of the observed bands in ^{158}Dy. Open symbols used for even, filled for odd spin states. The vibrational states are denoted by squares.

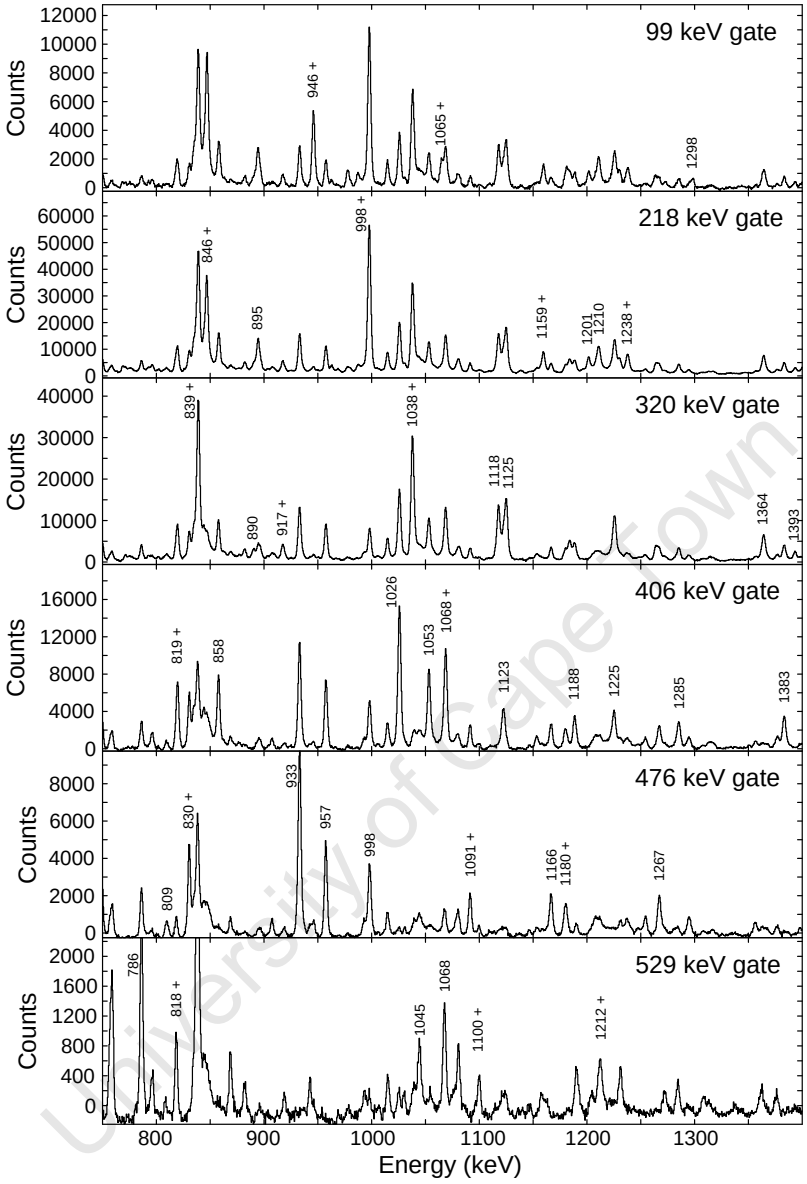

Figure 4.29: Spectra from ^{158}Dy gated on the ground state transitions, showing the observed high-energy transitions. The peaks are labelled only on the spectra which correspond to the highest yrast in-band gates at which coincidence is observed. These correspond to the level at which the yrast band is fed, from spin 2^+ on the 99 keV gate, down to the 12^+ state for the 529 keV gate. Peaks labeled with a + correspond to gamma-rays directly linking the positive parity vibrational states to the ground band.

University of Cape Town

4.4.1 Positive parity bands

Band 1

The yrast band in ^{158}Dy has been established [58] as undergoing the AB crossing (S-band), with deviation from the ground state configuration starting at the 14^+ state. In this experiment the states were only populated high enough to observe the band interactions, but not sufficiently as to observe the continuation of the ground state configuration.

Bands 11, 12 and 13

The familiar pattern of three positive parity (vibrational) bands with bandheads within 1 MeV from the ground state is again continued in this nucleus. The very low-spin structures were taken from the accepted levels [20], although the data disagree with the previously accepted results for the β and γ bands: the levels for both even-spin bands have been changed from the 6^+ states upwards. This is corroborated by the observation of the in-band transitions between the new levels. Each of the three vibrational bands has been extended up in spin from the previously deduced level schemes.

Bands 15 and 16

When gating on high-energy transitions out of the gamma bands (12 and 13), several other high-energy transitions are found to be in coincidence. These high-energy gamma-rays have associated low-energy transitions, characteristic of new band structures. Some of these have been tentatively marked as positive parity bands, based on DCO measurements between the out-of-band transition pairs. The bands labeled 15 and 16 appear to form a strongly interacting pair – if these bands are indeed of positive parity, this could be a set of two-phonon γ-band excitations.

University of Cape Town

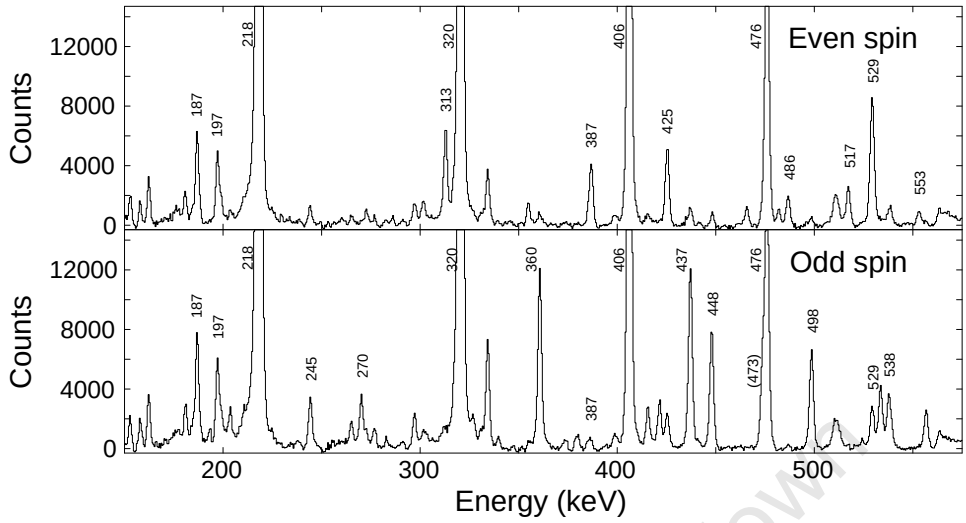

Figure 4.30: Spectra showing the transitions associated with the even and odd gamma bands in ^{158}Dy. The spectra were created by considering the sum of all the out-of-band transitions for the particular bands. Note the large number of 'contaminant' peaks, which correspond to various bands de-exciting down to the gamma bands.

University of Cape Town

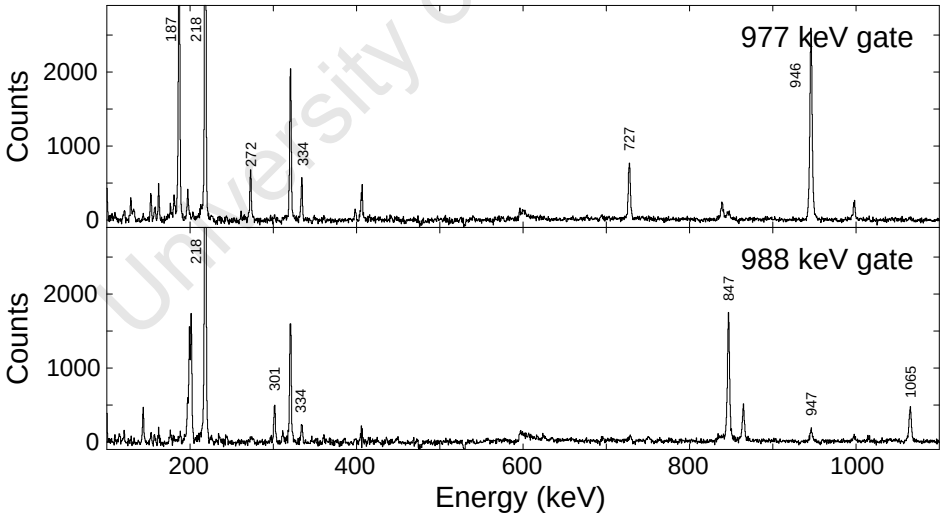

Figure 4.31: Spectra showing the decay out of the bandheads of bands 15 and 16. The 977 keV and 988 keV transitions show clear coincidences with the decays out of the gamma bands.

4.4.2 Negative parity bands

On the negative parity side, bands 2 to 6 have been reported before [57], and have had their spins and parities confirmed [58].

Bands 2, 3, 4

Considering the aligned angular momenta (figure 4.28), at high rotational frequency bands 2 and 3 have $\sim 6\hbar$ alignment, and from high-spin studies [58] this quantity increases with ω. Above a frequency of ~ 300 keV bands 2 and 3 are well understood as two-quasiparticle bands, corresponding to the AF and AE structures, respectively [57]. This experiment has yielded evidence to extend band 3 down from 11^- to 5^- (figure 4.33), wherein the alignment ($2\hbar < i_x < 3\hbar$) suggests that the band takes on a vibrational character. Additional transitions are also observed at low spin for bands 2 and 4 (figure 4.32 below).

University of Cape Town

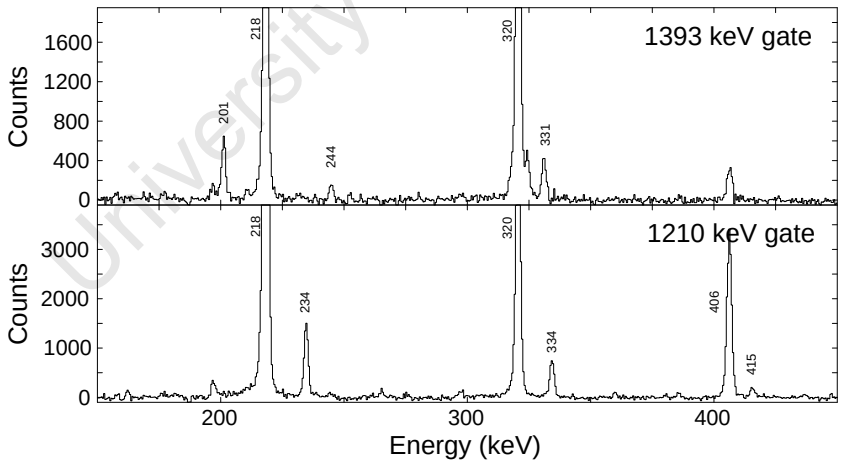

Figure 4.32: Spectra showing the extensions of bands 2 (top) and 4 of ^{158}Dy, gated on the transitions out of the newly placed states. In band 2, the new 201 keV is clearly visible, as are the known 244 keV and 331 keV peaks. In band 4, the new 244 keV transition is observed, as are the higher in-band 334 keV and 415 keV transitions.

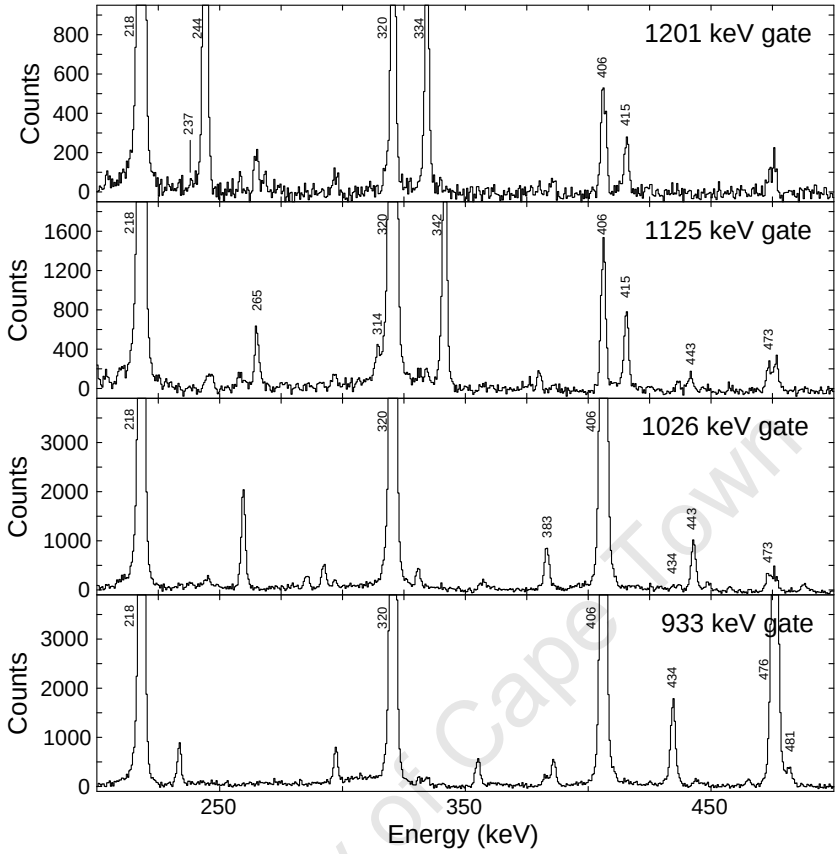

Figure 4.33: Spectra showing the proposed low-spin structure of band 3 in ^{158}Dy. The gates are on the out-of-band transitions from the 5^-, 7^-, 9^- and (known) 11^- states. The 237 keV gamma is tentative, but the 314 keV, 383 keV and 434 keV transitions are clearly identified. The extra observed peaks are in-band and linking transitions to band 4.

University of Cape Town

Bands 5, 6, 7 and 8

The strongly coupled pair of bands 5 and 6 bas been observed previously, and has been interpreted as a coupling between the $i_{13/2}[642]5/2$ and the upwards sloping $h_{11/2}[505]11/2$ neutron orbitals [57]. The decay out of this band pair goes via the even octupole band, which in turn decays to the ground band (and the odd gamma band). The M1 transitions, characteristic of the strongly coupled band, are also reported in coincidence with a 153 keV transition, to a hanging state at $\sim$ 2208 keV.

Decays out of this state have been observed to the 6^+ and 5^+ states in the gamma vibrational band (bands 12,13 in level scheme) through 732 keV and 894 keV transitions (and a 187 keV transition to band 15) although the gamma ray intensities are higher for the gamma-band coincidences than for those in bands 5, 6. Together with the non-observation of these transitions in the previous work, it is inferred that the 2208 keV state is a long-lived isomer. As the data were collected without pulse-selection, no definitive lifetime measurement could be inferred directly from the time spectra.

However, the intensity of the 732 keV transition when fitted to bands 5 and 6 is approximately 40% of the intensity when fitted to the gamma-rays in the γ bands. Given that the experiment was run with a $\Delta t = 150$ ns coincidence window, the lifetime of the state can be estimated:

$$e^{\frac{\Delta t}{\tau_{2208}}} \approx 1 - 0.4, \qquad \Rightarrow \qquad \tau_{2208} \approx -\frac{\Delta t}{\ln(1-0.4)} \approx 300 \text{ ns}. \tag{4.1}$$

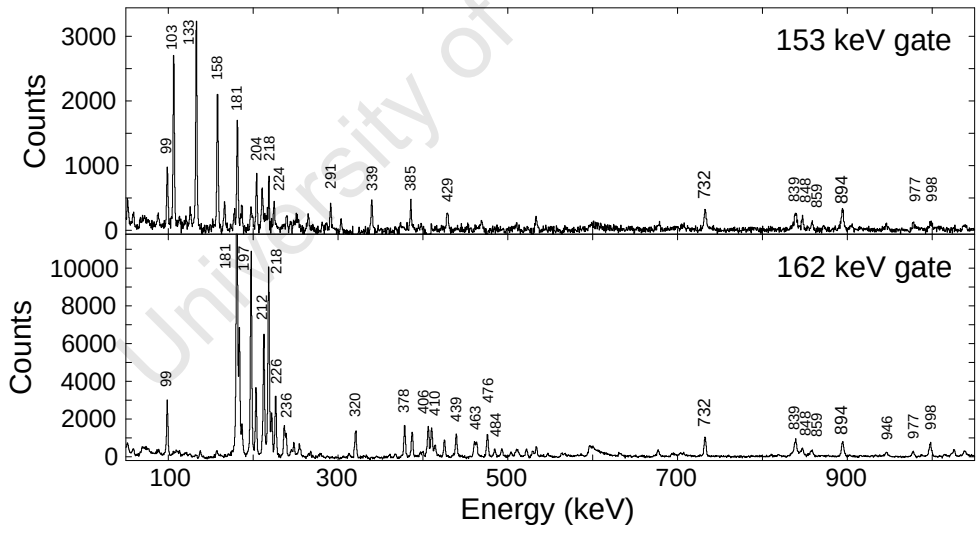

Figure 4.34: Spectra showing the connection of the strongly coupled bands to the isomeric 2208 keV state in ^{158}Dy. The 153 keV gate shows bands 5 and 6, while the 162 keV gate shows bands 7 and 8.

Additionally, gates on the transitions out of the isomeric state have revealed a second set of strongly coupled bands. The gates on the linking transition

University of Cape Town

are shown in figure 4.34. The new bands (7 and 8) do, however, have a fairly low alignment ($2\hbar < i_x < 4\hbar$) which is increasing with ω, suggesting that they are not a quasiparticle configuration.

Bands 9 and 10

Based on the high energy transitions identified as feeding particular states in the ground band, it has been possible to link some of the non-yrast states with (weak) in-band transitions. In addition, for several states in band 9, transitions have been observed to consecutive ($\Delta I = 2$) states in the yrast band. A DCO analysis suggests that the out-of-band transitions are dipole ($I = 1$) in character, forcing the spins to be odd. The decay to consecutive states in the yrast band is not observed for the transitions from band 10, and it has been assigned even spin. Weak connections between the two bands have also been observed. The band alignments of these bands appear to decrease with ω, however, which is inconsistent with both a quasiparticle and a vibrational character.

University of Cape Town

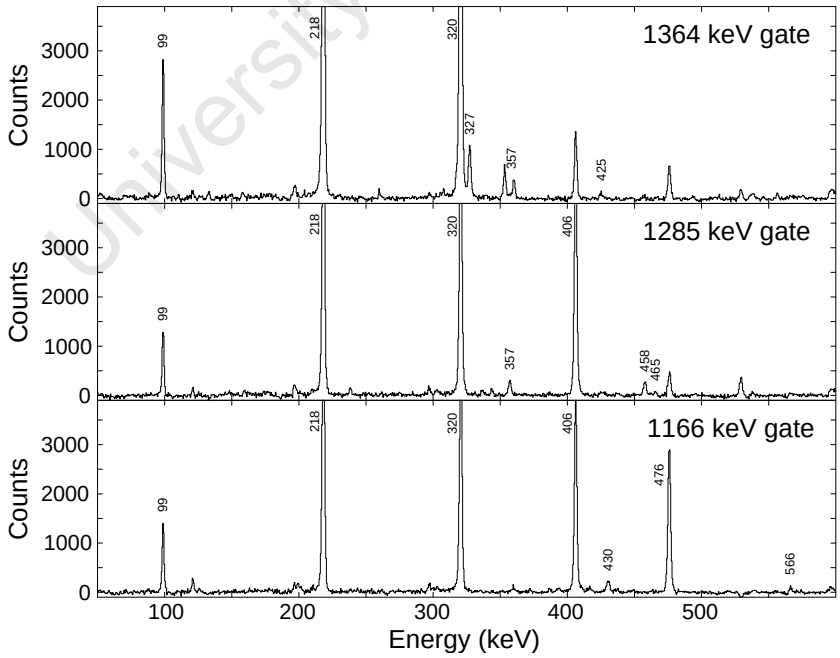

Figure 4.35: Spectra showing transitions associated with band 9 of ^{158}Dy.

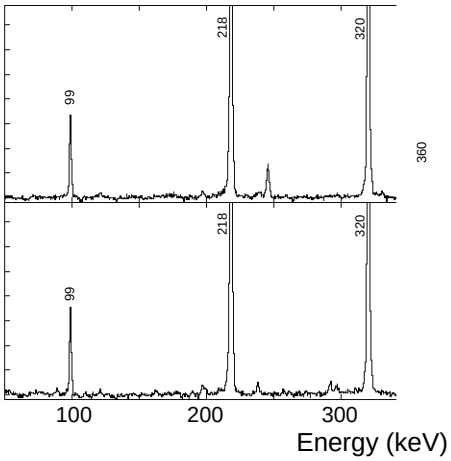

Figure 4.36: Spectra showing transitions associated with band 10 of ^{158}Dy.

Band 14

Finally, a set of reasonably high-energy transitions has been found to connect to the 5^+, 7^+, 9^+ transitions of the odd-spin gamma band, although the in-band transitions for this structure remain extremely weak.

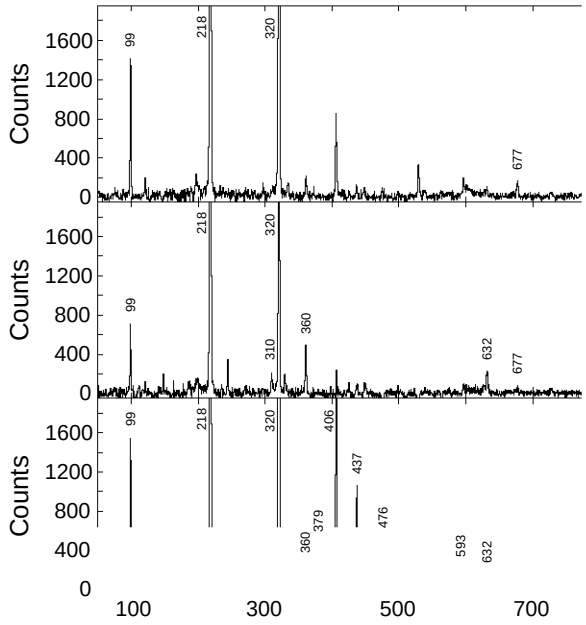

Figure 4.37: Spectra showing transitions associated with band 14 of ^{158}Dy.

Chapter 5

Discussion and Analysis

University of Cape Town

The experimentally inferred bands for ^{156}Er, ^{158}Dy and ^{160}Er have been detailed in the previous chapter, and the discussion must now be centered about the underlying nuclear structure responsible for the formation of those bands. The bands are primarily rotational, with three main subclasses: Bands with a different nuclear deformation, bands with a different quasiparticle configuration, or bands with vibrational phonons.

As was discussed in chapter 2, a quasiparticle configuration in even-even nuclei will require the breaking of a nucleonic pair, and so a static ($\omega = 0$) excitation of twice the pairing gap (about 2 MeV). The favourable configurations for observation are those that have high aligned angular momentum, and therefore whose excitation energy comes down steeply with ω. This is experimentally realized by the majority of the inferred quasiparticle bands carrying an alignment of $7\hbar$ to $10\hbar$.

The vibrational bands on the other hand will carry only the aligned angular momentum associated with the vibration. For octupole vibrations, the $K = 0$ band should carry $3\hbar$, while the $K = 1$ bands should carry $2\hbar$ of alignment.

The experimental alignment data (using equation (2.20)) have been displayed in figures 4.11, 4.19 and 4.28. The negative parity bands that extend to states below the 2 MeV pairing gap have also been shown to have an alignment that

is significantly below that of the low-lying quasiparticle bands, supporting their interpretation as vibrational excitations.

However, in order for such an interpretation to be appropriate, relative strengths of the excitations also need to be reproducible within the physical framework, and this subject is yet to be addressed. While not as apparent in ^{156}Er, where only a single ($7^- \rightarrow 5^-$) odd-spin transition has ever been observed, in ^{160}Er and ^{158}Dy the observed intensity of the in-band transition is noticeably stronger in the even-spin bands. This suppression of the in-band gammas in the odd-spin octupole bands was the original motivation for the tetrahedral proposal, wherein the suppression is due to a reduction to zero of the band's quadrupole moment, and by extension, the B(E2). While the explicit measurement of the B(E2) values for these octupole bands could not be performed, we can extract information about the physics of the band through the evaluation of various branching ratios, determining values for $B(\mathrm{E2})/B(\mathrm{E1})$.

University of Cape Town

5.1 Experimental branching ratios

The efficiency of the detectors is taken into account when evaluating the relative peak intensities, and so, by applying equation (2.29), the experimental $B(\mathrm{E2})/B(\mathrm{E1})$ values have been calculated. The results for ^{156}Er, ^{158}Dy and ^{160}Er, shown in figures 5.1, 5.2, show very distinct staggering, with the relative quadrupole (in-band) strength between the even- and odd-spin states being systematically stronger by an order of magnitude. The staggering and magnitudes are consistent with the results found for other nuclei in the mass region [13], including ^{160}Yb, ^{154}Gd and ^{156}Gd, although the ratio is substantially smaller in the $N = 88$ nucleus (^{156}Er) that in those with $N = 90$ and $N = 92$.

The difference may not be entirely unexpected, due to the slight differences in character of the out-of-band transition in the two cases. The E1 gamma rays emitted from the odd-spin states are stretched $I \rightarrow I - 1$, whereas the

even spin states, forced to decay to the even spin ground band, are of an unstretched nature $I \rightarrow I$. A similar effect has been observed in decays out of two-quasiparticle bands [62], wherein it was noted that "This relation can be understood by considering the fact that it is most efficient for a single-particle state with strongly aligned spin to emit a photon in the direction of the alignment."

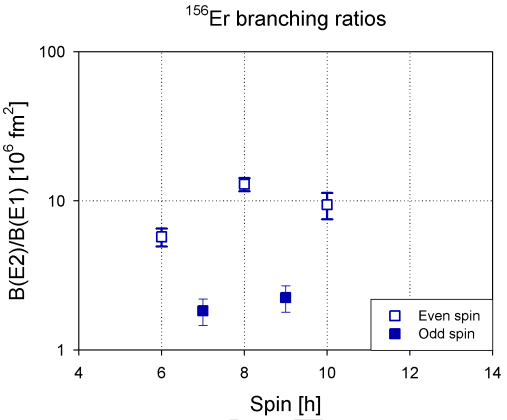

Figure 5.1: Ratio of reduced transition probabilities for the in-band E2 and the out-of-band E1 transitions for the octupole vibrational states in ^{156}Er. The $9^- \rightarrow 7^-$ 'in-band' transition is from the quasiparticle to the vibrational band.

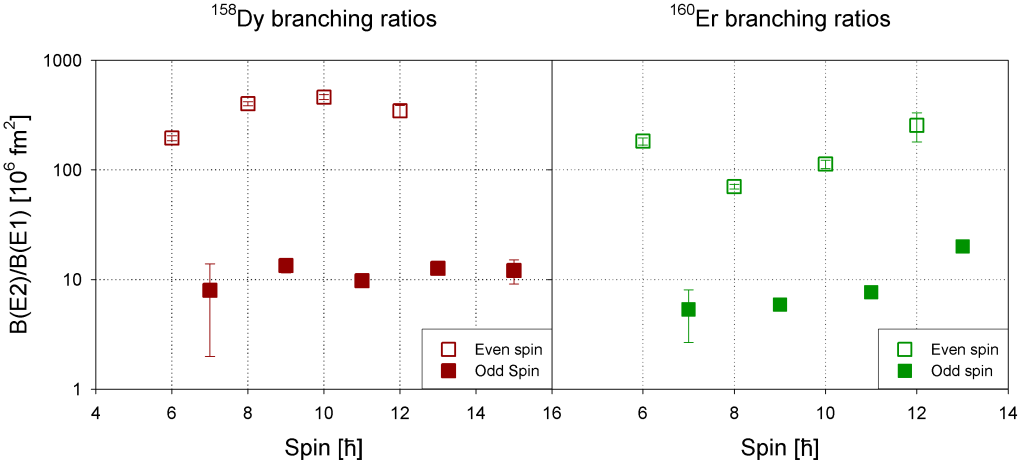

Figure 5.2: Ratio of reduced transition probabilities for the in-band E2 and the out-of-band E1 transitions for the octupole vibrational states in the studied $N = 92$ nuclei.

The secondary, crucial, observation is that in both nuclei the presented ratio remains fairly constant as one moves from low to medium spin states. There is no evidence for any change in character in either band as a function of spin, contradicting the hypothesis that these bands exhibit tetrahedral symmetry only at low spin.

5.2 Systematic study

The three experiments discussed here have not been the first to probe the structure of low lying negative parity bands in the region. Other people and facilities have performed experiments to study the negative parity bands in the rare earth nuclei in detail [63, 64, 65, 66, 67], allowing for a systematic study to be performed. The data for the octupole bands in ^{158}Er is a preliminary result from another experiment at iThemba LABS.

A large portion of the data collected for the testing of the tetrahedral hypothesis has been in the Gd-Yb region around $N = 90$. Band's excitation energies, less rigid-rotor reference ($A = 7.7$ keV) are shown in 5.3. Based on the ground band structure, the Harris parameters for each nucleus could be fitted (table 5.1), and the Routhian (figure 5.4) and alignments (figure 5.5) of the octupole candidate bands have calculated.

University of Cape Town

	$N = 88$	$N = 90$	$N = 92$
$Z = 70$ (Yb)	$\mathcal{J}_0 = 4\ \hbar^2/\text{MeV}$ $\mathcal{J}_1 = 190\ \hbar^4/\text{MeV}^3$	$\mathcal{J}_0 = 10\ \hbar^2/\text{MeV}$ $\mathcal{J}_1 = 185\ \hbar^4/\text{MeV}^3$	$\mathcal{J}_0 = 18\ \hbar^2/\text{MeV}$ $\mathcal{J}_1 = 160\ \hbar^4/\text{MeV}^3$
$Z = 68$ (Er)	$\mathcal{J}_0 = 1.9\ \hbar^2/\text{MeV}$ $\mathcal{J}_1 = 250\ \hbar^4/\text{MeV}^3$	$\mathcal{J}_0 = 15\ \hbar^2/\text{MeV}$ $\mathcal{J}_1 = 210\ \hbar^4/\text{MeV}^3$	$\mathcal{J}_0 = 23\ \hbar^2/\text{MeV}$ $\mathcal{J}_1 = 175\ \hbar^4/\text{MeV}^3$
$Z = 66$ (Dy)	$\mathcal{J}_0 = 3\ \hbar^2/\text{MeV}$ $\mathcal{J}_1 = 375\ \hbar^4/\text{MeV}^3$	$\mathcal{J}_0 = 22\ \hbar^2/\text{MeV}$ $\mathcal{J}_1 = 240\ \hbar^4/\text{MeV}^3$	$\mathcal{J}_0 = 31\ \hbar^2/\text{MeV}$ $\mathcal{J}_1 = 140\ \hbar^4/\text{MeV}^3$
$Z = 64$ (Gd)	$\mathcal{J}_0 = 1.9\ \hbar^2/\text{MeV}$ $\mathcal{J}_1 = 430\ \hbar^4/\text{MeV}^3$	$\mathcal{J}_0 = 24\ \hbar^2/\text{MeV}$ $\mathcal{J}_1 = 245\ \hbar^4/\text{MeV}^3$	$\mathcal{J}_0 = 33\ \hbar^2/\text{MeV}$ $\mathcal{J}_1 = 190\ \hbar^4/\text{MeV}^3$

Table 5.1: Harris parameters (2.17) used for making figures 5.4 and 5.5

It can be easily observed that the neutron number is the dominant factor in the gross structure of the bands, with all the $N = 88$ nuclei displaying a transitional structure: the ground state bands do not follow the $E \sim I(I+1)$ approximation which is representative of a good rotor.

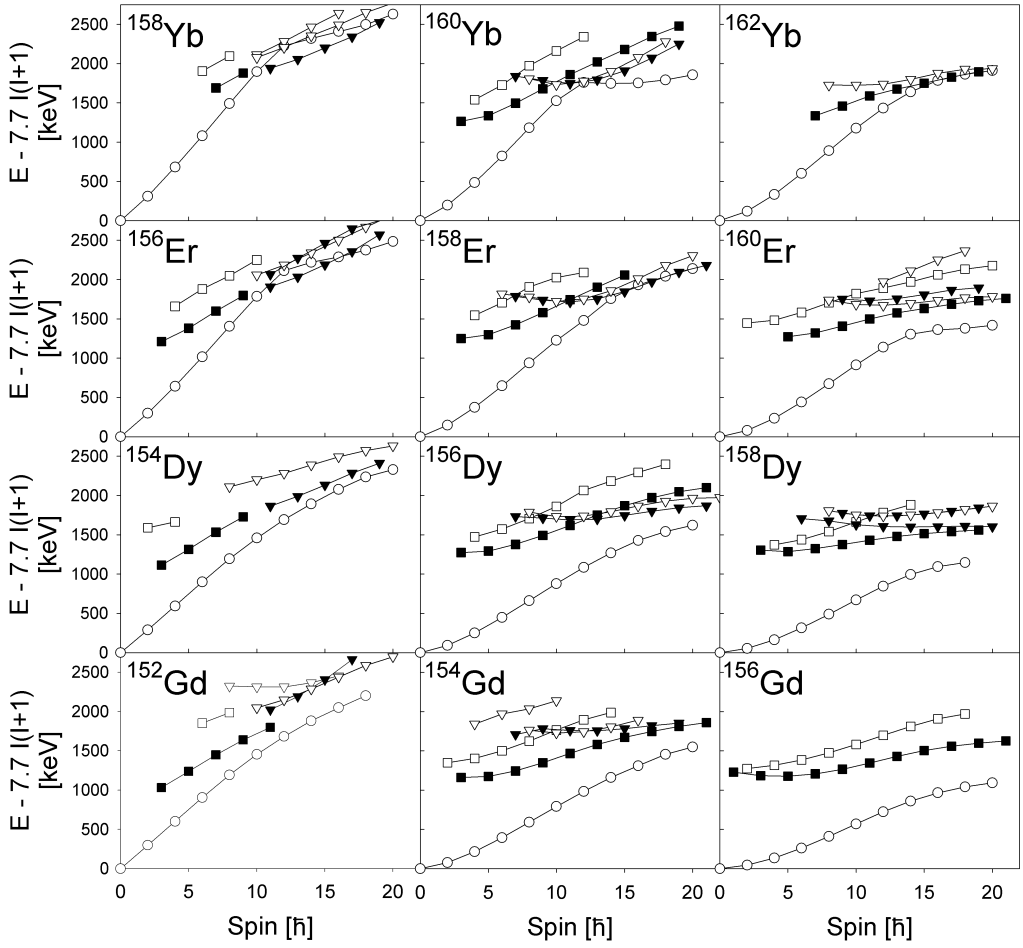

Figure 5.3: The low-lying negative parity bands in the rare-earth region, for $N = 88, 90, 92$, and $Z = 64, 66, 68, 70$. The ground band has been included (open circles), and a constant rigid rotor reference frame has been subtracted. Open symbols represent even spin, while closed symbols represent odd spin states. The *octupole*-like bands have been marked with squares.

The non-rotor structure of the $N = 88$ nuclei does slightly undermine the motivation of translating the bands into the intrinsic (rotating) frame. Nonetheless this can remain a meaningful interpretation, provided the extrapolation to low ω is not necessary. For $N = 90$ and $N = 92$ nuclei, when known, the odd and even spin octupole bands show a fairly consistent behaviour.

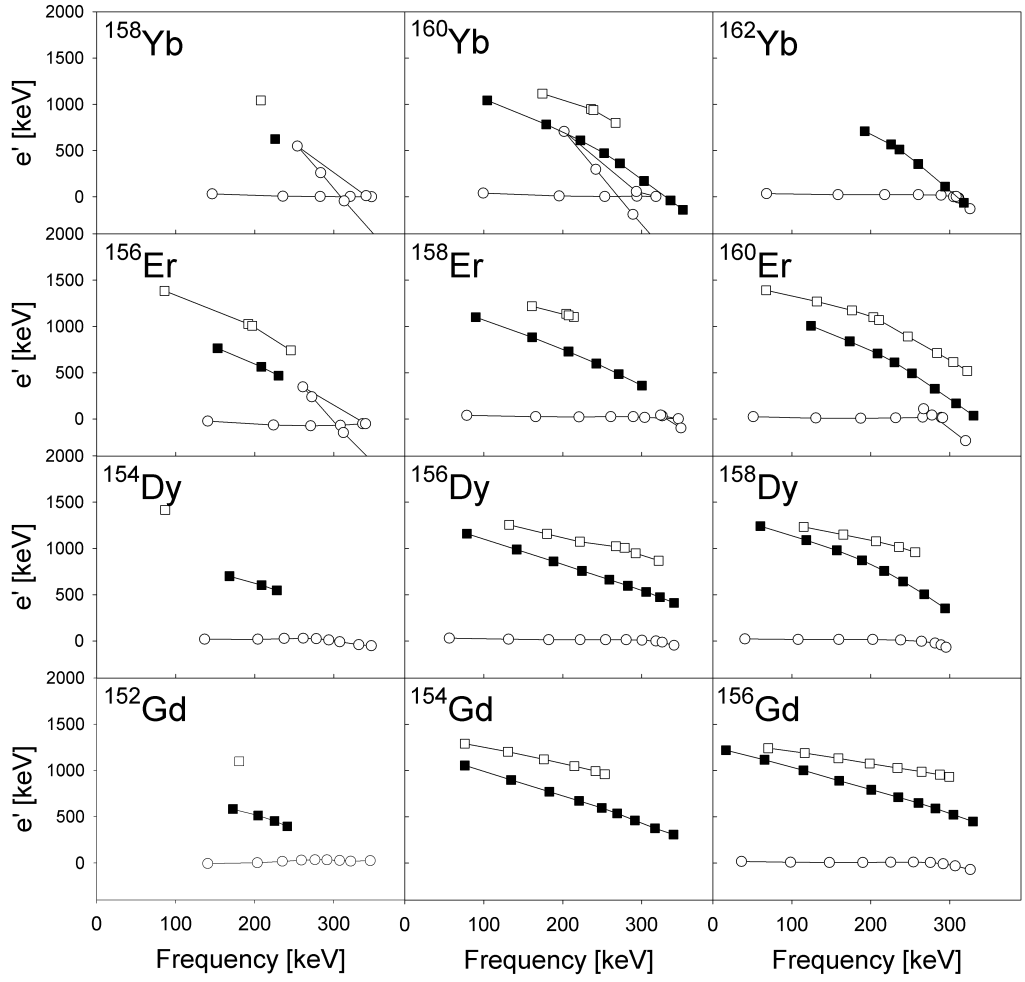

Figure 5.4: Routhian plots of octupole-like bands in the rare-earth region, for $N = 88, 90, 92$, and $Z = 64, 66, 68, 70$. The ground band has been included (open circles) for comparison. Open symbols represent even spin, while closed symbols represent odd spin states.

The octupole bands in $N = 90, 92$ nuclei form an odd-even pair, with the odd spin partner having lower excitation energy (and slow on the E-I plot). The aligned angular momenta at low ω remain consistent with the $K = 0$, $K = 1$ picture, with the even spin band carrying $2\hbar$, and the odd spin band carrying $3\hbar$. This changes once the bands mix with the quasiparticle bands, usually near $\omega \sim 250$ keV (in Gd the crossing occurs at a higher frequency).

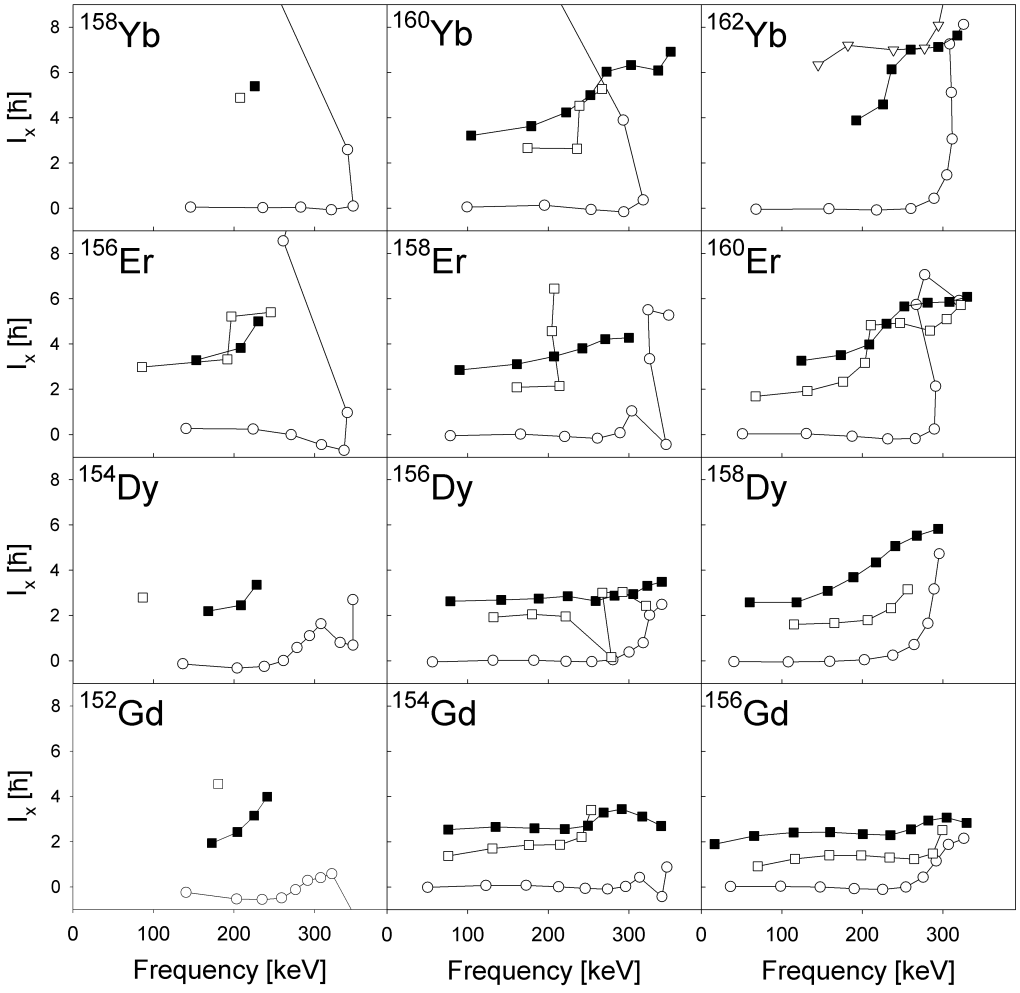

Figure 5.5: Alignment plots of octupole-like bands in the rare-earth region, for $N = 88, 90, 92$, and $Z = 64, 66, 68, 70$. The ground band has been included (open circles) for comparison. Open symbols represent even spin, while closed symbols represent odd spin states.

5.3 Signature in vibrational bands

In all even-even nuclei in the rare earth region, there is a difference in excitation energy between the odd- and even-spin octupole bands, with the even spin states systematically lying several hundred keV higher in energy. The basic interpretation of this phenomenon is that the lowest observed odd-spin band is the $K^\pi = 0^-$ octupole band, whereas the even-spin band is one signature of the $K^\pi = 1^-$ doublet. The repulsion between the odd-spin $K = 1$ and $K = 0$ bands would increase the energy spacing between them, pushing the second odd-spin octupole band higher up in energy than the even-spin octupole.

However, this rather simple explanation must be abandoned, as it makes definitive predictions which disagree with the experimental evidence collected.

- If the $K = 0$ band started lower in energy than the $K = 1$ band (whose unperturbed position is represented by the even-spin band), the $K = 0$ band would be displaced by ~ 250 keV from its unperturbed position, implying that the $K = 1$ odd-spin octupole band must lie within that energy range of the even-spin band.

- If the low $B(\mathrm{E2})/B(\mathrm{E1})$ value for the ($K = 0$) odd-spin band is due to the K dependence, the $K = 1$ odd-spin band should have (relatively) strong in-band transitions.

The existence of a second odd-spin octupole band with strong in-band transitions is not observed in any nuclei in the Gd-Yb region. The second octupole structure has been seen in ^{152}Sm [68, 69]. There is also strong evidence that in other nuclei in the region, the $K = 1$ band is in fact the lowest octupole structure [29, 70], although due to the interaction between various K states the energy levels are often shifted, leading to $K \neq 0$ bands being staggered.

The interaction between states of different K can be extended to treating the octupole vibrational states as mixtures of good-K states. The mixing

University of Cape Town

interaction is limited to states of a like integer parity[1], leading to a set of two non-interacting structures – much like the formalism of signature defined for quasiparticle states. The octupoles can be separated into odd-spin states, corresponding to $\alpha = 1$, and even-spin states, for $\alpha = 0$.

5.4 RPA calculations

The RPA framework, described briefly in section 2.4, involves taking the Hamiltonian of a rotating nucleus, with the addition of multipole-multipole interaction terms to account for the residual interaction. The model allows for the solution of energy eigenvalues (excitations of the rotating vacuum state), with their associated interaction strength (E1). For general excitations all terms that preserve the relevant parity (dipole and octupole) need to be included in the calculations. Since the octupole terms are treated as having good signature, the multipole operators involved need only be those of the chosen signature.

Within the signature-dependant RPA code, the multipole operators used are the (anti)symmetric combinations of the spherical harmonics $Y_{l\,\pm m}$, with

$$\hat{Q}_{lms} \equiv r^l \left(Y_{l\,m} + sY_{l\,-m}\right) \qquad \text{with } s = \pm 1,\ m \geq 1. \tag{5.1}$$

For $m = 0$ there can be no anti-symmetric operator, thus

$$\hat{Q}_{l0} \equiv r^l Y_{l0}. \tag{5.2}$$

Such a construction allows every transition operator to have a good signature quantum number, satisfying

$$\hat{S}_z \hat{Q}_{lms} = (-1)^{l+m} s\ \hat{S}_z \hat{Q}_{lms}. \tag{5.3}$$

As such, for calculating positive signature excitations, only four interactions

[1]Integer parity refers to the value modulo 2.

University of Cape Town

needed to be included in (2.24): $\hat{Q}_{11+}$, $\hat{Q}_{31+}$, $\hat{Q}_{32-}$, and $\hat{Q}_{33+}$. whereas the six terms $\hat{Q}_{10}$, $\hat{Q}_{11-}$, $\hat{Q}_{30}$, $\hat{Q}_{31-}$, $\hat{Q}_{32+}$, $\hat{Q}_{33-}$ were used for calculating negative signature states.

The dipole interactions strengths κ_{1m} were all taken as equal, with a value that showed agreement between the RPA calculations and the experimental excitation energies of the giant dipole resonance. The octupole interaction strengths were variable between nuclei, but kept constant once specified. The exact values were chosen so as to, at some fixed frequency ω_0, fit the lowest RPA solution to the experimentally inferred value. While this did not specify a unique set of κ_{3ms} values, uniqueness was forced by taking all the octupole interaction strength terms as constant for a given signature, termed κ_+ and κ_- for positive ($\alpha = 0$) and negative ($\alpha = 1$) signature states respectively.

For performing the calculations, the Tilted Axis Cranking code is run initially, to evaluate the quasiparticle excitations of the h_{2qp} Hamiltonian at a given rotational frequency ω. The expected value of the vibrational excitation (which is lowest excitation at low ω) is then used to fit the strength of the effective octupole interactions. Once set, the TAC and RPA calculations are performed over a set of frequencies from 10 keV to 250 keV. The RPA solutions can be expressed as a set of doublets: (energy and B(E1)), for every ω. A distribution of the quasiparticle components of the excitation can also be extracted, but this is useful primarily for isolating pure quasiparticle states. In order to extract 'band' structures, the RPA calculations need to performed over a fairly dense set of frequencies and a band must be "traced" based on continuity in energy and excitation strength. The vibrational excitations, being collective, are expected to have significantly higher B(E1) strengths, and this will be exploited when identifying the bands through crossings.

One downside to the RPA framework is its inability to distinguish states of different parity. The parity of excited states is implicitly set to negative (via E1 excitation), and the framework also introduces an interaction between the TAC vacuum (yrast) states and the excitations [71]. As such, the first band-crossing occurs at lower ω than expected, and the results become erratic past that point.

University of Cape Town

5.4.1 ^{158}Dy

The $B(\mathrm{E2})/B(\mathrm{E1})$ data is more significant for the $N = 92$ nuclei (which are also better rotors), so the RPA calculations for these nuclei will be discussed first. The results of the calculations are shown below.

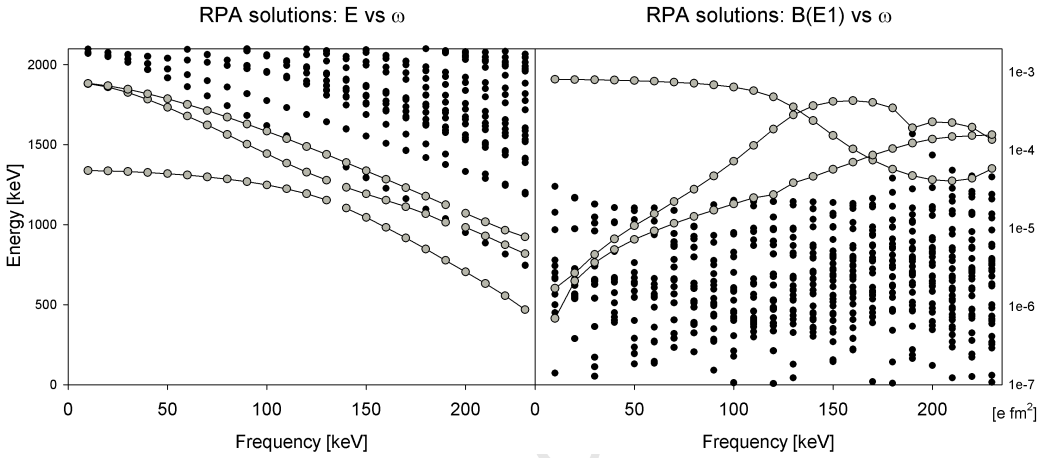

Figure 5.6: RPA energies and $B(\mathrm{E1})$ strengths for ^{158}Dy positive signature states. Three low-lying bands are highlighted. Note the exchange of character of the lowest two bands at $\omega \sim 135$ keV.

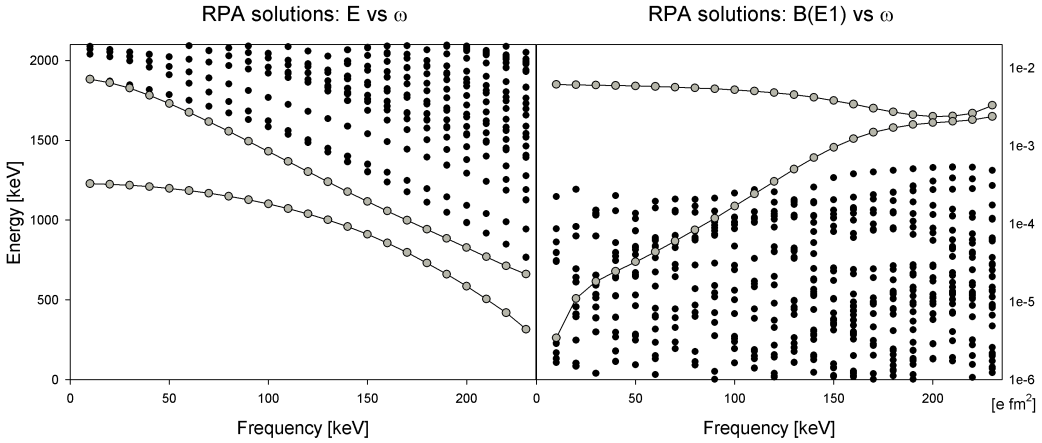

Figure 5.7: RPA energies and $B(\mathrm{E1})$ strengths for ^{158}Dy negative signature states. Two low-lying bands are highlighted. Note the very strong mixing between the two highlighted bands after $\omega \sim 150$ keV

The negative signature vibrational states are calculated as interacting more strongly with the purer quasiparticle excitations than the positive signature states, but the key observation is that the $B(\mathrm{E1})$ strength shows an order of magnitude difference, as predicted by Hamamoto and Sagawa [62].

By estimating the $B(\mathrm{E2})$ value to be similar for octupole bands as for the (quadrupole deformed) ground band, a value $B(\mathrm{E2})/B(\mathrm{E1})$ can be computed, for comparison with the experimentally inferred values, as shown below.

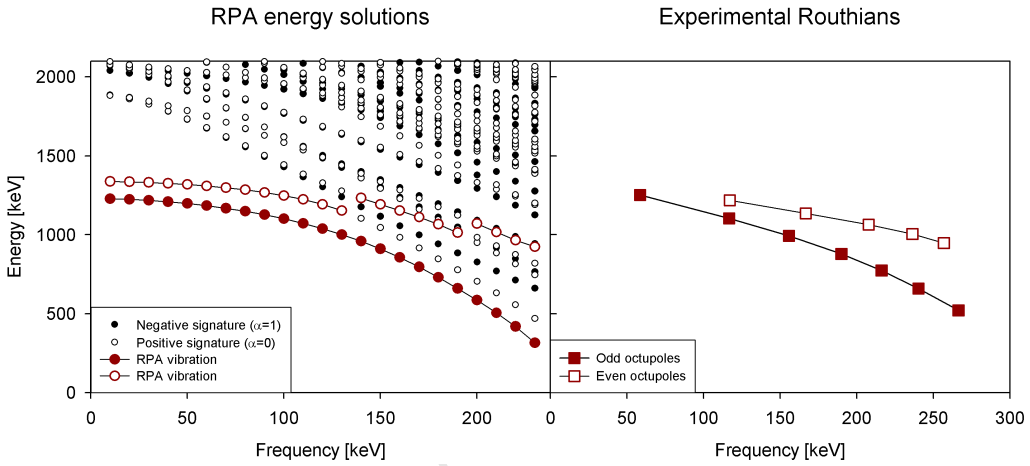

Figure 5.8: RPA calculations for the energies of the positive and negative signature states in ^{158}Dy, compared to the experimentally observed states.

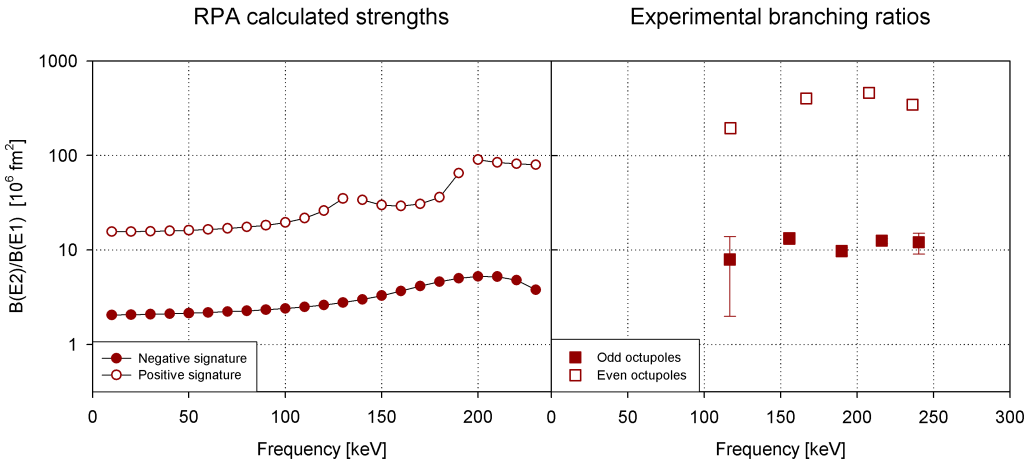

Figure 5.9: RPA calculations for the $B(\mathrm{E2})/B(\mathrm{E1})$ rates for the positive and negative signature states in ^{158}Dy, compared to values obtained from the experimentally observed branching ratios.

5.4.2 ^{160}Er

The same procedure can be applied to the other $N = 92$ nucleus (shown in figures 5.10 and 5.11): the main differences in behaviour at low excitation are due to a different quadrupole deformation, as the quasiproton excitations remain relatively high in energy for $\omega < 250$ keV.

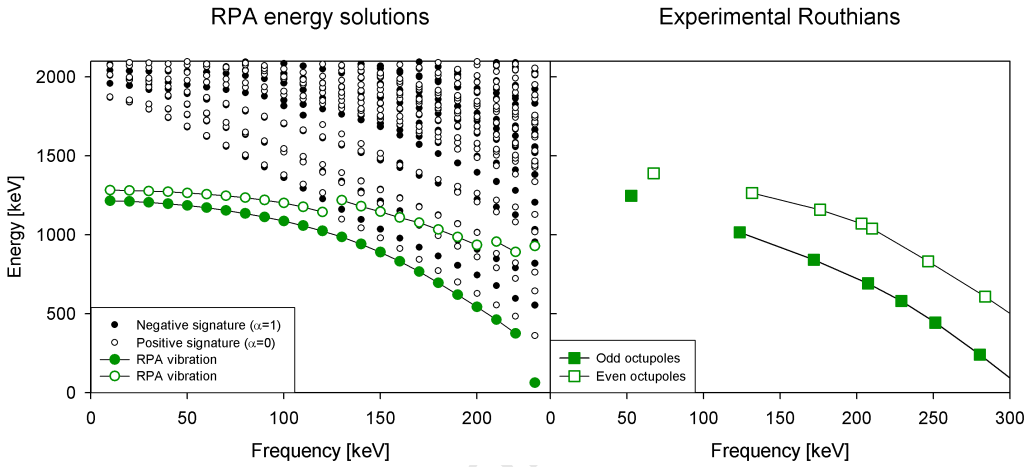

Figure 5.10: RPA calculations for the energies of the positive and negative signature states in ^{160}Er, compared to the experimentally observed states.

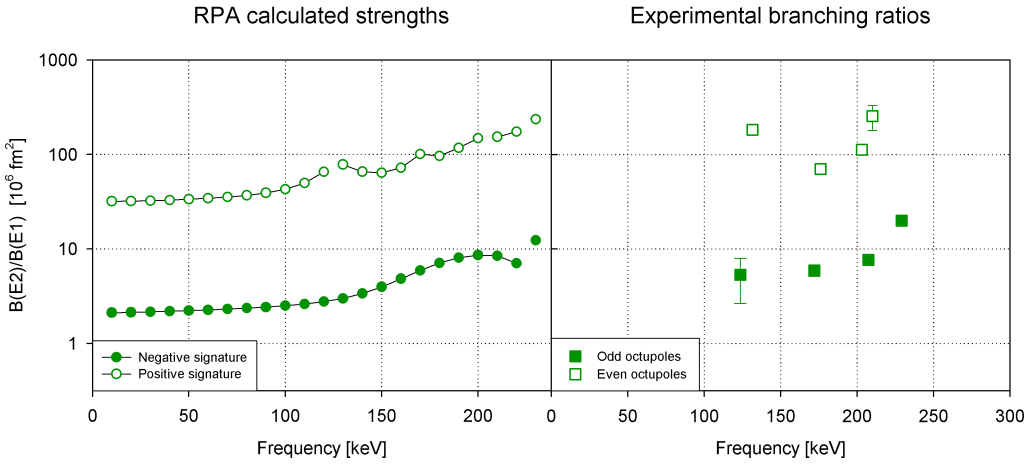

Figure 5.11: RPA calculations for the $B(\mathrm{E2})/B(\mathrm{E1})$ rates for the positive and negative signature states in ^{160}Er, compared to values obtained from the experimentally observed branching ratios.

5.4.3 ^{156}Er

The calculations for the $N = 88$ nucleus (below), are far less inspiring that those for the $N = 92$ nuclei. While the experimental data still displays a form of staggering, the RPA calculations suggest that the B(E1) strength should be comparable in the positive and negative signature states.

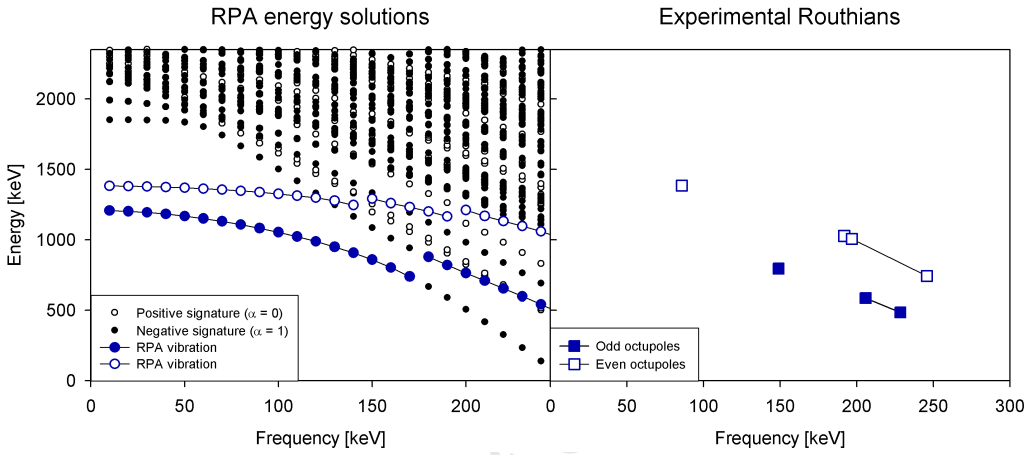

Figure 5.12: RPA calculations for the energies of the positive and negative signature states in ^{156}Er, compared to the experimentally observed states. Unlinked data points correspond to unobserved transitions in the expected band structure.

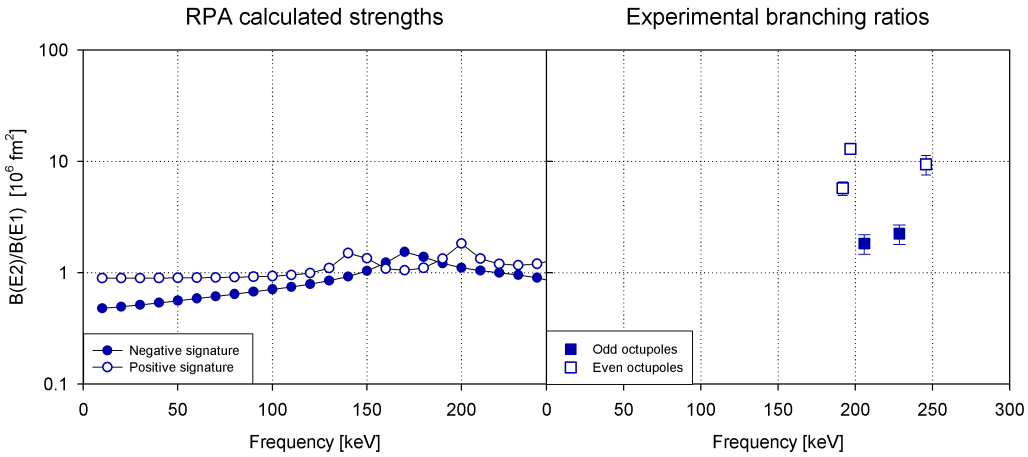

Figure 5.13: RPA calculations for the B(E2)/B(E1) rates for the positive and negative signature states in ^{156}Er, compared to values obtained from the experimentally observed branching ratios.

5.4.4 Systematic RPA calculations

The calculations can also be performed for nuclei in the region, in order to observe systematic trends of the RPA calculations, compared to the systematic experimental trends. Figure 5.14 below shows the experimentally calculated $B(\mathrm{E2})/B(\mathrm{E1})$ ratios, as a function of spin. Since the frequency ω is monotonic up the band, and the RPA $B(\mathrm{E1})$ rates are reasonably constant in ω, an approximate comparison can be made with the intrinsic frame calculations; the results of which are shown in figure 5.14 below.

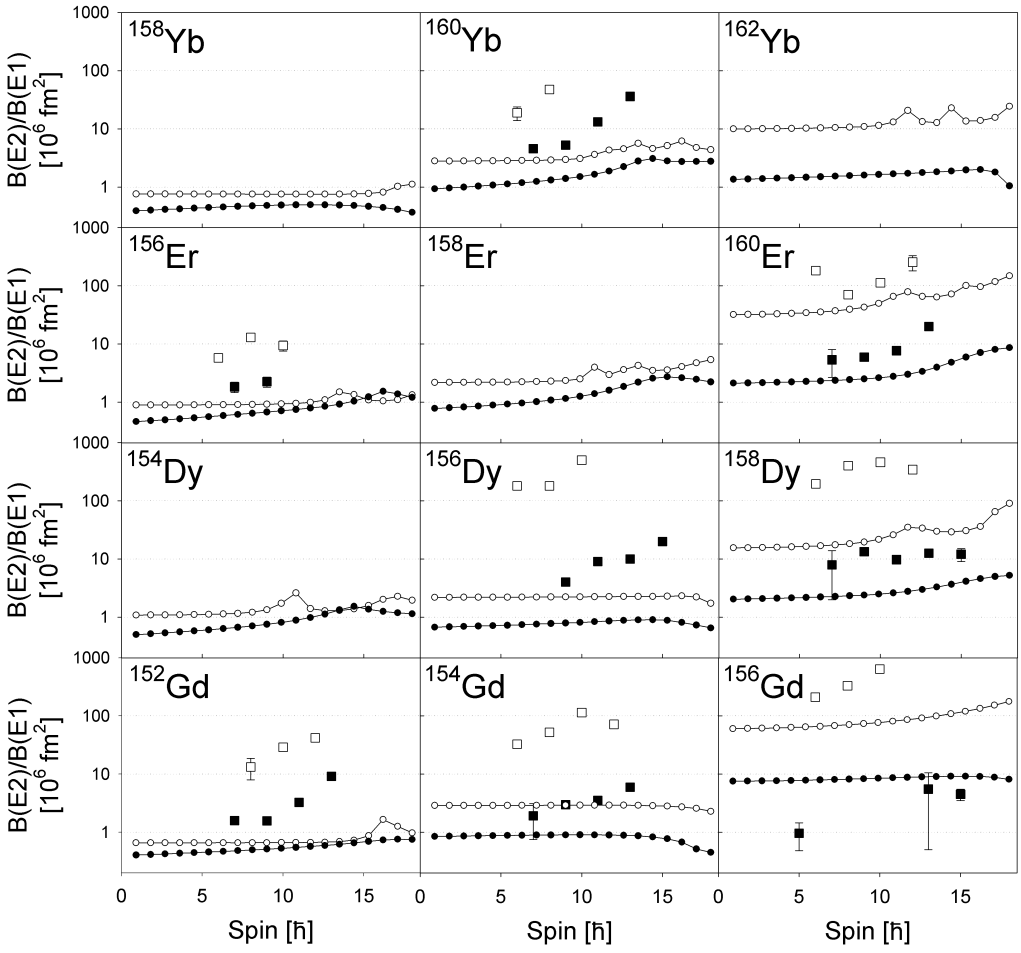

Figure 5.14: The calculated branching ratios, where known, for vibrational states in $N = 88, 90, 92$, and $Z = 64, 66, 68, 70$ nuclei (squares). The RPA-calculated $B(\mathrm{E2})/B(\mathrm{E1})$ rates are overlaid.

The systematic calculations do not, however shown a particularly good agreement with the experimentally known data points. The values of $B(\mathrm{E2})/B(\mathrm{E1})$ and the staggering between the bands of different signature only show quantitative agreement with the data for $N = 92$ nuclei. A form of staggering is regularly obtained for the $N = 90$ nuclei, although to only half the experimentally inferred level, while for for $N = 88$ nuclei, the calculated staggering is minimal, with the calculated values falling significantly below the experimental data points.

When considering the absolute strengths of the octupole interactions, which were obtained through fitting to the data, a certain consistency is observed (shown in table 5.2). The strength for positive signature excitations is higher than for the negative signature, which is to be expected as the low-lying $K = 0$ mode has only a negative signature component. Additionally, the individual strengths decrease as the mass number A increases; an effect that is consistent with reproducing low-spin excitations in a body with a higher number of participant nucleons (equivalent to the moment of inertia for rotational bands).

University of Cape Town

	$N = 88$	$N = 90$	$N = 92$
$Z = 70$ (Yb)	$\kappa_+ = 2.091 \times 10^{-5}$ $\kappa_- = 2.007 \times 10^{-5}$	$\kappa_+ = 1.962 \times 10^{-5}$ $\kappa_- = 1.879 \times 10^{-5}$	$\kappa_+ = 1.913 \times 10^{-5}$ $\kappa_- = 1.853 \times 10^{-5}$
$Z = 68$ (Er)	$\kappa_+ = 2.107 \times 10^{-5}$ $\kappa_- = 2.012 \times 10^{-5}$	$\kappa_+ = 2.037 \times 10^{-5}$ $\kappa_- = 1.931 \times 10^{-5}$	$\kappa_+ = 1.956 \times 10^{-5}$ $\kappa_- = 1.838 \times 10^{-5}$
$Z = 66$ (Dy)	$\kappa_+ = 2.155 \times 10^{-5}$ $\kappa_- = 2.051 \times 10^{-5}$	$\kappa_+ = 2.122 \times 10^{-5}$ $\kappa_- = 1.981 \times 10^{-5}$	$\kappa_+ = 2.024 \times 10^{-5}$ $\kappa_- = 1.879 \times 10^{-5}$
$Z = 64$ (Gd)	$\kappa_+ = 2.276 \times 10^{-5}$ $\kappa_- = 2.128 \times 10^{-5}$	$\kappa_+ = 2.190 \times 10^{-5}$ $\kappa_- = 2.009 \times 10^{-5}$	$\kappa_+ = 2.088 \times 10^{-5}$ $\kappa_- = 1.861 \times 10^{-5}$

Table 5.2: Octupole interactions strengths, as found when fitting the vibrational RPA solutions to the experimental Routhians.

Finally, it is worth noting that the RPA calculations are virtually always below the experimental data, giving no evidence of the $B(\mathrm{E2})$ rate (and hence quadrupole moment) for the octupole vibrational modes being reduced.

5.5 Discussion

The results of the RPA calculations show good agreement with the experimental data collected for ^{158}Dy and ^{160}Er, but not for ^{156}Er, and this can be extended to nuclei of $N = 92$ and $N = 88$ respectively.

A particular difficulty with the interpretation of the calculations in ^{156}Er is the mixing between the, quite strongly populated, quasiparticle bands and the vibrational states. This is experimentally observed, but the RPA model is particularly susceptible to such a mixing given that it characterizes all the states in term of signature (and implicitly, parity), and ignores any physical characterizations which would affect the interaction strength between two band structures.

Since the RPA also mixes the excitations with the vacuum state, above a frequency of 200 keV the vibrational bands cannot be considered as pure states within this framework. Unfortunately, for the $N = 88$ nuclei, which display a transitional character, attempts to describe the system at lower frequency are fundamentally crippled, as the rotational model cannot be applied. In such cases, the RPA framework is not the appropriate environment for describing the vibrational excitations.

In the nuclei whose ground state configurations have excitations consistent with a good rotor (which ^{158}Dy and ^{160}Er are, having $E_{4^+} > 3E_{2^+}$), the RPA model remains applicable, reasonably reproducing the experimentally observed phenomena as single octupole phonon excitations of rotating nuclei. This is not, however, reproduced in nuclei of a more transitional character.

University of Cape Town

Chapter 6

Conclusion

University of Cape Town

The field of studying nuclear structure through gamma-ray spectroscopy has been expanding recently with the development of arrays containing numerous HPGe detectors, which has in turn pushed the gamma-ray spectroscopy into the realm of high γ multiplicity reaction studies. These experiments allow the study of states of higher spin and excitation energy than ever before, unveiling exciting nuclear structures like super-deformed bands, band-termination and triaxiality [50, 54, 56], all in the same region of the nuclear landscape.

It is important to push the limits of our nuclear understanding to ultra-high spin states, but it is no less important to understand the structure of low-spin states, when the Coriolis interaction remains small: the realm of vibrational states. This work has focused on this family of excitations in even-even nuclei in the $(Z, N) \sim (70, 90)$ region.

Experiments to study $^{156}_{68}$Er, $^{160}_{68}$Er and $^{158}_{66}$Dy had been performed at the AFRODITE spectrometer (described in chapter 4), and in every case the in-band transitions within the negative parity vibrational bands have been observed down to spins 4^- and 5^- respectively. The relative strengths of these interactions show a staggering between the odd- and even-spin bands, which extends relatively smoothly from low to medium spin states. This behaviour indicates that a single structure underlies the entire band. This is in strong disagreement with the picture of a tetrahedrally deformed band

[9, 10, 11] at low spin. The lack of observation of in-band transitions at low-spin in the region can in fact be attributed to the competition between the low-energy E2 in-band transitions, and the high-energy E1 transitions to the ground state band.

To reconcile the experimental results with a theory, calculations have been performed within the RPA framework, in order to model the behaviour of a single vibrational phonon aligned with a nuclear rotation. The results (described in chapter 5) offer qualitative agreement with the data, in that the theory predicts an order of magnitude difference between the strengths of the negative and positive signature collective excitations. These B(E1) strengths correlate well with the experimentally observed 'suppression' of the B(E2)/B(E1) branching ratios, which also show an order of magnitude difference between the odd- and even-spin octupole band partners. The apparent suppression of the in-band quadrupole transitions can be understood in the model as a strengthening of the out-of-band dipole strength, if the B(E2) rate is taken as consistent with that for a quadrupole deformation as known for the ground state band. Or, stated in terms of the underlying physics: in the RPA framework, the collective modes are constructed out of a set of single-particle basis states, which have been known to display strongly signature-dependent B(E1) strengths [62], and this signature dependence is carried over to the vibrational modes.

Furthermore, a systematic study of the observed negative parity structures in the rare-earth region has been performed (figures 5.3-5.5), and there is a clear similarity between the bands observed for various N isotones. The systematically self-consistent behaviour suggests that these negative parity bands all share the same structure, and in several nuclei the octupole bands have been inferred to have large quadrupole moments [13, 66], which strongly disagrees with the tetrahedral hypothesis. The lack of distinctly differing structures is evidence that there are likely no tetrahedral structures in the low spin states in the mass 160 region at all.

University of Cape Town

Appendix A

Reaction selection details

University of Cape Town

In order to find the most suitable reaction to study a particular nucleus, several calculations are necessary. At iThemba LABS, the programs `RBR` and `FUSION` were used to decide on the ideal reactions.

A.1 `Reaction`

This program, written by Klaus Schiffer and Johan Nyberg (NBI), considers fusion reactions with neutron, protons and α particles emitted, where limits can be set on the numbers of emitted particles. The atomic masses are read in from a file, and the missing masses are calculated using the Lysekil liquid drop model, including shell corrections (based on a program `ALICE` by F. Plasil and M. Blann). The Coulomb energy, l_{max}(classical), and the fusion cross-section are calculated using formulae from an article by Pelte and Schwalm (Heavy Ion Collisions, ed. BOCK, Vol 3, p. 239).

As the purpose of the experiments was to study low-lying states, the ideal reactions would emit only a few particles, and it was decided to consider only neutron evaporation reactions. The program was run with $2 \leq N_n \leq 4$ and no proton or α emissions.

The following search was done for the final nucleus Dy with Amin = 158, Amax = 158 :
The projectile was Zmin = 2, Zmax = 10
Number of emitted alpha particles Minalpha = 0, Maxalpha = 0
Number of emitted protons Minp = 0, Maxp = 0
Number of emitted neutrons Minn = 2, Maxn = 4
Number of emitted particles Minpart = 2, Maxpart = 4

List of possible reactions leading to 158Dy (Z=66,N=92) (stable isotope) :

Reaction	ZP	NP	ZT	NT	Coulomb Barrier (MeV) CM	Coulomb Barrier (MeV) LAB	Projectile Energy (MeV) CM	Projectile Energy (MeV) LAB	Compound-Nucl. Q(MeV)	Compound-Nucl. E*(MeV)	Reaction Q-value (MeV)	lmax (hbar)	Fusion x-sect. (mb)	v/c Proj. (%)	v/c CN (%)
157Gd(3He,2n)	2	1	64	93	17.83	18.17	25.63	26.12	13.78	39.41	-1.63	10	953.8	13.64	0.26
158Gd(3He,3n)	2	1	64	94	17.81	18.15	35.57	36.24	12.29	47.86	-9.57	15	1499.4	16.06	0.30
156Gd(a,2n)	2	2	64	92	17.60	18.05	39.85	40.87	-0.44	39.41	-15.85	20	1768.1	14.81	0.37
157Gd(a,3n)	2	2	64	93	17.58	18.03	48.21	49.43	-0.35	47.86	-22.21	23	1920.5	16.28	0.40
158Gd(a,4n)	2	2	64	94	17.57	18.01	58.14	59.62	-0.09	58.06	-30.14	27	2180.3	17.88	0.44
153Eu(7Li,2n)	3	4	63	90	25.29	26.45	28.20	29.49	11.21	39.41	-4.20	10	381.3	9.50	0.42
152Sm(9Be,3n)	4	5	62	90	32.71	34.65	43.22	45.78	4.64	47.86	-17.22	21	823.0	10.44	0.58
148Nd(12C,2n)	6	6	60	88	46.79	50.59	47.14	50.96	-7.74	39.41	-23.14	4	25.0	9.55	0.72
150Nd(12C,4n)	6	6	60	90	46.69	50.43	63.56	68.65	-5.50	58.06	-35.56	31	918.9	11.08	0.82
148Nd(13C,3n)	6	7	60	88	46.53	50.62	54.09	58.84	-6.23	47.86	-28.09	22	512.1	9.86	0.80
142Ce(18O,2n)	8	10	58	84	58.93	66.40	55.05	62.03	-15.64	39.41	-31.05	0	0.0	8.60	0.97
138Ba(22Ne,2n)	10	12	56	82	70.31	81.52	66.03	76.55	-26.62	39.41	-42.03	0	0.0	8.65	1.19

Table A.1: List of reactions using stable beams and projectiles resulting in formation of ^{158}Dy

University of Cape Town

List of possible reactions leading to 160Er (Z=68,N=92) (unstable isotope) :

Reaction	ZP	NP	ZT	NT	Coulomb Barrier (MeV) CM	Coulomb Barrier (MeV) LAB	Projectile Energy (MeV) CM	Projectile Energy (MeV) LAB	Compound-Nucl. Q(MeV)	Compound-Nucl. E*(MeV)	Reaction Q-value (MeV)	lmax (hbar)	Fusion x-sect. (mb)	v/c Proj. (%)	v/c CN (%)
160Dy(3He,3n)	2	1	66	94	18.33	18.67	38.90	39.63	10.43	49.33	-12.90	16	1553.2	16.80	0.31
161Dy(3He,4n)	2	1	66	95	18.31	18.65	47.36	48.24	12.82	60.17	-19.36	20	1970.0	18.53	0.34
158Dy(a,2n)	2	2	66	92	18.11	18.57	42.07	43.14	-1.65	40.43	-18.07	21	1841.3	15.21	0.38
160Dy(a,4n)	2	2	66	94	18.07	18.53	61.48	63.02	-1.31	60.17	-33.48	28	2214.0	18.39	0.45
154Gd(9Be,3n)	4	5	64	90	33.70	35.67	46.52	49.24	2.81	49.33	-20.52	23	912.9	10.83	0.60
155Gd(9Be,4n)	4	5	64	91	33.66	35.61	54.96	58.15	5.22	60.17	-26.96	30	1301.4	11.77	0.65
153Eu(10B,3n)	5	5	63	90	41.23	43.92	45.48	48.45	3.85	49.33	-19.48	14	321.8	10.19	0.63
153Eu(11B,4n)	5	6	63	90	40.97	43.91	58.93	63.17	1.24	60.17	-30.93	31	1073.0	11.10	0.74
150Sm(12C,2n)	6	6	62	88	48.25	52.11	51.14	55.23	-10.71	40.43	-27.14	13	209.5	9.94	0.74
152Sm(12C,4n)	6	6	62	90	48.15	51.95	69.00	74.44	-8.82	60.17	-41.00	34	1014.5	11.54	0.84
149Sm(13C,2n)	6	7	62	87	48.03	52.22	48.10	52.30	-7.67	40.43	-24.10	2	6.8	9.29	0.75
150Sm(13C,3n)	6	7	62	88	47.98	52.14	58.09	63.12	-8.76	49.33	-32.09	25	611.9	10.21	0.81
148Nd(16O,4n)	8	8	60	88	61.12	67.72	76.38	84.63	-16.20	60.17	-48.38	34	705.9	10.66	1.04
146Nd(17O,3n)	8	9	60	86	60.97	68.07	65.90	73.57	-16.57	49.33	-39.90	20	273.8	9.64	1.01
145Nd(18O,3n)	8	10	60	85	60.77	68.31	66.37	74.61	-17.05	49.33	-40.37	22	311.5	9.43	1.04
146Nd(18O,4n)	8	10	60	86	60.70	68.19	75.94	85.30	-15.77	60.17	-47.94	36	716.1	10.09	1.11
142Ce(21Ne,3n)	10	11	58	84	72.78	83.54	74.43	85.44	-25.10	49.33	-48.43	13	87.4	9.35	1.20
142Ce(22Ne,4n)	10	12	58	84	72.51	83.74	86.79	100.24	-26.62	60.17	-58.79	39	617.3	9.89	1.33

Table A.2: List of reactions using stable beams and projectiles resulting in formation of ^{160}Er

University of Oslo

List of possible reactions leading to 162Yb (Z=70,N=92) (unstable isotope) :

Reaction	ZP	NP	ZT	NT	Coulomb Barrier (MeV) CM	Coulomb Barrier (MeV) LAB	Projectile Energy (MeV) CM	Projectile Energy (MeV) LAB	Compound-Nucl. Q(MeV)	Compound-Nucl. E*(MeV)	Reaction Q-value (MeV)	lmax (hbar)	Fusion x-sect. (mb)	v/c Proj. (%)	v/c CN (%)
162Er(3He,3n)	2	1	68	94	18.84	19.19	41.88	42.66	8.76	50.64	-15.88	17	1622.8	17.43	0.32
162Er(a,4n)	2	2	68	94	18.58	19.04	64.46	66.05	-2.33	62.13	-36.46	29	2261.9	18.82	0.45
156Dy(9Be,3n)	4	5	66	90	34.68	36.68	49.65	52.52	0.99	50.64	-23.65	25	1006.4	11.19	0.61
152Gd(12C,2n)	6	6	64	88	49.70	53.62	55.11	59.46	-13.73	41.38	-31.11	18	365.0	10.31	0.75
154Gd(12C,4n)	6	6	64	90	49.59	53.46	74.25	80.04	-12.12	62.13	-46.25	38	1172.8	11.97	0.87
152Gd(13C,3n)	6	7	64	88	49.42	53.65	62.06	67.37	-11.42	50.64	-36.06	28	714.7	10.55	0.83
151Eu(14N,3n)	7	7	63	88	56.52	61.76	62.26	68.04	-11.62	50.64	-36.26	20	344.4	10.21	0.87
151Eu(15N,4n)	7	8	63	88	56.24	61.83	75.10	82.56	-12.97	62.13	-47.10	37	897.6	10.87	0.98
148Sm(16O,2n)	8	8	62	86	63.15	69.98	64.48	71.45	-23.09	41.38	-40.48	10	77.3	9.79	0.96
149Sm(16O,3n)	8	8	62	87	63.09	69.86	72.35	80.12	-21.71	50.64	-46.35	27	473.1	10.37	1.01
150Sm(16O,4n)	8	8	62	88	63.02	69.74	82.33	91.12	-20.20	62.13	-54.33	39	857.3	11.06	1.07
148Sm(17O,3n)	8	9	62	86	62.87	70.09	70.62	78.73	-19.98	50.64	-44.62	25	394.9	9.97	1.03
149Sm(17O,4n)	8	9	62	87	62.80	69.97	78.49	87.45	-16.36	62.13	-50.49	36	727.5	10.51	1.08
147Sm(18O,3n)	8	10	62	85	62.66	70.33	70.52	79.16	-19.88	50.64	-44.52	26	406.1	9.72	1.06
148Sm(18O,4n)	8	10	62	86	62.60	70.21	80.66	90.47	-18.53	62.13	-52.66	40	828.8	10.39	1.13
145Nd(20Ne,3n)	10	10	60	85	75.34	85.73	78.95	89.84	-28.31	50.64	-52.95	19	179.1	9.82	1.19
146Nd(20Ne,4n)	10	10	60	86	75.26	85.57	88.52	100.64	-26.39	62.13	-60.52	36	559.6	10.40	1.25
144Nd(21Ne,3n)	10	11	60	84	75.13	86.08	79.96	91.62	-29.32	50.64	-53.96	22	225.9	9.68	1.23
145Nd(21Ne,4n)	10	11	60	85	75.05	85.92	87.71	100.41	-25.58	62.13	-59.71	36	541.6	10.13	1.28
143Nd(22Ne,3n)	10	12	60	83	74.93	86.45	82.50	95.20	-31.86	50.64	-56.50	28	337.7	9.64	1.29
144Nd(22Ne,4n)	10	12	60	84	74.85	86.28	92.32	106.42	-30.19	62.13	-64.32	43	702.5	10.19	1.35

Table A.3: List of reactions using stable beams and projectiles resulting in formation of ^{162}Yb

University of Oslo

It ought to be noted that the program calculates all possible reactions based on stable targets, and stable or semi-stable projectiles. At iThemba LABS the radioactive beam project is only in the planning stages, so the unstable projectiles were not considered. The truncated outputs for reactions to create ^{158}Dy, ^{160}Er and ^{162}Yb are presented in tables A.1-A.3.

A.2 `Fusion`

In order for nuclear reactions to take place, it is necessary for the nuclei to be sufficiently close to each other to allow their constituent nucleons to interact, which requires overcoming the Coulomb barrier. Given a target of atomic mass and proton number (A_1, Z_1), and a projectile beam (A_2, Z_2), the center of mass energy required is

$$E_{CM} = \frac{1}{4\pi\epsilon_0}\frac{Z_1 Z_2 e^2}{r} \approx \frac{1}{4\pi\epsilon_0}\frac{Z_1 Z_2 e^2}{(\sqrt[3]{A_1} + \sqrt[3]{A_2})r_0},$$

where $r_0 \approx 1.2$ fm. In a fixed target experiment however, the compound nucleus is going to recoil with a speed of approximately $\frac{A_2}{A_1+A_2}v$, so the energy of the projectile must be appropriately increased. Using a non-relativistic approximation, this reduces to

$$E_{2,kin} = \frac{(M_{1+2} + E_{CM})^2 - M_{1+2}^2}{2M_1} = \frac{2M_{1+2}E_{CM} + E_{CM}^2}{2M_1} \approx \frac{A_1 + A_2}{A_1}E_{CM},$$

where the second term can be neglected as the Coulomb energy between the nuclei is orders of magnitude smaller than the mass of the compound nuclei.

For a target reaction, the program `FUSION` calculates the classical and quantum parameters for a particular beam/target combination over a range of beam energies. It performs the above calculation using empirically measured data for the nuclear radii and masses (including the reduction due to the binding energy), and in turn it creates a table of kinematic variables corresponding to that of the created compound nucleus. The main program

University of Cape Town

outputs the excitation energy of the compound nucleus, the maximal angular momentum and the total fusion cross section of the reaction, at every specified beam energy. The subsequent decays of the compound nucleus are then derived statistically.

A.3 P.A.C.E.

The results from the FUSION code are taken and fed into the program ZPACE, which is the ORNL-adapted standard version (1980) of the Projection Angular-momentum Coupled Evaporation Monte-Carlo code. The program takes a sample of 10000 nuclei prepared in a state as calculated by the FUSION program, and evaluates the decay of the compound nucleus, until the produced nucleus decays into a state that is strong-interaction stable. The relative yields are then related to the reaction cross sections, which are presented in figures 3.5-3.7.

University of Cape Town

Appendix B

RPA calculations

University of Cape Town

The Random Phase Approximation itself is a rather complicated model, the details of which have been left out of the main text. This treatment here is a summary of the explanations and documentation [31, 72] I received from Fritz Dönau, who wrote the programs for performing the calculations. Most of the material in this chapter is *not* my own work.

B.1 RPA model for separable interactions

B.1.1 Implementation of the interaction

The interaction is implemented through the inclusion of multipole-multipole terms

$$V = -\frac{1}{2}\sum_{\lambda\mu} \kappa^{\lambda\mu} Q_{\lambda\mu} Q^{\dagger}_{\lambda\mu}, \tag{B.1}$$

where $Q^{\dagger}_{\lambda\mu} = (-1)^{\mu} Q_{\lambda\mu}$, and $\kappa_{\lambda\mu}$ is the relevant multipole interaction strength. Defining symmetrized operators, $s = +1$ (hermitian) and $s = -1$ (antihermitian)

$$Q_{\lambda\mu s} = \frac{1}{2}(Q_{\lambda\mu} + sQ^{\dagger}_{\lambda\ -\mu}), \tag{B.2}$$

the interaction can be written as a sum of squares

$$V = -\frac{1}{2}\sum_{\lambda\mu}\kappa^{\lambda\mu}Q_{\lambda\mu}Q^{\dagger}_{\lambda\mu} = -\frac{1}{2}\sum_{\lambda\mu s}\kappa^{\lambda\mu s}(Q_{\lambda\mu s})^2. \tag{B.3}$$

Using a set of spherical basis functions, one may define state $|1\rangle = |nljm\rangle$ and state $|2\rangle = |n'l'j'm'\rangle$. The matrix elements $\langle 1|Q_{\lambda\mu}|2\rangle = \langle 1|Q_{\lambda\mu}|2\rangle^*$ will be then real. As the multipole operators $Q_{\lambda\mu} = f_\lambda(r)Y_{\lambda\mu}$, for the symmetrized operators

$$\langle 1|Q_{\lambda\mu s}|2\rangle = s\,\langle 2|Q_{\lambda\mu}|1\rangle = \frac{1}{2}\left(\langle 1|f_\lambda(r)Y_{\lambda\mu}|2\rangle + s\,\langle 2|f_\lambda(r)Y_{\lambda\mu}|1\rangle\right). \tag{B.4}$$

B.1.2 Quasiparticle operators

The quasiparticle transformation creation c_1^+ and annihilation c_2 operators are defined as

$$c_1^+ = \sum_i (u_{1i}\alpha_i^+ + v_{1i}\alpha_i), \qquad c_2 = \sum_k (u_{2k}\alpha_k + v_{2k}\alpha_k^+), \tag{B.5}$$

where the coefficients u, v are assumed to be real.

Writing the Q-operators in terms of c_1^+ and c_2:

$$\begin{aligned} Q_{\lambda\mu s} &= \sum_{1,2}\langle 1|Q_{\lambda\mu s}|2\rangle\, c_1^+ c_2 \\ &= \sum_{i,k}\sum_{1,2}\langle 1|Q_{\lambda\mu s}|2\rangle\,(u_{1i}v_{2k}\alpha_i^+\alpha_k^+ + u_{2k}v_{1i}\alpha_i\alpha_k), \end{aligned} \tag{B.6}$$

where only the two quasiparticle and two quasihole terms are considered relevant for the RPA. Using the symmetries, the expression can be rewritten as a sum of over independent quasiparticle pairs (termed $i < k$):

$$Q_{\lambda\mu s} = \sum_{i<k}\sum_{1,2}\langle 1|Q_{\lambda\mu s}|2\rangle\,(u_{1i}v_{2k} - u_{1k}v_{2i})(\alpha_i^+\alpha_k^+ + s\alpha_k\alpha_i). \tag{B.7}$$

University of Cape Town

Next, the boson operators $b^+_\varrho = \alpha^+_i \alpha^+_k$ and $b_\varrho = \alpha_k \alpha_i$ are introduced, where the index ϱ corresponds to the index pair of $i < k$. In accordance with the Quasi Boson Approximation, these are treated as exact bosons, and satisfy $[b^+_\varrho, b_{\varrho'}] = \delta_{\varrho,\varrho'}$.

For a full representation, isospin $\tau = \pi, \nu$ must also be included, and for convenience it is written as

$$Q^\tau_{\lambda\mu s} = \sum_\varrho \tilde{F}^{\lambda\mu s}_{\varrho,\tau}(b^+_{\varrho\tau} + s b_{\varrho\tau}) \tag{B.8}$$

$$\tilde{F}^{\lambda\mu s}_{\varrho,\tau} = \sum_{1,2} \left\langle 1|Q^\tau_{\lambda\mu s}|2\right\rangle (u^{(\tau)}_{1i} v^{(\tau)}_{2k} - u^{(\tau)}_{1k} v^{(\tau)}_{2i}). \tag{B.9}$$

Finally, for convenience, define $p = \lambda\mu s$, $\sigma = \pm 1$, to take into account isoscalar ($\sigma = 1$) and isovector ($\sigma = -1$) modes of interaction. A modified strength constant $\tilde{\kappa}$, can be defined as $\tilde{\kappa}^{\lambda\mu}_\sigma = \kappa^{\lambda 0}_\sigma$ for $\mu = 0$, and $\tilde{\kappa}^{\lambda,\mu>0}_\sigma = 2\kappa^{\lambda\mu}_\sigma$ for $\mu > 0$. The complete interaction takes the form

$$V = -\frac{1}{2}\sum_{p,\sigma} \kappa^p_\sigma s (Q^\pi_p + \sigma Q^\nu_p)^2 = -\frac{1}{2}\sum_{p,\sigma} \kappa^p_\sigma s (Q^\sigma_p)^2. \tag{B.10}$$

B.1.3 Derivation of the RPA equations

The complete boson Hamiltonian is

$$H = \sum_{\varrho,\tau} E_{\varrho\tau} b^+_{\varrho\tau} b_{\varrho tau} - \frac{1}{2}\sum_{p,\sigma} \kappa^p_\sigma s (Q^\sigma_p)^2, \tag{B.11}$$

where the first term refers to the diagonal two quasiparticle energies. The phonon operators

$$\hat{\Omega}^+ = \sum_{\varrho,\tau}(R_{\varrho\tau} b^+_{\varrho\tau} - S_{\varrho\tau} b_{\varrho\tau}), \qquad \hat{\Omega}^- = \sum_{\varrho,\tau}(R_{\varrho\tau} b_{\varrho\tau} - S_{\varrho\tau} b^+_{\varrho\tau}) \tag{B.12}$$

satisfy $[\hat{\Omega}, \hat{\Omega}^+] = 1$, assuming real amplitudes R and S. From the RPA equation $[H, \hat{\Omega}^+] = E\hat{\Omega}^+$, and the definition that the lowering operator $b_{\varrho\tau}$

University of Cape Town

acting on the vacuum state gives zero, it can be obtained that

$$\langle b_{\varrho\tau}[H,\hat{\Omega}^+]\rangle \;\; = ER_{\varrho\tau} \;\; = E_{\varrho\tau}R_{\varrho\tau} - \sum_{p,\sigma}\langle b_{\varrho\tau}Q_p^\sigma\rangle s\tilde{\kappa}_\sigma^p[Q_p^\sigma,\hat{\Omega}^+], \quad \text{(B.13)}$$

$$\langle b_{\varrho\tau}[H,\hat{\Omega}]\rangle \;\; = ES_{\varrho\tau} \;\; = -E_{\varrho\tau}S_{\varrho\tau} - \sum_{p,\sigma}\langle b_{\varrho\tau}Q_p^\sigma\rangle s\tilde{\kappa}_\sigma^p[Q_p^\sigma,\hat{\Omega}]. \quad \text{(B.14)}$$

The expectation value $\langle b_{\varrho\tau}Q_p^\sigma\rangle = \tilde{F}_{\varrho\tau}^p(\delta_{\tau\pi}+\sigma\delta_{\tau\nu})$. Defining the constant normalization factor $\tilde{D}_{p\sigma} \equiv s\tilde{\kappa}_\sigma^p[Q_p^\sigma,\hat{\Omega}^+]$, one can solve for the RPA amplitudes:

$$R_{\varrho\tau} \;\; = \;\; \sum_{p,\sigma}\frac{\tilde{F}_{\varrho\tau}^p(\delta_{\tau\pi}+\sigma\delta_{\tau\nu})\tilde{D}_{p\sigma}}{E_{\varrho\tau}-E} \quad \text{(B.15)}$$

$$S_{\varrho\tau} \;\; = \;\; \sum_{p,\sigma}\frac{\tilde{F}_{\varrho\tau}^p(\delta_{\tau\pi}+\sigma\delta_{\tau\nu})s\tilde{D}_{p\sigma}}{E_{\varrho\tau}+E}. \quad \text{(B.16)}$$

For given states p and p' the RPA amplitudes can be combined as

$$X_{pp'}^\tau(E) \equiv \sum_\varrho \tilde{F}_{\varrho\tau}^p\tilde{F}_{\varrho\tau}^{p'}\left(\frac{1}{E_{\varrho\tau}+E}+\frac{ss'}{E_{\varrho\tau}-E}\right), \quad \text{(B.17)}$$

which allows the derivation of an equation for the normalization constants

$$\tilde{D}_{p\sigma} = \kappa_\sigma^p\sum_{p',\sigma'}(X_{pp'}^\pi+\sigma\sigma'X_{pp'}^\nu)\tilde{D}_{p'\sigma'}. \quad \text{(B.18)}$$

Defining the matrix $A = A(p\sigma,p'\sigma')(E) \equiv X_{pp'}^\pi+\sigma\sigma'X_{pp'}^\nu$, the equation (B.18) has solutions iff

$$\left|\left|A_{p\sigma,p'\sigma'}-\frac{1}{\kappa_\sigma^p}\delta_{p\sigma,p'\sigma'}\right|\right| = 0. \quad \text{(B.19)}$$

This is the dispersion relation, the zeros of which correspond to the RPA eigenvalues of the equation of motion $[H,\hat{\Omega}^+] = E\hat{\Omega}^+$.

University of Cape Town

B.1.4 Calculation of the strength constant

In order to solve for the RPA eigenvalues E, one can either perform a direct diagonalization of the matrix form of the equations of motion, or solve the dispersion relation (B.19). The eigenvalues are extremely sensitive to the strength constants κ^p_σ, so in order to obtain a fair starting point, it is worth evaluating the interaction strength to reproduce an experimentally inferred phonon excitation E, which can be obtained from the dispersion relation. Expanding the first line ($p\sigma$) of the determinant, one gets

$$||A(E)|| - \frac{1}{\kappa^p_\sigma} \min ||A_{p\sigma,p\sigma}(E)|| = 0 \quad \Rightarrow \quad \kappa^p_\sigma = \frac{\min ||A_{p\sigma,p\sigma}(E)||}{A(E)}. \quad \text{(B.20)}$$

This allows a direct calculation of the strength constant, which is particularly useful if the dimension of the matrix A is large, due to several multipole interactions being included in the calculation.

B.2 Numerical calculations

The codes used for performing the calculations were written in `Fortran90`, compiled for linux with the Intel `ifort` compiler. I have assisted with testing and debugging of the programs, but sole author/owner of these programs is Fritz Dönau. This section will describe the inputs and methods of calculations.

B.2.1 `TAC3DZ`

The Tilted Axis Cranking, in 3D, with Z-signature symmetry is the preliminary code that calculates the single particle energies of a system subject to a given rotational frequency ω.

University of Cape Town

Inputs

For every nucleus, the single particle energies need to be calculated separately for protons and neutrons. The code can perform calculations for a single parameter set (when performing calculations for the RPA), or over a range of parameter values (when trying to find deformation minima, or investigating ground state configurations and band crossings). As such, the code takes a large number of inputs [31]:

```
IVOL, IDIA, NPOUT, ICYOUT, NPART
A, IP, NL, NU, ICY, IWO, INTPR, NPP, IWW, ELIMDO, ELIMUP
E2L, E4L, GAML, DEL, XLAM, OML, THL, PHIL
VAR
CONFIGURATION
EO, GPAIR
```

The first line consists of various parameters: how to consider volume conservation, how to control configurations (diabatically or adiabatically), number of points in outer parameter loop, index of parameter for outer loop, and the total particle number of the nucleus.

The second line contains: the mass A, the Nilsson model to use, the lower and upper harmonic oscillator shell to be used, the variable of the inner parameter loop, a flag for whether the Fermi energy λ needs to be calculated or specified, the number of quasiparticle levels above/below zero to output to the log files, the number of points in the inner loop, format of wavefunction outputs, and the lower and upper limits of the energy range for outputs of quasiparticle energies.

The third line gives the nuclear properties: deformation parameters ε_2, ε_4, γ, pairing gap Δ, λ, rotational frequency ω, and orientation angles θ and ϕ.

Finally, `VAR` is the upper value for the varied parameter in the inner loop (related to `ICY`). The configuration is a set of numbers that specify the occupation of the yrast state, compared to the system at $\omega = 0$ – this needs to be carefully inferred from log files and spaghetti plots. The E_0 and G_{pair} terms, which allow energy/pairing offsets, have not been used in these calculations.

University of Cape Town

Outputs

The TAC code produces outputs of the quasiparticle energy eigenvalues in terms of the spherical basis. When run with parameter loops it also outputs the spaghetti plot information, total energies, and (relevant to the RPA), the wavefunctions of every quasiparticle configuration in the spherical basis.

B.2.2 RPASEPZ

The main program used is the Random Phase Approximation for SEParable interactions with Z-signature symmetry.

Inputs

```
NI
I(1), I(2), ..., I(NI)
I_trans, L_trans, M_trans, IPAR, THETA, ICASE
IFSTRETCH, IFIT, EFIT
κ(1), f(1,1), f(1,2), f(1,3), f(1,4)
    ⋮
κ(NI), f(NI,1), f(NI,2), f(NI,3), f(NI,4)
E1, E2, ESTEP
EPOL(p), EPOL(n)
Z, N
DELTA, RSMIN
ISEARCH, SIG
WFCname, NUwfc
```

The first line specifies the number of multipole interactions to be used, and the indices specifying the interactions are then listed on the second line. The third line specifies the I, L and M of the transition operator used, the parity of the states (for the calculations performed here, this was $L = 1, \pi = -$), the angle θ of the cranking, and a flag indicating whether to use the θ specified or not.

University of Cape Town

On the fourth line, the IFSTRETCH parameter is a flag referring to which set of basis states should be used, IFIT is a flag as to whether the interaction strength needs to be fitted or not, and if it does, the lowest energy solution will be chosen to match EFIT.

The following NI lines contain the interaction strengths κ_i for the interactions, together with the f multipliers for various forms: f_1 for isoscalar, f_2 for isovector, f_3 for only protons and f_4 for only neutrons. Based on some calculations [72], it was felt that the lowest vibrational terms will be a result of the isoscalar form, so f_1 was set to 1, and $f_2 = f_3 = f_4 = 0$.

The following lines refer to the strength function calculations. E1, E2 and ESTEP are the lower and upper energies of the output (with specified step). EPOL gives the relative polarization strengths for protons/neutrons – this has no effect on the RPA calculations, as long as $E_{pol}(p) - E_{pol}(n) = 1$. The Z and N are the numbers of protons and neutrons in the nucleus. DELTA refers to the Lorentzian width of the strength function, and RSMIN specifies the threshold strength before a solution is claimed.

For manually searching through energy intervals to find solutions, the ISEARCH flag can be used, and SIG specifies the signature of the solutions. Finally, WFCname specifies the filename of the TAC output wavefunctions, which are also taken as input, and NUwfc is the number of wavefunctions in the specified file.

University of Cape Town

Outputs

The primary output of the program is the list of RPA eigenenergies, and their relative B(E1) strength. There is also a log file that specifies the quasiparticle decomposition of every such state, which can be used for identifying pure two quasiparticle bands, simple band mixing, as well as vibrational states, which have no predominant contribution from any quasiparticle state.

B.3 Performing calculations

Based on the experimental Routhians, a low-ω value was chosen where the octupole band was observed. This was chosen as the RPA solutions are more representative before the interaction of the vibrational and yrast states becomes significant. The fits were performed, giving values for the octupole interaction strengths κ_+ and κ_-. These strengths were then taken as constant, and were used for all further experiments.

The deformations and pairing gaps for the nuclei of interest were taken from the tables of Möller, Nix. The range of angular frequencies was chosen from 0 to 0.3 MeV, although it was found that after the first band-crossings the results became slightly erratic. The calculations were performed in steps of $\Delta\omega = 0.01$ MeV, changing the TAC configuration as necessary. For every ω, the outputs of the TAC were used as inputs to the RPA code, and the log of all energies and B(E1) strengths was recorded.

Regarding the identification of bands as 'vibrational', a check needs to be performed that the quasiparticle contributions for that particular energy eigenvalue are indeed scattered. A quicker way is to consider the states with the strongest excitation (being collective, the B(E1) rates are expected to be higher), and the continuity of solution can be applied as the 'tracing' of figures 5.6, 5.7.

University of Cape Town

	$N = 88$	$N = 90$	$N = 92$
$Z = 70$ (Yb)	$\varepsilon_2 = 0.150$ $\varepsilon_4 = -0.020$	$\varepsilon_2 = 0.192$ $\varepsilon_4 = 0.000$	$\varepsilon_2 = 0.208$ $\varepsilon_4 = 0.000$
$Z = 68$ (Er)	$\varepsilon_2 = 0.175$ $\varepsilon_4 = -0.013$	$\varepsilon_2 = 0.200$ $\varepsilon_4 = -0.013$	$\varepsilon_2 = 0.233$ $\varepsilon_4 = -0.013$
$Z = 66$ (Dy)	$\varepsilon_2 = 0.192$ $\varepsilon_4 = -0.020$	$\varepsilon_2 = 0.217$ $\varepsilon_4 = -0.020$	$\varepsilon_2 = 0.242$ $\varepsilon_4 = -0.027$
$Z = 64$ (Gd)	$\varepsilon_2 = 0.192$ $\varepsilon_4 = -0.027$	$\varepsilon_2 = 0.225$ $\varepsilon_4 = -0.040$	$\varepsilon_2 = 0.250$ $\varepsilon_4 = -0.047$

Table B.1: Deformation parameters used for the systematic TAC+RPA calculations [18].

Bibliography

[1] S.G. Nilsson, I. Ragnarsson, *Shapes and Shells in Nuclear Structure,* Cambridge University Press, 1995.

[2] R.F. Casten, *Nuclear Structure from a Simple Perspective,* Oxford Studies of Nuclear Physics, 2nd ed., 2002.

[3] W. Greiner, J.A. Maruhn, *Nuclear Models,* Springer-Verlag, 1996.

[4] K.S. Krane, *Introductory Nuclear Physics,* John Wiley & Sons, 1988.

[5] K. Heyde, *Basic Ideas and Concepts in Nuclear Physics,* Institute of Physics Publishing, 2nd ed., 1999.

[6] B.R. Martin, *Nuclear and Particle Physics,* John Wiley & Sons, 2006.

[7] P. Ring, P. Schuck, *The Nuclear Many-Body Problem,* Springer-Verlag, 1980.

[8] A. Bohr, *The Coupling of Nuclear Surface Oscillations to The Motion of Individual Nucleons, Mat. Fyz. Medd. Dan. Vid. Selsk.* **26**, 14 (1952)

[9] J. Dudek, A. Góźdź, N. Schunck, M. Miśkiewicz, *Nuclear Tetrahedral Symmetry: Possibly Present Throughout the Periodic Table,* Phys. Rev. Lett. **88**, 252502 (2002)

[10] N. Schunck, J. Dudek, *Nuclear Tetrahedral Symmetry,* Int. J. Mod. Phys. **E13**, 213 (2004)

University of Cape Town

[11] J. Dudek et al., *An Island of Rare Earth Nuclei with Tetrahedral and Octahedral Symmetries: Possible Experimental Evidence,* Phys. Rev. Lett. **97**, 072501 (2006)

[12] J. Dudek, *Nuclear Tetrahedral and Octahedral Symmetries: Beginning of New Avenues...,* Gordon Conference on Nuclear Physics (2007)

[13] R.A. Bark et al., *Non-Zero Quadrupole Moments of Candidate Tetrahedral Bands,* Phys. Rev. Lett. **104**, 022501 (2010)

[14] M.G. Mayer, *On Closed Shells in Nuclei,* Phys. Rev. **74**, 235 (1948)

[15] M.G. Mayer, J.H.D. Jensen, *Elementary Theory of Nuclear Shell Structure,* John Wiley & Sons, 1955

[16] S.G. Nilsson, *Binding states of individual nucleons in strongly deformed nuclei,* Mat. Fys. Medd. Dan. Vid. Selsk. **29**, 16 (1955)

[17] S.G. Nilsson et al., *On the Nuclear Structure and Stability of Heavy and Superheavy Elements,* Nucl. Phys. A **131**, 1 (1969)

[18] P. Möller et al., *Nuclear Ground-State Masses and Deformations,* Atomic Data and Nuclear Data Tables **59**, 181 (1995)

[19] D.R. Inglis, *Particle derivation of nuclear rotation properties associated with a surface wave,* Phys. Rev. **96**, 1059 (1954)

[20] R.B. Firestone et al., *Table of Isotopes,* Wiley-Interscience, 8th ed., 1996

[21] R. Bengtsson, S. Frauendorf, *Quasiparticle spectra near the yrast line,* Nucl. Phys. A **327**, 139 (1979)

[22] S. Frauendorf, *Spin Alignment in Heavy Nuclei,* Physica Scripta, Vol **24**, 349 (1981)

[23] R. Bengtsson, J.D. Garret, *The Cranking Model – Theoretical and Experimental Basis,* Int. Rev. of Nucl. Phys. "Collective Phenomena in Atomic Nuclei" (1983)

University of Cape Town

[24] R. Bengtsson, S. Frauendorf, F.-R. May, *Quasiparticle Levels,* in At. Data Nucl. Data Tables **35**, 15 (1986)

[25] S.M. Harris, *Higher order corrections to the cranking model,* Phys. Rev. **138**, B509 (1965)

[26] J. Bardeen, L.N. Cooper, J.R. Schiffer, *Theory of superconductivity,* Phys. Rev. **108**, 1175 (1957)

[27] A. Bohr, B.R. Mottleson, D. Pines, *Possible analogy between the excitation spectra of nuclei and those of the superconducting metallic state,* Phys. Rev. **110**, 936 (1958)

[28] P.A. Butler, W. Nazarewicz, *Intrinsic reflection assymetry in atomic nuclei,* Rev. Mod. Phys. **68**, 349 (1996)

[29] K. Neergård P. Vogel, *Low-lying octupole states of the doubly even deformed nuclei with* $152 \leq A \leq 190$*,* Nucl. Phys. A **145**, 33 (1970)

[30] P. Vogel, *Negative parity yrast states in deformed nuclei,* Phys. Lett. B **60**, 431 (1976)

[31] F. Dönau, *Manual for the running of TAC3D and RPASEP codes,* and *The RPA for separable interactions,* unpublished.

[32] J.D. Jackson, *Classical Electrodynamics,* John Wiley & Sons, 1998.

[33] G. Battistuzzi et al., *A plunger device for in-beam measurements of nuclear lifetimes,* Nucl. Inst. and Meth. **146**, 481 (1977)

[34] L. Riedinger, *E1 Rates and Things Tetrahedral,* unpublished, (2008)

[35] A. Gavron, *Statistical model calculations in heavy ion reactions,* Phys. Rev. C **21**, 230 (1980)

[36] R.T. Newman et al., *High-spin studies with the AFRODITE array,* Balkan Phys. Lett. 182 (1998)

University of Cape Town

[37] R.M. Lieder, *New Generation of Gamma-Detector Arrays,* Experimental Techniques in Nuclear Physics p 137, (1997)

[38] R.K. Bhowmik, *Experimental Methods of Nuclear Spectroscopy: High spin states,* in *Structure of Atomic Nuclei*, Narcsa

[39] P.J. Nolan, *EUROGAM - A High Efficiency Escape Suppressed Spectrometer Array,* Nucl. Phys. A **520**, 657c (1990)

[40] C.W. Beausang et al., *Measurements on prototype Ge and BGO detectors for the Eurogam array,* Nucl. Inst. and Meth. **313**, 37 (1992)

[41] P.M. Jones et al., *Calibration of the new composite "clover" detector as a Compton polarimeter for the EUROGAM* , Nucl. Inst. and Meth. **362**, 556 (1995)

[42] J.F. Sharpey-Schafer, J. Simpson, *Escape suppressed spectrometer arrays: A revolution in γ-ray spectroscopy,* Progress in Particle and Nuclear Physics **21**, 293 (1988)

[43] G.F. Knoll, *Radiation Detection and Measurement,* 2nd edition, John Wiley and Sons (1989)

[44] D.B. Campbell, *Angular momentum induced shape changes in the rare-earth nuclei $^{152,153}Gd$ and $^{159,160}Yb.$,* PhD Thesis, Florida State University, 2004

[45] P. Mukherjee, A.K. Sengupta, *^{152}Eu as a Calibrating Source for Ge(Li) Detectors,* Nucl. Inst. and Meth. **68**, 165 (1969)

[46] D.C. Radford, *ESCL8R and LEVIT8R: Software for interactive graphical analysis of HPGe coincidence data sets,* Nucl. Inst. and Meth. **361**, 297 (1995)

[47] K.S. Krane et al., *Directional correlations of gamma radiations emitted from nuclear states oriented by nuclear reactions or cryogenic methods,* Atomic Data and Nuclear Data Tables **11**, 351 (1973)

University of Cape Town

[48] K. Starosta et al., *Experimental test of the polarization direction correlation method (PDCO),* Nucl. Inst. and Meth. **423**, 16 (1999)

[49] *National Nuclear Data Center Database,* `www.nndc.bnl.gov`

[50] E.S. Paul et al., *Loss of collectivity in the transitional* ^{156}*Er nucleus,* Phys. Rev. C **79**, 044324 (2009)

[51] J.M. Rees et al., *Non-yrast positive-parity structures in the* γ*-soft nucleus* ^{156}*Er,* Phys. Rev. C **83**, 044314 (2011)

[52] H. Beuscher et al., *Evidence for Strong Variation of the Moment of Inertia at Higher Angular Momenta in the Ground State Rotational Bands of* ^{158}*Er and* ^{166}*Yb,* Phys. Lett. B **40**, 449 (1972)

[53] J. Burde et al., *Third Discontinuity in the Yrast Levels of* ^{158}*Er,* Phys. Rev. Lett. **48**, 530 (1982)

[54] J. Simpson et al., *Spin 50*$\hbar$ *in* ^{160}*Er and the boundary between collective and non-collective rotation in light Er isotopes,* J. Phys. G **13**, L235 (1987)

[55] K. Dusling et al., *Medium-spin* γ*-ray spectroscopy of the transitional nucleus* ^{160}*Er,* Phys. Rev. C **73**, 014317-1 (2006)

[56] J. Ollier et al., *Ultrahigh-spin spectroscopy of* ^{159,160}*Er: Observation of triaxial strongly deformed structures,* Phys. Rev. C **80**, 064322 (2009)

[57] T. Hayakawa et al., *High spin states in* ^{158}*Dy,* Phys. Rev. C **68**, 067303 (2003)

[58] A. Pipidis et al., *Structural behavior of* ^{157,158,159}*Dy in the* $I = 30-50\hbar$ *spin regime,* Phys. Rev. C **72**, 064307 (2005)

[59] C.W. Reich, *Nuclear Data Sheets for* $A = 156$*,* Nucl. Data Sheets **99**, 753 (2003)

[60] P.E. Garrett, *Characterization of the* β *vibration and* 0_2^+ *states in deformed nuclei,* J. Phys. G **27**, R1 (2001)

University of Cape Town

[61] K. Heyde, J.L. Wood, *Shape coexistence in atomic nuclei,* Rev. Mod. Phys. **83**, 1467 (2011)

[62] I. Hamamoto, H. Sagawa, *Electromagnetic transitions in rotating nuclei,* Nucl. Phys. A **327**, 99 (1979)

[63] D.R. Zolnowski, M.B. Hughes, J. Hunt, T.T. Sugihara, *Systematics of quasirotational states in $N = 88$ nuclei,* Phys. Rev. C **21**, 2556 (1980)

[64] R.A. Bark et al., *Physics at low spin in the mass 160 region: the search for tetrahedral shapes,* Nucl. Phys. A **834**, 58c (2010)

[65] Q.T. Doan et al., *Spectroscopic information about a hypothetical tetrahedral configuration in ^{156}Gd,* Phys. Rev. C **82**, 067306 (2010)

[66] M. Jentschel et al., *Ultrahigh-Resolution γ-Ray Spectroscopy of ^{156}Gd: A Test of Tetrahedral Symmetry,* Phys. Rev. Lett. **104**, 222502 (2010)

[67] L. Riedinger, *Search for new symmetries in fast-rotating nuclei,* Zakopane Conference on Nuclear Physics (2012)

[68] W.D. Kulp et al., *Search for intrinsic collective excitations in ^{152}Sm,* Phys. Rev. C **77**, 061301 (2008)

[69] W.D. Kulp et al., *$N = 90$ region: The decays of $^{152}Er^{m,g}$ to ^{152}Sm,* Phys. Rev. C **76**, 034319 (2007)

[70] R.F. Casten, W.-T. Chou, N.V. Zamfir, *Signature splitting in octupole bands of vibrational and deformed nuclei,* Nucl. Phys. A **555**, 563 (1993)

[71] S. Frauendorf, private communication.

[72] F. Dönau, private communication.

University of Cape Town

Acknowledgments

There are many people to whom I owe a debt of thanks, who have affected my work during the perfect number of years I have spent on my PhD.

Firstly, I would like to thank my parents: Tadeusz and Danuta Stankiewicz for encouraging me to continue with my work despite the setbacks, and for pushing me to finish when things looked bleakest.

Secondly, I'm grateful for my friends: Rudy Chetty, Katharine Henninger, Angus Morrison, Max Richter and Sam Perumal may have done more distracting than pushing me, but they ensured that my life was enjoyable during this time. Perhaps with more harassment I would have finished quicker.

I am very much indebted to Fritz Dönau, without whom the RPA calculations could not have been performed. Without the many hours of discussion about the theory, the interpretations of the calculations, let alone the regular updates and fixes to (his) codes, I would not have been able to obtain the theoretical results that I have.

I would like to thank my supervisors for introducing me to the field of nuclear physics. I would also like to offer a word of thanks to all the people who assisted me with my work: this includes (but is not limited to) David Aschman from UCT, Rob Bark, Pradip Datta, Pete Jones, Elena Gueorguieva-Lawrie, Simon Mullins, Paul Papka and Mathis Wiedeking from the iThemba LABS physics group, Sean Murray from IT, and Rainer Thomae from the iThemba accelerator group.

I'd like to thank Spencer Wheaton and Andy Buffler for all the assistance and reassurances they provided me whenever I needed a shoulder to cry on.

I would like to acknowledge the National Research Foundation (NRF), and iThemba LABS for financial assistance.

Last, but certainly not least: I'm glad for the students who love Olympiad mathematics at least as much as I do, and who, through extreme hard work and dedication, have allowed me to continue with my passion for such beauty. It has been a rare pleasure to work with such an intelligent group of people, and a true privilege to be Leader of SA IMO delegations.

University of Cape Town